Channel Model and Performance Analysis of Millimetre-wave UAV Air-to-Ground Link under UAV Wobbling

Songjiang Yang

Department of Electronic and Electrical Engineering

The University of Sheffield

Supervisors: Prof. Jie Zhang, Dr. Wei Liu

This thesis is submitted for the approval of the

Doctor of Philosophy

June 2022

This thesis is dedicated to my beloved parents and friends. Without their unconditional love, encouragement and support, I would not be the person I am today.

Acknowledgements

I am indebted to my supervisor Professor Jie Zhang for his continued guidance, encouragement, and support to enlighten and shape me to be an independent researcher. Without his guidance and persistent help, this thesis would not have been possible.

I would like also like to thank my second supervisor Dr. Wei Liu for his insightful feedback and help.

I would like to sincerely thank Dr. Jiliang Zhang and Prof. Xiaoli Chu, without whom I would not have made it through my Ph.D. degree. Dr. Jiliang Zhang selflessly devotes his time and efforts to our weekly discussion. Without his precious support, it would not be possible to conduct this research. Prof. Xiaoli Chu gave me the opportunity to attend the EC H2020 MSCA project Indoor Small-Cell Networks with 3D MIMO Array Antennas (is3DMIMO). Their work and attitude have set an energetic example to me, which encourages me to overcome a hard time in my Ph.D.

I am very fortunate to work with colleagues in the wireless group of the University of Sheffield. A special thank you to my colleagues, Dr. Wenfei Yang and Dr. Junwei Zhang who gave me their help and time in listening to me and helping me work out my problems during the whole Ph.D. stage. A special mention goes to Dr. Bo Ma and Dr. Tao Hu who are my best friends and life mentors. They share many happy memories in my leisure time and raise me up when I am down.

Last but not the least, I would like to thank my parents Mrs. Ning Jiang and Mr. Chun Yang, who are always supporting me in chasing my dreams. My grandparents also encourage me in my hard time. The tireless support from family is always my spiritual anchor in this fast-changing and competitive environment.

Abstract

Fifth-generation (5G) and beyond mobile communication networks are expected to meet an explosion of data traffic usage and a fast-varying environment. The millimetre-wave communications and unmanned aerial vehicles (UAVs) communications are two important methods to tackle these challenges. To thoroughly investigate millimetre-wave UAV communications, it is essential to have a good understanding of electromagnetic wave propagation in the millimetre-wave band between the UAV-carried aerial base station or the mobile relay node and ground nodes, which is known as the UAV air-to-ground (A2G) channel model. To support the millimetre-wave UAV A2G network design, it is vital to have a deep cognition of the network performance evaluation parameters of the UAV A2G link, e.g., throughput and energy efficiency. This thesis discusses three problems related to millimetre-wave UAV A2G communications.

In this study, the effect of the inevitable UAV wobbling on the millimetre-wave UAV A2G channel is first investigated. The wobbling process of a hovering UAV, which is affected by wind gusts and the high vibration frequency of its propellers and rotors, is modelled. The analytical temporal autocorrelation function (ACF) for the millimetre-wave UAV A2G link is derived. With the derived temporal ACF equation, the Doppler power spectrum density for the millimetre-wave UAV A2G link is investigated. The numerical results show that the temporal ACF decreases quickly with time and the impact of the Doppler effect caused by UAV wobbling is significant on bit error probability (BEP) for the millimetre-wave A2G link.

Then, the problem of throughput for the millimetre-wave UAV A2G link under UAV wobbling is investigated. Two types of detectors at the receiver to demodulate the received

signal and get the instantaneous BEP of a millimetre-wave UAV A2G link under UAV wobbling are introduced. Based on the designed detectors, an adaptive modulation scheme maximising the average transmission rate under UAV wobbling by optimizing the data transmission time subject to the maximum tolerable BEP is proposed. The numerical results show that the proposed adaptive modulation maximises the temporally averaged transmission rate of the millimetre-wave UAV A2G link compared with other transmission policies under UAV wobbling.

After proposing the adaptive modulation, the power control to minimise the power consumption is investigated considering the limited on-board energy of a UAV. A power control policy that minimises the transmission power while maintaining both the BEP under the threshold and the maximised average transmission rate is proposed for the millimetre-wave UAV A2G link under UAV wobbling. The energy efficiency of the UAV A2G link is evaluated to show how effective this power control policy is. The numerical results show that the power control policy reduces the power consumption by up to 50% for wobbling millimetre-wave UAV A2G links and the energy efficiency of the system under power control is higher than that of the adaptive modulation scheme without the power control policy.

In summary, the thesis studies the channel characteristics and evaluates the performance of the millimetre-wave UAV A2G link under wobbling to support the future millimetre-wave UAV communication network deployment. A key observation is that even for weak UAV wobbling, the temporal ACF of the UAV A2G link deteriorates quickly, making the link difficult to establish a reliable communication link. To keep the reliable A2G link and achieve high throughput, the adaptive modulation scheme of the millimetre-wave UAV A2G link under wobbling is proposed. The power control policy for the adaptive modulation of the millimetre-wave UAV A2G link could save power by over 50% and support the green UAV A2G link.

List of Publications

Published

1. **S.Yang**, Z. Zhang, J. Zhang, and J. Zhang, “Impact of rotary-wing UAV random wobbling on millimeter wave air-to-ground wireless channel” *IEEE Transactions on Vehicular Technology,* **Accepted**.

2. **S. Yang**, J. Zhang and J. Zhang, “Impact of foliage on urban mmWave wireless propagation channel: A ray-tracing based analysis," *in Proc. International Symposium on Antennas and Propagation,* Xi’an, China, 2019, pp. 1-3.

3. Y. Jiang, H. Hu, **S.Yang**, J. Zhang and J. Zhang, “Generalized 3-D spatial scattering modulation," *IEEE Transactions on Wireless Communication,* vol. 21, no. 3, pp. 1570-1585, Mar. 2022

4. Y. Zhang, C. Chen, **S. Yang**, J. Zhang, X. Chu and J. Zhang, “How friendly are building materials as reflectors to indoor LOS MIMO communications?," *IEEE Internet of Things Journal,* vol. 7, no. 9, pp. 9116-9127, Sept. 2020.

5. C. Chen, **S. Yang**, J. Zhang, X. Chu and J. Zhang, “Tractable performance analysis of small-cell networks with a novel bounded path loss model," *Electronics Letters*, vol. 56, no. 2, pp. 105-107, Jan. 2020.

Under review

1. **S.Yang**, Z. Zhang, J. Zhang, X. Chu, and J. Zhang, “Adaptive modulation for wobbling UAV air-to-ground links in millimeter-wave bands” *IEEE Transactions on Wireless Communication*.

2. **S. Yang**, J. Zhang and J. Zhang, “Energy efficiency optimization in millimeter-wave air-to-ground links under UAV wobbling," *in Proc. 2022 PIMRC*.

Table of Contents

List of Figures

List of Tables

Abbreviations

3D Three dimension

3GPP Third-generation partnership project

5G Fifth-generation

6G Sixth-generation

A2A Air-to-air

A2G Air-to-ground

AAoA Azimuth angle of arrival

AAoD Azimuth angle of departure

ACF Autocorrelation function

AoA Angle of arrival

AoD Angle of departure

AWGN Additive white Gaussian noise

BEP Bit error probability

BS Base station

CDF Cumulative distribution function

CIR Channel impulse responese

COTS Common off-the-shelf

CSI Channel state information

CW Continuous wave

EAoA Elevation angle of arrival

EAoD Elevation angle of departure

EE Energy efficiency

FAA Federal aviation administration

FW Fixed-wing

GBSM Geometry-based stochasticchannel model

GPS Global positioning system

GPU Graphics processing units

HAP High altitude platform

IoT Internet of things

IRS Intelligent reflection surface

ITU International telecommunication union

LAP Low altitude platform

LoS Line-of-sight

LTE Long term evolution

MIMO Multiple-input-multiple-output

NLoS Non-line-of-sight

PDF Probability density function

PDP Power delay profile

PEP Pairwise error probability

PLE Path loss exponent

PSD Power spectral density

PSK Phase shift keying

QAM Quadrature amplitude modulation

RMS Root-mean-square

RIS Reconfigurable intelligent surface

RW Rotary-wing

SB Single-bounced

SINR Signal-to-interference-plus-noise-ratio

SNR Signal-to-noise-ratio

UAV Unmanned aerial vehicle

UE User equipment

UUB Union upper bound

V2V Vehical-to-vehical

Chapter 1

Introduction

Overview

In this chapter, the background, motivations, objectives, and contributions of this thesis will be introduced. Unmanned aerial vehicle (UAV) communication systems and millimetre-wave techniques have been proposed to address the growing demand for emergency assistance and the high data rate in the fifth-generation (5G) communication system era. The research objectives and contributions of this thesis about millimetre-wave UAV communications are discussed. Finally, the structure of this thesis is presented.

1.1 Background

In the fifth-generation (5G) communication system era, unmanned aerial vehicles (UAVs) have been widely investigated to facilitate numerous applications such as flexible coverage and capacity enhancements, emergency assistance, disaster relief, etc. [1–3]. According to [4], the 5G communication system should support the enhanced mobile broadband, the ultra-reliable and low latency communications, and the massive machine-type communications. Moreover, the millimetre-wave is one of the important techniques to achieve the requirement of the 5G communication system, which could support higher data rate due to higher bandwidth, enable miniaturization of the antenna array in UAV base station (BS) due to short wavelength, and suppress interference due to high beam directivity [5–8]. The integration

of UAVs into millimetre-wave communications will bring new design opportunities and challenges.

UAVs are aircraft driven by remote control or computer program on-board without a human pilot. In recent years, UAVs have entered our daily lives for numerous civilian and commercial applications owing to the advancement of manufacturing technologies and cost-reducing. According to a report from the Federal Aviation Administration (FAA), the fleet of UAVs for recreation will be increased from around 1.32 million vehicles in 2019 to 1.59 million units by 2024. Moreover, the fleet of UAVs for commercial will be more than doubled from around 0.39 million vehicles in 2019 to 0.82 million units by 2024 [9].

In practice, there are two general standards for UAV classification. In general, UAVs can be classified, based on altitudes, into two categories, i.e., high altitude platforms (HAPs) and low altitude platforms (LAPs). For HAPs, the altitudes of the UAV can reach the upper layers of the stratosphere [10]. On the other hand, LAPs are quasi-stationary aerial platforms within the troposphere [11]. Compared with HAPs, LAPs are much easier to deploy which is suitable for time-sensitive applications. However, the HAPs have longer power endurance. Moreover, UAVs can be classified, based on type, into two categories, i.e., fixed-wing (FW) and rotary-wing (RW) UAVs. Conventionally, the FW UAV, with high load capability, has been applied to carry BS equipment, which is too large for RW UAV to carry. However, the FW UAV has to maintain continuous high-speed mobility, which brings challenges to system design for stationary local area coverage [12]. This non-stationary wireless propagation channel has a negative impact on the stability of the wireless connection [13]. With the evolution of small cell networks, BS equipment is expected to be further miniaturized in the future when the millimetre-wave band is widely used. Thus, the RW UAV with relatively low load capability can facilitate stable and flexible coverage for a certain area by filling coverage holes and/or providing extra capacity by overlaying on an existing cellular network while it is hovering in the air. In Fig 1.1, an overview of the different classifications of the UAVs is provided.

Since UAVs need the remote control, wireless communications have become essential for UAV operation and have drawn significantly growing attention for combining together in re-

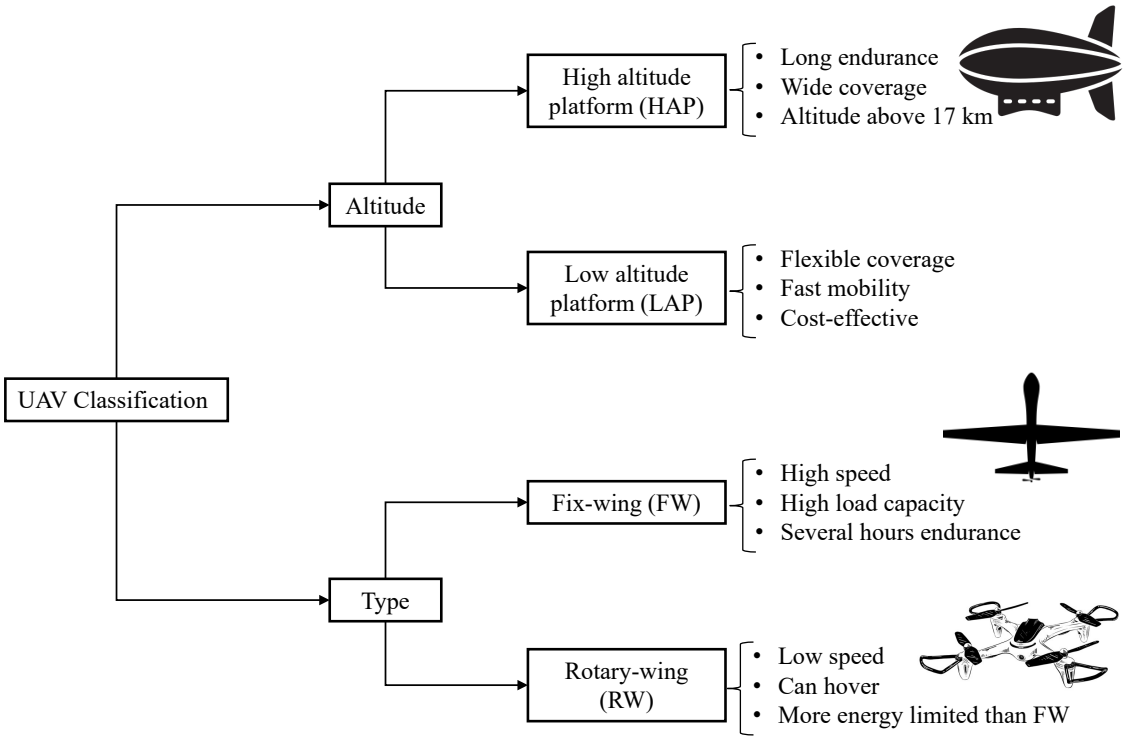

Fig. 1.1 UAV classification.

cent years. Depending on different mission requirements of UAV communications, they may need to timely transmit and/or receive information, such as images, video, and data packets to/from various ground nodes. There are two main applications of UAV communications, i.e. cellular-connected UAV and UAV-assisted communications. The main difference between cellular-connected UAV and UAV-assisted communications is the roles of the UAV. The UAV acts as BSs, access points or relays in UAV-assisted wireless communications and the UAV acts as user equipment (UE) in cellular-connected UAV communications. The two paradigms of cellular-connected UAV communications and UAV-assisted communications share both similarities (e.g., in terms of air-to-ground (A2G) UAV channel characteristics and interference) and differences (e.g., communication requirements and design considerations) [14]. Recently, the Third-generation Partnership Project (3GPP) has specified the communication requirements for the UAV-assisted communication system, where the data rate requirement for UAV command is in the range of 60-100 kb/s for both downlink and uplink directions [15]. For the cellular-connected UAV communications, the real-time remote control and

Table 1.1 Comparison of wireless technologies for UAV communications.

Technology	Description	Advantages	Disadvantages
Direct link	Direct point-to-point communication with ground node	Simplicity and low cost	Limited to LoS, limited operation range, low reliability and data rate
Satellite	Internet access via satellite	Global coverage	High operational cost, large attenuation and delay, high energy-consuming
Ad-hoc network	Dynamically self-organizing network	High-mobility, robust and flexible architecture	High energy consumption, low spectrum efficiency, long delay
Cellular network	Communication via cellular infrastructure	Cost-effective, support large-scale UAV communications, high reliability and data rate	Remote areas unavailable

video data transmission, where the transmission rate requirement is about several Mb/s or Gb/s.

To meet the communication requirements of UAV communications, four candidate communication technologies include 1) direct link; 2) satellite; 3) ad-hoc network; and 4) cellular network. The comparison of wireless communication technologies for UAV communications is shown in Table 1.1 [16]. After comparison, integrating UAVs into the cellular network in millimetre-wave bands offers cost effectiveness, high reliability, and high data rate for UAV communications in the 5G era. The schematic diagram of UAV-assisted network is shown in Fig. 1.2.

The aforementioned benefits make 5G cellular networks become a promising new trend to support the increasing and dynamic UAV wireless data traffic. However, the millimetre-wave UAV communication system is significantly different from its terrestrial counterparts because of the high altitude, high mobility, and high probability of the line-of-sight (LoS) A2G channel. Table 1.2 summarized the main design opportunities and challenges of millimetre-wave UAV communications, which are further discussed as follows.

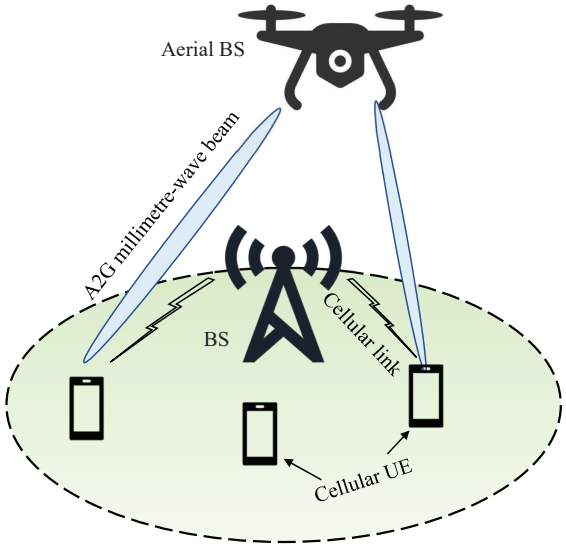

Fig. 1.2 UAV-assisted communication network.

- Compared with conventional terrestrial BSs/users, the UAV BSs/users usually have a much higher altitude. The high UAV altitude leads to the high LoS A2G probability because the scatterers cannot block the LoS link [16]. The UAV coverage of aerial heterogeneous networks could be expanded by high UAV altitudes [17]. Since the high altitude UAVs could offer three-dimension (3D) aerial coverage for BSs or users, the 3D A2G channel model is required to support the transmission with the high data rate, the high reliability, and the low latency. However, A2G LoS links make inter-cell interference become a more critical issue for cellular systems with hybrid aerial and terrestrial UEs [14]. The high altitude also leads to a large propagation distance, which means larger path loss in millimetre-wave communications. Hence, the UAV hovering height and the UAV trajectory to keep the reasonable path loss and limited interference should be taken into account.

- Compared with conventional terrestrial BSs/users, the UAV BSs/users usually could be deployed more flexibly. It can support more emergent situations and quick action for an urgent network needs. However, the high mobility of UAVs leads to the highly dynamic communication channel characteristics for the A2G channel, and excessive spatial and temporal variations included in non-stationary situations. Moreover, the

Table 1.2 Opportunities and challenges of millimetre-wave UAV communications.

Characteristic	Opportunities	Challenges
High altitude	High LoS probability, wide coverage	Marginally relies on the elevation angle, require 3D A2G channel model, larger path loss, severe A2G interference
High mobility	Flexible deployment, coverage and capacity enhancements	Dynamic channel characteristics and the significant Doppler effect, the excessive spatial and temporal variations
Energy constraint	-	Energy-efficiency design, limited endurance time of UAVs
UAV structures	-	Airframe shadowing caused by the structural design and rotation of the UAV

Doppler effect becomes more severe when the frequency band is extended to the millimetre-wave band [18]. It is challenging to build a reliable 3D A2G channel model and analysis the channel characteristics for different operating scenarios.

- Compared with conventional terrestrial BSs/users, the UAV BSs/users are usually limited by the operating time. Since the size restriction of the UAV and the limitation of battery technology, the UAV energy consumption and reliable operating time has become a bottleneck of the UAV communication system [19]. The cruising and hovering time duration is limited by the on-broad battery capacity. Thus, the energy efficiency (EE) design of UAV communications is more involved and urgent than that of the conventional terrestrial system [20].

1.2 Motivations and Objectives

1.2.1 Motivations

As introduced in section 1.1, the millimetre-wave UAV communication system can offer enormous throughput, flexible coverage, and urgent capacity enhancement. To thoroughly

investigate the millimetre-wave UAV wireless system, it is necessary to have a deep understanding of the millimetre-wave propagation characteristics between the UAV and the ground node. Accordingly, the millimetre-wave UAV A2G channel model needs to be researched, where the channel characteristics are different from the classic terrestrial communication channel [17]. Especially, the movement and wobbling of UAVs, the type of UAVs, and the different propagation environments could affect the millimetre-wave UAV A2G channel characteristics significantly [21, 22]. The study of the millimetre-wave UAV A2G channel is the basement of the millimetre-wave UAV communications design.

Moreover, fundamental performance analysis to evaluate the impact of channel characteristics on the millimetre-wave UAV A2G communications is vital for designing millimetre-wave UAV communications. For example, the throughput of the UAV systems is the basic key quality-of-service metric. Since the time-varying channel characteristics of UAV A2G links lead to outdated channel state information (CSI) from the channel estimation, the bit error probability (BEP) performance of millimetre-wave UAV A2G links deteriorates. The throughput of the millimetre-wave UAV A2G link under wobbling will decrease by the worse BEP performance. However, the throughput problem of millimetre-wave UAV A2G link under UAV wobbling has not been sufficiently studied. To reap the benefits of millimetre-wave UAV communications, it is necessary to achieve the required system performance by considering the UAV wobbling.

In addition, under the size, weight, and battery capacity restrictions of UAVs, the power consumption has become a bottleneck for the UAV-carried aerial BSs or mobile relay nodes [19]. For instance, UAVs must use on-board battery energy to support signal transmission, signal processing, and mobility purposes, which results in the limited flight and hovering time duration [23]. Recently, the UAV moving trajectory optimization is the main research direction [24], but the power control policy applied to the transmission frame for the wobbling millimetre-wave UAV A2G links has not been studied in the literature. Extending the UAV operating time on limited on-broad battery capacity by power control policy while achieving the required throughput is also another challenging problem.

1.2.2 Objectives

Channel model of millimetre-wave UAV A2G link under wobbling

While UAVs are hovering or cruising in the air, UAVs will inevitably be wobbling due to various environmental and mechanical issues, such as wind gusts, bad weather, and the high vibration frequency of their propellers and rotors [21]. Such UAV wobbling leads to the Doppler effect on the millimetre-wave UAV A2G link [25, 26], making the wireless channel unstable and unpredictable [21]. Therefore, the millimetre-wave UAV A2G channel model under UAV wobbling must be investigated. Detailed objectives are listed as follows:

1. To capture mechanical vibration parameters of the UAV to introduce the UAV movement model under wobbling;

2. To derive the temporal channel autocorrelation function (ACF) for describing the channel property of millimetre-wave UAV A2G link under wobbling;

3. To derive the Doppler power spectrum density (PSD) based on the temporal ACF; and

4. To analyse how mechanical vibration parameters of the UAV impact the channel characteristics on millimetre-wave UAV A2G link under wobbling.

Throughput of millimetre-wave UAV A2G link under wobbling

Since time-varying channel characteristics lead to outdated CSI from the channel estimation, the BEP performance of millimetre-wave UAV A2G link under wobbling decreases. Furthermore, the worse BEP performance results in the low throughput of the system. Hence, the BEP performance and the throughput of millimetre-wave UAV A2G link under wobbling must be investigated for the design of a reliable network. Detailed objectives are listed as follows:

1. To build the relationship between the temporal ACF from the time-varying channel and the imperfect CSI from channel estimation;

2. To design the detector at the receiver demodulating the signal under imperfect CSI and computing the instantaneous BEP of the millimetre-wave UAV A2G link under wobbling;

3. To design the adaptive modulation scheme to keep the reliable UAV A2G link under imperfect CSI; and

4. To find the maximum average transmission rate based on the BEP threshold by optimizing the transmission period in an adaptive modulation scheme.

Power control of millimetre-wave UAV A2G link under wobbling

When the UAV cruising and hovering in the air, the power constraint should be considered to support an efficient flight for data transmission. Hence, the power control of the UAV transmission process must be investigated for maintaining high EE. The detailed objectives are listed as follows:

1. To design the power control policy for finding the minimum transmission power at transmitter subject to maximised throughput and BEP threshold;

2. To evaluate the EE performance of the millimetre-wave UAV A2G link with power control policy; and

3. To find the optimized transmission time achieving the maximum EE performance in an adaptive modulation scheme with a power control policy.

1.3 Contributions

The main contributions of the thesis are summarised as follows:

- Review the latest development of UAV A2G channel measurements, modelling and simulation. Important existing channel models are reviewed and classified.

Research on the channel modelling of millimetre-wave UAV A2G link under wobbling

- The RW UAV movement model at hovering status under UAV wobbling is introduced. Two parameters, i.e., the vibration frequency of the UAV and the velocity envelope covariance of UAV wobbling, are defined to capture the characteristic of UAV wobbling.

- The temporal ACF of millimetre-wave RW UAV A2G link is derived in a closed-form expression based on the RW UAV wobbling movement model at hovering status. The analytical expression of the temporal ACF is verified by Monte Carlo simulation results. The closed-form temporal ACF derivation can help the system compute the temporal ACF and evaluate the UAV A2G link performance quickly.

- The Doppler PSD of millimetre-wave RW UAV A2G link with UAV wobbling is computed based on the analytical temporal ACF.

Research on the adaptive modulation scheme of millimetre-wave UAV A2G link under wobbling

- The imperfect CSI is modelled by using a continuous temporal ACF of the millimetre-wave UAV A2G channel impulse response (CIR). Then, the relationship between the BEP and the temporal ACF is analytically derived and used to adjust the modulation order in the adaptive modulation scheme accordingly.

- Two detectors are introduced for millimetre-wave UAV A2G links under imperfect CSI, i.e., the maximum likelihood detector and the sub-optimum detector, which both use the continuous temporal ACF as the reference to demodulate the received signal and get the instantaneous BEP. To speed up the calculation of the instantaneous BEP, the sub-optimum detector ignores the power differences among symbols in a constellation diagram, leading to a computational complexity much lower than that of the maximum likelihood detector. I derive the closed-form union upper bound (UUB) on the BEP for

the sub-optimum detector under imperfect CSI and verify its accuracy by comparing it with Monte Carlo simulation results.

- An adaptive modulation scheme is proposed based on the designed detectors to maximize the average transmission rate of the millimetre-wave UAV A2G link under imperfect CSI. The data transmission time and the modulation order (among M-ary phase shift keying (PSK) or M-ary quadrature amplitude modulation (QAM)) are optimized subject to a BEP threshold, constant transmission power, and a channel estimation time constraint.

Research on the power control policy of millimetre-wave UAV A2G link under wobbling

- A new power control policy is designed to minimize the instantaneous transmission power of the adaptive modulation subject to the BEP threshold at the receiver and the maximum transmission power constraint, while maintaining the maximum average transmission rate. The BEP approximation based on the signal-space concept and the Netwon-Raphson method is used to compute the minimized instantaneous transmission power for M-ary PSK and M-ary QAM, respectively.

- The EE performance of the millimetre-wave UAV A2G link with the power control policy is evaluated under the constant transmission rate or the adaptive modulation scheme. The trade-off between the transmission time and the estimation time is analysed to find the maximum EE of the system.

1.4 Thesis Outline

The first chapter of this thesis summarises UAV communications and millimetre-wave techniques in the 5G network and introduces the research undertaken. The motivations, objectives, and contributions of the research are presented.

Chapter 2 presents an overview of the millimetre-wave UAV A2G channel model and the performance analysis of the UAV communication system. The UAV A2G channel models and the millimetre-wave channel models are introduced, which include millimetre-wave propagation properties, channel model methods, and millimetre-wave UAV channel characteristics. The performance analysis metrics of the UAV A2G communication system are presented, i.e., coverage probability, outage probability, throughput, and EE.

Chapter 3 studies the impact of mechanical wobbling on the Doppler effect of the millimetre-wave wireless channel between a UAV and a ground node. The wobbling process of a hovering RW UAV is modelled firstly. The analytical model of the temporal ACF for the millimetre-wave RW UAV A2G link in a closed-form expression is derived. How RW UAV wobbling impacts the Doppler effect on the millimetre-wave RW UAV A2G link is investigated. A key observation is that even for weak UAV wobbling, the temporal ACF of the UAV A2G link deteriorates quickly, making the link difficult to establish a reliable communication link.

Chapter 4 focuses on the throughput of millimetre-wave UAV A2G link under wobbling, which finds the maximum average transmission rate by optimum adaptive modulation scheme under imperfect CSI. Two detectors to demodulate the received signal and get the instantaneous BEP of a millimetre-wave UAV A2G link under imperfect CSI are introduced. Based on the designed detectors, an adaptive modulation scheme to maximize the average transmission rate under imperfect CSI by optimizing the data transmission time subject to the maximum tolerable BEP is proposed.

Chapter 5 proposes the power control policy of millimetre-wave UAV A2G link under wobbling, which can reduce the energy consumption based on the different transmission methods. The power control policy for the adaptive modulation of the millimetre-wave UAV A2G link could save power by over 50% and support the green UAV A2G link. The EE performance of the millimetre-wave UAV A2G link under the power control policy is shown. The trade-off between spectral efficiency and EE is discussed to achieve the system performance aims.

Chapter 6 summarizes the thesis by presenting the overall research outcomes and providing concluding remarks. In addition, potential further works are suggested at the end of the chapter.

Chapter 2

State-of-the-art and Research Challenges

Overview

This chapter introduces topics of the millimetre-wave UAV A2G channel modelling and the performance analysis of the UAV A2G link. For an in-depth investigation of the millimetre-wave UAV A2G channel models, the basic characteristics of the millimetre-wave propagation and the UAV A2G channel model need to be understood. Moreover, the performance analysis metrics of the UAV communications need to be reviewed. Accordingly, in this chapter, the millimetre-wave UAV A2G channel model is first introduced, followed by the performance analysis of UAV communication systems.

2.1 Review of Millimetre-wave Propagation

In this section, basic concepts and problems of millimetre-wave propagation properties are introduced.

2.1.1 Millimetre-wave Propagation Properties

Millimetre-wave is a class of electromagnetic wave which wavelength is at the millimetre level (1-10 mm) and the frequency spectrum is between 30 and 300 GHz [27]. The wavelength of the millimetre-wave is smaller than typical objects in the physical environment. Therefore, the propagation properties of millimetre-wave have some differences with lower frequency

waves. When the size of an obstacle is at millimetre level, millimetre-wave could be blocked whereas, low frequency band signal is not. When millimetre-wave transmits in free space, air and water molecule will act as the main attenuation role. Oxygen molecule mainly absorbs the 60 GHz electromagnetic wave and water molecule mainly absorbs the 164-200 GHz electromagnetic wave [28]. Therefore, 60 GHz, and 180 GHz bands have more excess attenuation than other frequency band and the excess attenuation are -20 dB/km, and -15 dB/km, respectively [29]. Fortunately, the 28 GHz, 38 GHz, and 72 GHz are working as good as currently used cellular bands for long-range outdoor mobile communications [6, 30].

2.1.2 Basic Millimetre-wave Channel Model

The free space propagation of the electromagnetic wave in the millimetre-wave band is a useful starting point for evaluating large-scale millimetre-wave wireless channel characteristics. If there are no obstructions, reflections, and scatterers, the easy model of large-scale propagation is a free space Friis model. The equation of the Friis model is shown below [31],

$$P_{\mathrm{r}} = P_{\mathrm{t}} G_{\mathrm{t}} G_{\mathrm{r}} \left(\frac{\lambda}{4\pi d} \right)^2, \tag{2.1}$$

where P_{r} and P_{t} are the received and transmitted power, respectively, G_{r} and G_{t} are the gain of receiver and transmitter antennas, respectively, λ is the operating wavelength of transmission, and d is the distance of transmitter and receiver. According to (2.1), the millimetre-wave free space propagation loss is higher than low frequency band. Fortunately, small directional narrow beam antennas which have substantial gain may offset and even reduce the path loss in the millimetre-wave frequency band [27]. However, this model only works well for the LoS path and the antennas aligned perfectly [32].

Compared to the free space Friis equation, log-distance path loss model will express path loss better for real-world situations [30]. The log-distance path loss model is related to the path loss exponent (PLE), which has different values in different propagation scenarios. The

log-distance path loss model is shown below [33],

$$P_{\mathrm{r}}[\mathrm{dBm}] = P_{\mathrm{t}}[\mathrm{dBm}] + K[\mathrm{dB}] - 10\alpha \log \frac{d}{d_0}, \tag{2.2}$$

where K is a dimensionless constant that depends on antenna characteristics and average channel attenuation, α is the PLE with different values of indoor and outdoor scenario, and d_0 is the reference distance. In general, the reference distance is 1 metre and when α value is 2, it means free-space propagation. According to [30], the α value at outdoor situation is in range of 2.3 to 3.86.

2.1.3 The Doppler Effect of Millimetre-wave

The small-scale millimetre-wave propagation also has some differences from microwave. Especially, the Doppler shift becomes vital to consider as one of the small-scale parameters in channel characteristics [34]. At millimetre-wave frequency, the Doppler effect has a more significant influence than the microwave frequency band. The Doppler shift is the difference between the received frequency and the actual transmitted frequency. When the carrier frequency increases, the Doppler shift will also increase fast. For example, when the carrier frequency increases from 2 GHz to 60 GHz, the Doppler shift increases 30 times [31]. Moreover, the much smaller wavelength of millimetre-wave signals results in a much smaller coherence time than the conventional ultra-high frequency band system, so the Doppler effect on the millimetre-wave band causes some severity problems in the UAV communication channel model. The Doppler shifts could disrupt the orthogonality between the sub-carriers in orthogonal frequency division multiplexing systems causing carrier frequency offset and inter-carrier interference.

2.2 Review of UAV A2G Channel Models

In this section, the state-of-the-art UAV A2G channel models are firstly reviewed from the measurement campaigns and basic channel model methods. Then, the analysed UAV A2G

Table 2.1 Key features of deterministic and stochastic channel models.

Channel modelling types	Key features	Complexity	Accuracy	Generality
Deterministic channel modelling	The propagation properties of electromagnetic waves should be considered in the model. The channel model is accurate, but much more complex than stochastic channel model.	High	High	Low
Stochastic channel modelling	The propagation parameters should be pre-defined in the model. However, the measurement parameters to support stochastic channel model are difficult to extract from the measurement results at specific environment.	Medium	Medium	Medium

channel characteristics and the popular channel model method are introduced to provide a general understanding of the UAV A2G channel.

2.2.1 Channel Modelling Methods

This subsection introduces the basic channel modelling methods of radio wave propagation. In general, existing channel modelling methods can be categorized into two types, i.e., deterministic models and stochastic models [35]. The deterministic method generates CIRs with high accuracy, but the computational complexity is relatively high. The stochastic method could get the accuracy enough channel information and the computational burden can be reduced. The key features of these two types of channel modelling methods are summarized in Table 2.1. The detailed deterministic and stochastic channel modelling methods are described below.

Deterministic Channel Models

The deterministic channel models are widely employed to simulate multipath propagation in a given environment. The deterministic models can predict electromagnetic wave propagation

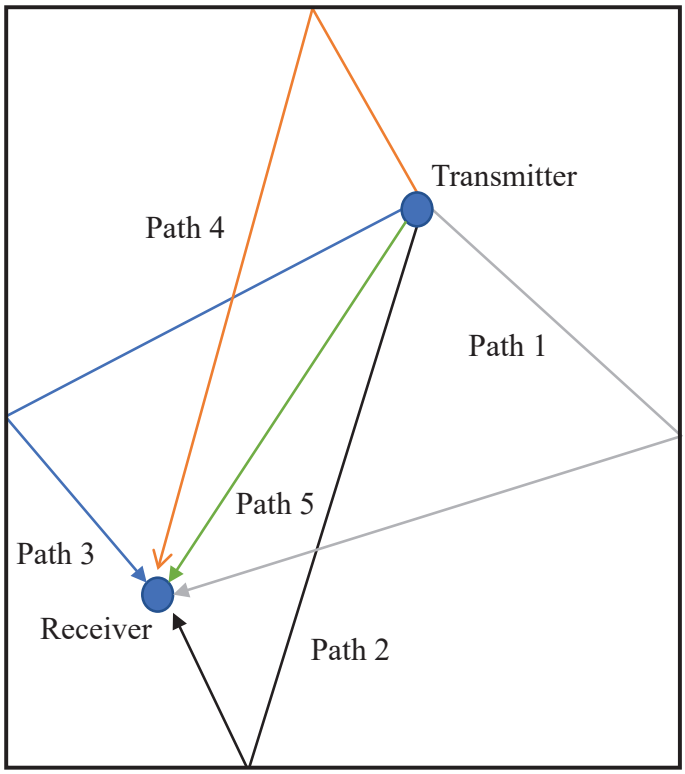

Fig. 2.1 Simple ray-tracing mechanism illustration in specific propagation scenario.

parameters more accurately with known propagation scenarios. For the high accuracy of the deterministic channel model, this method is currently widely used in radio propagation modelling software to simulate the channel model, where results from simulation could help the engineers to design the wireless networks better. However, the computational complexity of the propagation simulation increases significantly, thereby, leading to increased simulation time consumption and the high requirements on the hardware, such as graphics processing units (GPU), for the computation.

Conventionally, the deterministic propagation algorithms can be generally divided into the ray-tracing based method, the ray-launching based method, the Finite-Difference Time-Domain (FDTD) method, and Parabolic equation [36]. A brief description of these methods is discussed below.

- **Ray-tracing**

  The ray-tracing method predicts the ray propagations for fixed transmitter and receiver positions in a known environment. The simple ray-tracing propagation mechanism for a room is shown in Fig. 2.1. The rays are generated as the light satisfying geometrical optical rules for the given positions. With the concept of the rays, the simulated electromagnetic waves can be classified by their propagation mechanisms including LoS, reflection, penetration, diffraction, and scattering to express the channel characteristics [37]. The ray-tracing has been widely employed in indoor localization [38] and network deployment optimization [39] due to the high prediction accuracy of electromagnetic wave propagations.

- **Ray-launching**

  Ray-launching algorithms, also known as brute-force ray-tracing, shoot a huge number of rays from the transmitter to exhaustively generate all possible rays for the transmitter to all possible positions of receivers. For the ray-launching algorithms, the rays are propagated from a transmitter to anywhere with different propagation mechanisms including LoS, reflection, penetration, diffraction, and scattering, where the rays do not trace specifically for any exact receiver positions [40]. The basic assumptions and propagation principles of rays are the same as ray-tracing algorithms. The given environment is discretized into unit sections and computed fields for a traced ray represent the field over an entire ray tube volume [41].

- **Finite-Difference Time-Domain**

  FDTD method computes the reflection, diffraction and radiation propagation based on Maxwell's equation. FDTD method is capable of modelling most situations because the position relation between the transmitter and the receiver can then be involved in the solution directly for all points in the region of interest, but the poor efficiency would consume much calculation resources. Hence, it is not generally used individual for channel modelling but applied as a compensation method to improve the accuracy of ray-tracing and ray-launching methods [42].

- **Parabolic Equation**

  The parabolic equation model provides an approximation to the scalar wave equation modelling electromagnetic waves propagating at small angles. This model has a computational efficiency for the long distance radio propagation in the presence of terrain dependent environments. However, it is difficult to model the circumstance with high mobility objectives or other obstacles because of the limited propagation angles [43].

Stochastic Channel Model

The stochastic channel models are suitable to build the mobile-to-mobile channel model in a given environment. The reason for that is the good trade-off between accuracy and computational burden, and the good generality of the similar propagation environment [44]. The stochastic radio propagation algorithms can also be divided into a correlated-based stochastic model and a geometry-based stochastic model. A brief description of these methods is discussed below.

- **Correlation-Based Stochastic Models**

  Correlation-based stochastic models (CBSMs) assume that the channel coefficients are generated from zero-mean complex independent and identically distributed random variables. The CBSMs describe the channel characteristics by correlation matrices instead of the directional propagation parameters [44]. For channel modelling, the correlation in the time, frequency, and spatial domains should be considered. Hence, the statistical behaviour of the channel characteristics can be computed from the measurement data by statistical methods.

- **Geometry-based Stochastic Channel Model**

  The geometry-based stochastic channel model (GBSM) modelled the channel characteristics based on the geometrical location of the transmitter, the receiver, and scatterers. The channel model applied the electromagnetic laws of LoS, reflection, diffraction, and scattering for the position of the transmitter, the receiver, and scatterers to compute

the channel characteristics. The GBSMs are suitable to build the mobile-to-mobile channel model due to the good trade-off between the simulation accuracy and the computational burden [45].

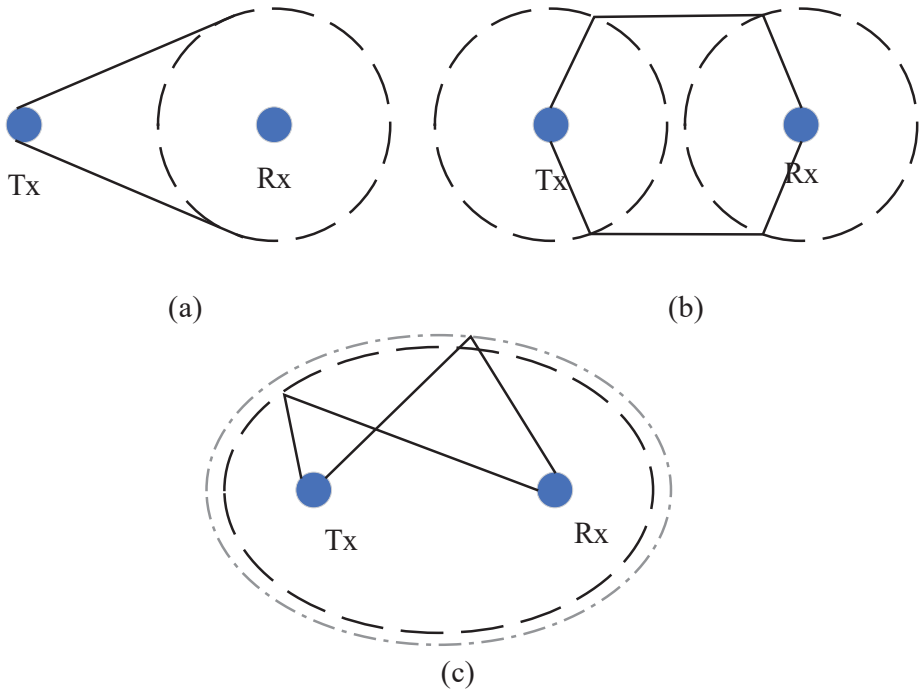

Fig. 2.2 The three typical GBSMs: (a) One-ring model; (b) Two-ring model; (c) Elliptical model. The Tx and Rx denote transmitter and receiver, respectively.

The often-used GBSMs can be classified as the one-ring model, the two-ring model, and the elliptical scattering model, as shown in Fig. 2.2 [46]. For some 3D cases, the cylinder scattering model will be used to express the position of the transmitter and the receiver accurately [47]. The one-ring model is often used to describe the simple environment, where the receiver is surrounded by many scatterers in one circle [48]. The two-ring model assumes that scatterers surround the transmitter and the receiver by independent two circles, where the transmitter and the receiver are set as the centre of the scatterer's circle. The one-ring model and the two-ring model are often used in the narrowband communication system because they are frequency non-selective [48]. Furthermore, the method of elliptical models for setting scatterer is to draw a set of ellipses with varying focal lengths whose foci correspond to the transmitter and

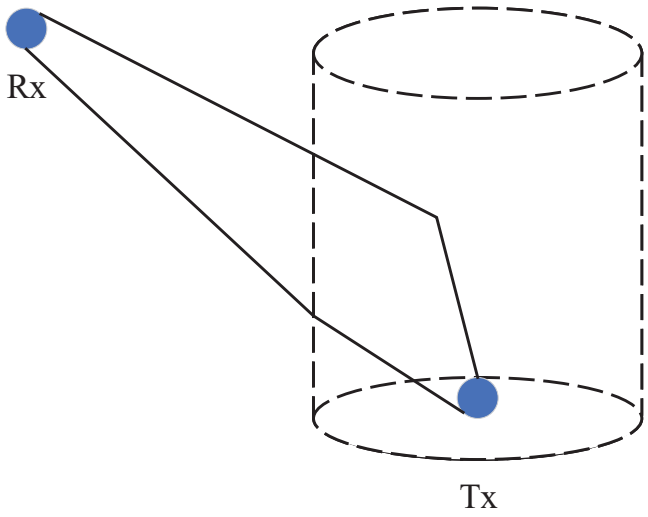

Fig. 2.3 The 3D cylinder GBSM. The Tx and RX denote transmitter and receiver, respectively.

the receiver position [49], which is suitable to model the wideband channel in the communication system.

The cylinder scattering model has a similar process to the previously described GBSMs, but the difference is one of the transmitter and receiver set with the elevation angle and height value. The scatterers surround the transmitter and receiver on the setting cylinder model. The schematic diagram of the cylinder scattering model is shown in Fig. 2.3, where the solid lines stand for the propagation rays from transmitter to receiver through the scatterer in the 3D GBSM model. The 3D GBSM model with cylinder model is also derived in many papers for vehicle-to-vehicle (V2V) communications and UAV communications [50].

There is another classification method of GBSMs considering whether scatterers are placed in regular shape or not. For these aforementioned typical models, the shape of the scatterers placed is regular, so they are also called regular-shaped GBSM. In contrast, the irregular-shaped GBSM places the scatterers randomly with the specified statistical distribution [51]. Irregular-shaped GBSM can capture the physical characteristics well and reproduce the physical reality of effective scatterers.

2.2.2 UAV A2G Channel Measurement Campaigns

In this subsection, the behaviour of the UAV A2G propagation channel could be better understood via field measurements. In general, the UAV A2G channel characterization is related to the operational environment, channel sounding process, antenna configuration, UAV types, and UAV dynamics setting (altitude and velocity).

In the early A2G channel measurements stage, the small-sized FW manned aircraft were used, which flew at a high altitude. For instance, a Cessna-172s aircraft was used to evaluate the performance of a multiple-input multiple-output (MIMO) system at 2.4 GHz for the A2G channel in the urban, suburban, and over sea scenarios. The flight height is about 1000 m (10500 ft), which is too high to evaluate the current UAV A2G channel but supports the further learning of the A2G channel in the early stage [52].

Recently, low-altitude UAVs were used to help learn the A2G channel at a low cost [53–59]. For example, the FW or RW UAV was used to comprehend the A2G channel characteristics in different scenarios. For general UAV measurement, the UAV payload is including the global positioning system (GPS) system to record the flight path, wireless equipment to transmit/collect data, and a video camera to record the flight dynamics [57].

In [53], the measurement campaign was performed in a suburban area of Shanghai, China, using a 2.585 GHz continuous wave (CW) transmitter with a bandwidth of 18 MHz. The RW UAV flew between 0 to 300 m above the ground. The authors have characterized the power delay profile (PDP), Rician K-factor of the wireless channel, root-mean-square (RMS) delay spread, and cumulative distribution function (CDF) of residuals of K-factor. Similar scenario measurement in Victoria, Australia, for a path loss model and shadow fading with a flight height between 30 to 120 m were conducted. The wireless equipment was a typical Android phone using long-term evolution (LTE) technology at 850 MHz [57]. A related measurement campaign was conducted with a similar band and technology to analyse the UAV A2G channel over cellular networks in Fyn, Denmark, for a path loss model and shadow fading in a rural area with a flight altitude between 15 to 120 m [56].

In [54], the authors used an iPhone 5s as the wireless equipment to measure the time and frequency dispersion of the A2G channel in residential and mountainous desert terrains.

Table 2.2 Summary of measurement campaigns

Ref.	**Freq.**	**UAV**	**Scenario**	**Antenna**	**Altitude**	**Channel Statistics**
[53]	2.585 GHz	RW	Suburban	SISO	0-300 m	PDP, K, RMS, CDF
[54]	5.8 GHz	RW	Residential	Phone	100 m	RMS, DS, CDF
[55]	0.9 GHz	FW	Rural	MIMO	0-274 m	P_r
[56]	0.8 GHz	RW	Rural	SISO	15-120 m	PL, SF
[57]	0.85 GHz	RW	Suburban	Phone	30-120 m	P_r, PL, SF
[58]	0.9 GHz	FW	Rural	MIMO	200 m	RMS, P_r, SD, OR
[59]	2.4 GHz	RW	Urban	SISO	125m	P_r, CDF
SISO: single-input-single-output, MIMO:multiple-input-multiple-output, PDP: power delay profile, K: Rician factor, RMS: RMS delay spread, CDF: cumulative distribution function, DS: Doppler spread, P_r: received power, PL: path loss, SF: shadow fading, SD: spatial diversity, OR: outage rate						

They studied the time and frequency variations of the UAV A2G channel by evaluating the RMS delay and the Doppler spread. In [59], urban and bay areas in the Yokohama City and the Shinjuku Ward were analysed using 925 MHz and 2.4 GHz omnidirectional antenna, respectively. They found the CDF of 2.4 GHz shows time-dependent in the urban area, which was distinct from the bay area.

In [55], the measurement campaign was performed in a rural area using 2.4 GHz and 5.8 GHz common off-the-shelf (COTS) 802.11 equipment. The FW UAV flew between 0 to 274 m above the ground. The authors have characterized the received power with the MIMO system. In [58], the authors used the FW UAV at 900 MHz with the MIMO system to characterize RMS delay spread, received power, spatial density, and outage rate. In Table 2.2, the aforementioned measurement campaigns has been summarized.

2.2.3 UAV A2G Channel Models

The reliable analytical A2G channel modelling approaches, which can be categorized as deterministic models and GBSMs, are necessary to characterize the propagation behaviour of the UAV channel [22]. In [60], the authors proposed a ray-tracing propagation channel for low-altitude UAVs in suburban compared with measurements, where the impact of UAV altitude on PDP and RMS delay spread was studied. In [61], the authors investigated the

narrowband and wideband characteristics of the A2G link, e.g., received power, CIR, and RMS delay spread, in urban environment using ray-tracing simulation. In [62], the authors derived a theoretical path loss model considering different tilts of mountain reflections by comparing it with the ray-tracing simulation. The PDP is analysed for the speed of the UAV and the multipath of mountain reflection could be distinguished well. In [63], the authors investigated the UAV A2G narrowband propagation in the urban scenario by the ray-launching tool to analyse the impact of UAV heights and transmission frequencies on path loss. In [64], the authors introduced the Doppler effect caused by propellers' rotation of the RW UAV A2G channel. It also points out that motor vibration could have a significant effect on the UAV A2G communication channel.

GBSMs are popular for analysing the channel characteristics of UAV wireless communication channels, which provides a trade-off between the computational complexity and the accuracy, e.g., in [47, 50, 65–69]. In [65], the authors proposed a 3D cylinder GBSM with the sum of the LoS and non-LoS (NLoS) components for wideband non-stationary Ricean fading channels. The time-varying parameter of angles spread and expressions of the space-time correlation function of the UAV are derived to properly describe channel properties. In [66], a 3D geometry-based UAV-MIMO channel model in the A2G link was adopted in an elliptic-cylinder model to indicate the spatial correlation function for the high mobility of the UAV. The UAV transmitter mobility and ground reflection of the propagation are firstly investigated in the UAV A2G channel model. Moreover, Zhu *et al.* [47] and Jia *et al.* [67] proposed a 3D cylinder GBSM UAV-MIMO channel model for the non-stationary situation, which studied the time-variant ACF, cross-correlation function, Doppler PSD, level-crossing rate, and average fading duration. The path number, the path delay, and the angle parameter are analysed at the angles of arrival (AoA) following the Von Mises distribution and the angles of departure (AoD) following the Laplacian distribution. Subsequently, Chang *et al.* [50] and Jiang *et al.* [68] proposed a 3D wideband GBSM UAV-V2V channel model, which assumes that effective scatterers around the ground receiver and distributed on the surface of an ellipse. The A2G V2V channel model has studied the impacts of different UAV altitudes, A2G elevation angles, and scatterers altitudes on channel characteristics. In [69], the nar-

Table 2.3 Summary of UAV A2G channel models

Ref.	Scenario	Method	Channel Statistics
[60]	Suburban	Ray-tracing	PDP, RMS
[61]	Urban	Ray-tracing	P_r, RMS, CIR, ToA
[62]	Mountain	Ray-tracing	PDP, PL
[63]	Urban	Ray-launching	PL
[64]	-	-	DS
[47]	-	GBSM	AoA, AoD, ACF, CCF, DPSD, LCR, AFD
[50]	Urban	GBSM	P_r, RMS, AoD, AoA, CCF, ACF, DPSD
[65]	-	GBSM	AoD, AoA, CCF, ACF, DPSD
[66]	Urban	GBSM	CCF
[67]	-	GBSM	ACF, CCF
[68]	Urban	GBSM	P_r, RMS, AoD, AoA, CCF, ACF, DPSD
[69]	-	GBSM	AoA, AoD, ACF, CCF, DPSD, LCR, AFD

PDP: power delay profile, RMS: RMS delay spread, P_r: received power, CIR: channel impulse response, ToA: mean time of arrival, PL: path loss, DS: Doppler spread, AoA: angle of arrival, AoD: angle of departure, ACF: temporal auto-correlation function, CCF: spatial cross-correlation function, DPSD: Doppler power spectrum density, LCR: level-crossing rate, AFD: average fading duration

rowband 3D UAV MIMO GBSM Ricean fading channel was investigated consisting of LoS component, single-bounces rays, and double bounced rays. The non-stationary UAV-MIMO channel was proposed in a two-cylinder model, which is different from the aforementioned works.

The summary of aforementioned UAV A2G channel models is shown in Table 2.3.

2.2.4 Millimetre-wave UAV A2G Channel Models

To this end, the research on the millimetre-wave UAV A2G propagation channel is still in its infancy. The millimetre-wave FW UAV-MIMO GBSM, which used the birth-death process to model the non-stationary property of scatterers in the millimetre-wave UAV A2G link, was proposed in [71]. The temporal ACF, spatial CCF, and Doppler PSD are analysed for geometrical characteristics of the regular shaped GBSM. In [76], the authors proposed a 3D wideband non-stationary millimetre-wave UAV MIMO GBSM with heterogeneous scattering sources, i.e., far and local clusters, which can describe the UAV propagation

Table 2.4 Summary of millimetre-wave UAV A2G channel models

Ref.	Freq.	Scenario	Method	Channel Statistics
[70]	60 GHz	Urban	-	OP
[71]	28 GHz	Urban	GBSM	ACF, CCF, DPSD
[72]	28 & 60 GHz	Urban, suburban, rural, over sea	Ray-tracing	P_r, RMS
[73]	28 & 60 GHz	Urban, suburban, rural, over sea	Ray-tracing	P_r, ToA, AoD, AoA
[74]	100 GHz	Urban	Hybrid model	PL, RMS, PDP, AoA
[75]	28 GHz	Urban	Hybrid model	P_r, RMS, AoD, AoA
[76]	28 GHz	-	GBSM	ACF, CCF, DPSD

OP: outage probability, ACF: temporal auto-correlation function, CCF: spatial cross-correlation function, DPSD: Doppler power spectrum density, P_r: received power, RMS: RMS delay spread, ToA: mean time of arrival, AoA: angle of arrival, AoD: angle of departure, PL: path loss, PDP: power delay profile

scenarios precisely. The local mobile cluster leads to a higher time correlation and narrower quasi-stationary interval compared with the local stationary cluster.

The work in [70] proposed analytical channel models for direct UAV-to-UAV link, aerial relay link, and relay link under hovering fluctuations situation. Furthermore, the outage probability of a UAV-to-UAV millimetre-wave link and the end-to-end SNR for two relay scenarios is analysed. In [72] and [73], the authors used a ray-tracing tool to characterize the millimetre-wave propagation channel for the A2G link at 28 GHz and 60 GHz with different UAV heights in urban, suburban, rural, and over sea situations. The RMS delay spread will decrease when UAV height increase for suburban and rural scenarios and the millimetre-wave A2G channel characteristics are dependent on the relative height between scatterers and UAVs. In [74], the authors analysed the UAV A2G channel characteristics, i.e., the path loss, the excess delay, the PDP, and the AoA, for the urban environment at 100 GHz by the ray-tracing method. Then, these channel characteristics from the ray-tracing are extracted to support the stochastic channel model to generate the multipath components.

In [75], the authors proposed a hybrid channel model by using statistical results from the ray-tracing method to obtain the CIR and angle evolution characteristics. Especially, the hybrid channel model combines the ray-tracing model and the GBSM, which is used in the

millimetre-wave UAV A2G propagation channel to achieve simulation accuracy and reduce the computational burden [44]. The ray-tracing model is used to compute deterministic rays for large-scale and the GBSM is used to compute time-variant characteristics following scatterers deployment.

The summary of the aforementioned millimetre-wave UAV A2G channel models is shown in Table 2.4. Moreover, to summarize, none of the state-of-the-art UAV A2G channel models has studied the Doppler effect brought by the UAV wobbling at hovering status in millimetre-wave bands.

2.3 Review of UAV A2G Link Performance Analysis

In this section, parameters used to evaluate the UAV A2G link performance are introduced. The LoS probability, coverage probability, throughput, and energy management are discussed and optimized from aspects of UAV height, UAV trajectory, and UAV deployment.

2.3.1 Line-of-sight Probability and Coverage Probability

The LoS probability and the coverage probability are two important parameters to evaluate the UAV A2G link performance and they are always discussed together in the literature. The LoS probability and the coverage probability are first discussed in LAP by [11]. The LoS probability is modelled based on the International Telecommunication Union (ITU) work [77] and simplified to the Sigmoid function form is shown below

$$\mathbf{P}(\mathrm{LoS},\theta) = \frac{1}{1+a\exp\left[-b(\theta-a)\right]}, \tag{2.3}$$

where a and b are called here the S-curve parameters, and θ is depicted angle. Then, the average path loss related to the LoS probability is derived as

$$\Lambda = \mathbf{P}(\mathrm{LoS}) \times \mathrm{PL}_{\mathrm{LoS}} + \mathbf{P}(\mathrm{NLoS}) \times \mathrm{PL}_{\mathrm{NLoS}}. \tag{2.4}$$

The path loss of the LAP for the urban environment was derived in [78], where the set of path loss model parameters in suburban, urban, dense urban, and high-rise urban are proposed. According to the different transmission scenarios, the different service threshold in terms of the maximum allowable path loss is defined. This maximum allowable path loss could be translated into a UAV A2G link working coverage of radius. Therefore, the optimum LAP altitude to maximise the coverage on the ground is proposed analytical. The coverage probability could be computed through the probability of the UAV A2G path loss over the maximum allowable path loss.

Based on basic work in [11], there many extended works are published. The optimal location of UAVs could support adjusting the A2G networks' reliability by adding the relay node. In [79], the authors proposed two mobility models of 3D mobile UAVs considering the UAV vertical and spatial movement processes, which are the mixed mobility model and the uniform mobility model, to analyse the UAV coverage probability. In [80], the authors studied the coverage of UAV as a base station with variable height and variable horizontal distance in the millimetre-wave band, where the optimum placement of UAV is found. The coverage probability of multiple UAVs from an aerial network to relay the ground node's data was derived in [81]. Furthermore, the generic framework with height-dependent path loss, small-scale fading, and ground-to-ground channel model is used to analyse and optimize the UAV A2G systems, where the outage probability is minimised and coverage range is maximised [82]. The probability of LoS in the urban environment for the UAV communications was derived in [83], where the footprint of the building adopted the log-normal distribution for suburban, urban, and high-rise urban. The imperfect CSI raised from estimation errors degrades system performance for the UAV communications, the optimum altitude of the UAV communications under imperfect CSI is computed by an algorithm in an urban environment [84].

2.3.2 Throughput

The throughput and capacity of the communication system is the vital parameter to express how effective the designed system. In [85], the authors derived the relationship of the

coverage probability versus SNR threshold and the expected rate versus the range of minimum SNR based on path loss from [11]. This work helps the UAV to optimize the altitude and power to achieve the quality-of-services requirements. The optimum altitude of multiple UAVs to maximise the sum rate of the ground network is computed in [81], where extending the system from a single UAV to multiple UAVs. In [86], the authors analysed the average ergodic rate and the area spectral efficiency for different heights and densities of UAVs. The impact of network densification and the imperfect CSI on the capacity were analysed for the UAV A2G link in Ricean Fading channels [87]. The ergodic and outage capacity between multiple UAVs or UAV swarms in 3D spaces are analysed at different fixed altitudes and A2G links with the 3D UAV trajectory. With the internet of things (IoT) network, the optimum UAV deployment to maximise the collection of data from the IoT device is studied.

The algorithm for optimizing trajectories of multiple UAVs and the height of UAVs to maximise the data rate is proposed to support the IoT UAV-associated network [88]. Apart from optimizing the trajectories and heights of UAVs, the UAV speed is another parameter to optimize the sum rate for the UAV network [89]. The throughput for UAV-enabled wireless powered communication networks is maximised by optimizing the trajectories and the speed of UAVs [90]. The optimal UAV hovering location and UAV trajectories are analysed considering the wireless powered communication and wireless information transfer. To summarize, the throughput performance of the UAV A2G link under UAV wobbling in millimetre-wave bands has not been sufficiently studied from the modulation and link transmission process perspectives.

2.3.3 Energy Minimisation and Energy Efficiency

The endurance and the performance of UAV systems are fundamentally restricted by the on-board battery. The total energy consumption of the UAV includes communication-related energy and propulsion energy. The communication-related energy is caused by radiation, signal processing and other circuitry and the propulsion energy supports the UAV mobility and hovering. The propulsion energy model for the FW UAV [91] and for the RW UAV [23] are derived to help minimise the total energy of the UAV working. Since UAV trajectory

optimization is the main method to minimise the total energy consumption, the propulsion energy of the UAV is the vital parameter.

The EE of the FW UAV with generally constrained trajectories and circular trajectories are analysed in [91]. For the RW UAV enable IoT system, the maximum energy consumption among all devices was minimised while satisfying the UAV energy budget by optimizing the UAV trajectory and the UAV speed [92]. For the RW UAV, the hovering time is a vital parameter to maximise the EE for UAV-based heterogeneous networks. The multiple UAVs situation for two-tier heterogeneous networks is considered to maximise the EE of the system by optimizing UAV hovering time [93]. Moreover, in [24], the authors proposed power allocation mechanisms for fixed BSs and steady UAVs to maximise the system sum rate or minimise the system power consumption of a UAV-assisted millimetre-wave heterogeneous cellular network. In [94], the authors proposed an efficient algorithm to maximise the achievable rate by jointly optimizing the UAV's 3D trajectory and transmission power subject to the UAV flight altitude and transmission power constraints. To summarize, the power control policy of the UAV A2G link under UAV wobbling in millimetre-wave bands has not been studied to minimise the communication consumption power and the EE performance of the UAV A2G link under UAV wobbling has not been evaluated.

2.4 Summary

UAV communications and millimetre-wave techniques have attracted much research attention as they enable great performance enhancement, and are compelling for 5G networks to meet the emerging applications for increasing demands of the throughput along with the EE.

The basic millimetre-wave propagation model including the free space path loss model and the log-distance path loss model is investigated firstly. The 28 GHz and 60 GHz frequency bands are popular in the published literature. Moreover, the Doppler effect of the millimetre-wave A2G link is severe because of the millimetre-wave frequency band and the mobility of the UAV.

The basic deterministic channel model and stochastic channel model are introduced to support understanding the UAV A2G channel model better. The UAV A2G channel measurement campaigns and the UAV A2G channel model are reviewed along with the system limitation and challenges, followed by the UAV A2G system performance evaluation. The channel characteristics of the UAV A2G channel are presented, e.g., path loss, received power, the Doppler DSP, temporal ACF and RMS delay spread. We note that the impact of UAV wobbling in the millimetre-wave A2G wireless channel and the combination of the adaptive modulation and the power control policy for wobbling millimetre-wave UAV A2G links to maintain the maximum achievable transmission rate has not been studied in the published literature.

In the upcoming chapter, the impact of UAV wobbling on the millimetre-wave UAV A2G wireless channel is investigated to support the UAV A2G network design, followed by the UAV A2G link performance evaluations from the throughput perspective and the power-saving perspective.

Chapter 3

Impact of UAV Wobbling on Millimetre-wave A2G Wireless Channel

Overview

Millimetre-wave UAV A2G links face unpredictable Doppler effects arising from the inevitable wobbling of the UAV. Moreover, the time-varying channel characteristics during transmission lead to unstable UAV A2G links. This chapter studies the impact of mechanical wobbling on the Doppler effect of the millimetre-wave wireless channel between a hovering RW UAV and a ground node. Original contributions of this chapter lie in the following: i) Modelling the wobbling process of a hovering RW UAV; ii) developing an analytical model to derive the temporal ACF for the millimetre-wave RW UAV A2G link in a closed-form expression; and iii) investigating how RW UAV wobbling impacts the Doppler effect on the millimetre-wave RW UAV A2G link. Numerical results show that different RW UAV wobbling patterns impact the amplitude and the frequency of ACF oscillation in the millimetre-wave RW UAV A2G link. For UAV wobbling, the temporal ACF decreases quickly and the impact of the Doppler effect is significant on the millimetre-wave A2G link.

3.1 Introduction

In the 5G era, UAV A2G links have been widely investigated to facilitate numerous applications such as flexible coverage and capacity enhancements, emergency assistance, disaster relief, etc. [1, 2]. Moreover, the integration of the UAV technique and millimetre-wave communications has been proposed to provide a high data rate UAV A2G link to support these applications[70]. The miniaturization of the aerial base station for UAV carrying could be realized due to the small wavelength in millimetre-wave frequency [6].

However, in a UAV A2G link, the UAV hovering in the air may experience mechanical wobbling in the millimetre scale owing to the imperfect mechanical control and various environmental issues, such as wind gusts, bad weather, and high vibration frequency of their propellers and rotors [21, 95]. In other words, the UAV can be seen as a mobile transceiver with the non-negligible velocity in hovering status, which leads to a severe Doppler effect in the millimetre-wave RW UAV A2G link [25, 26]. Moreover, time-varying channel characteristics in the A2G link lead to the outdated channel state information from the channel estimation, resulting in deteriorated BEP performance of the UAV A2G link [96]. Therefore, to reap the benefits of the millimetre-wave RW UAV communications, the wireless channel for the millimetre-wave UAV A2G link should be distinctly characterized with regard to the Doppler effect.

A handful of UAV A2G research works have considered the wobbling of RW UAV [21, 64, 70]. In [70], the authors discussed the antenna mismatch of the transmitter and the receiver caused by wobbling in the millimetre-wave RW UAV A2G link. In [21], the authors studied the impact of UAV wobbling on the coherence time of the wireless channel using Rician fading. In [64], the authors analysed the impact of propellers' rotation on the Doppler shift of the RW UAV A2G channel. Since the FW UAV requires continuous stable high-speed mobility, the Doppler effect in the FW UAV A2G link can be analysed and compensated by using the space-time correlation function for non-stationary UAV scenarios [79]. To summarize, none of the state-of-the-art UAV A2G channel models has studied the Doppler effect brought by the wavelength-scale mechanical wobbling at hovering status in millimetre-wave bands.

In this chapter, the first attempt to analytically investigate the impact of UAV mechanical wobbling on the Doppler effect in millimetre-wave UAV A2G links is presented. Specifically, the temporal ACF and the Doppler PSD of millimetre-wave RW UAV channel under mechanical wobbling are derived. The major contributions of this chapter are summarized as follows:

- The RW UAV movement model at hovering status under mechanical wobbling is introduced. Two parameters, i.e., the vibration frequency and the velocity envelope covariance, are defined to capture characteristics of UAV mechanical wobbling.

- The temporal ACF of the millimetre-wave RW UAV A2G link is derived in a closed-form expression based on RW UAV mechanical wobbling movement model at hovering status. The analytical expression of the temporal ACF is verified by Monte-Carlo simulations.

- The Doppler PSD of the millimetre-wave RW UAV A2G link with mechanical wobbling is computed based on the analytical temporal ACF.

- A 3D non-stationary GBSM is proposed for the millimetre-wave RW UAV A2G link under UAV wobbling. Then, this model employs the a single cylinder geometry and combines the LoS and single-bounced (SB) components, which is a supplement model for the analytical model.

- Numerical results show that the temporal ACF decreases quickly and the impact of the Doppler effect is significant in the millimetre-wave A2G link while the RW UAV is under random mechanical wobbling. The temporal ACF oscillates with a reducing amplitude, which is mainly impacted by the vibration frequency and the velocity envelope covariance, respectively.

The proposed analytical model of the temporal ACF and the Doppler PSD will be applied to predict the impact of the mechanical wobbling on the Doppler effect in millimetre-wave RW UAV A2G links.

The rest of this chapter is organized as follows. In Section II, the system model and assumptions of the RW UAV mechanical wobbling at hovering status of the millimetre-wave UAV A2G link are presented. In Section III, analytical results of the temporal ACF and the Doppler PSD of the millimetre-wave RW UAV A2G link under mechanical wobbling are derived. In Section IV, a 3D non-stationary GBSM for the millimetre-wave RW UAV A2G link under UAV wobbling is proposed. In Section V, impacts of UAV mechanical wobbling on millimetre-wave RW UAV channel at hovering status are discussed. Finally, in Section VI, main conclusions are drawn.

3.2 System Model

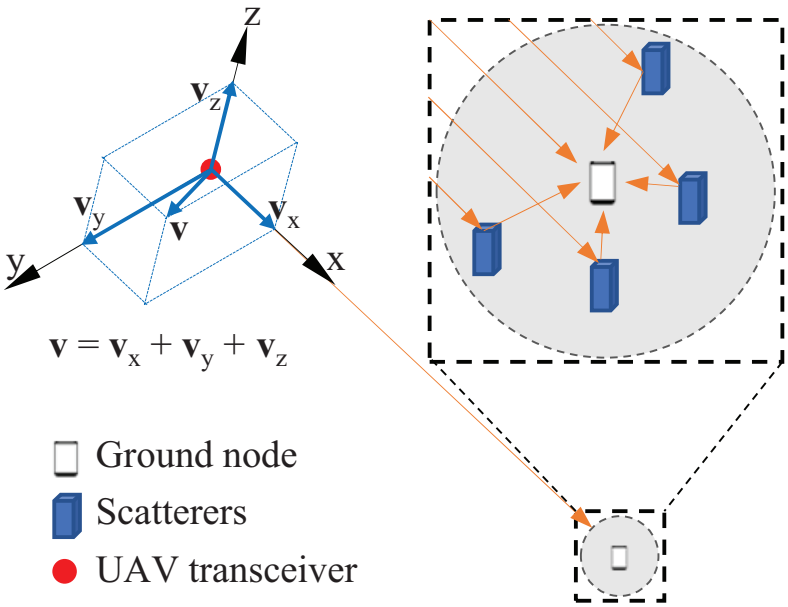

Fig. 3.1 The millimetre-wave UAV A2G link with UAV mechanical wobbling.

In this section, the system model and assumptions in the millimetre-wave RW UAV A2G link are introduced. Then, the UAV wobbling movement process of the millimetre-wave RW UAV A2G link is derived.

In this study, a millimetre-wave UAV A2G link between a hovering UAV and a ground node is designed for analysing the UAV A2G channel model. As shown in Fig. 3.1, the UAV

is equipped with a single horn directional antenna (transceiver) located at the bottom of the UAV platform. The directional horn antenna supports the directional beam to overcome high attenuation of the millimetre-wave propagation [97, 98]. According to Fig. 3.1, the velocity of UAV mechanical wobbling is denoted as $\mathbf{v}$, which could be superposed by following a Cartesian coordinate system, i.e., $\mathbf{v} = \mathbf{v}_{\mathrm{x}} + \mathbf{v}_{\mathrm{y}} + \mathbf{v}_{\mathrm{z}}$. Moreover, one axis direction of a Cartesian coordinate system is set in the same direction as the UAV A2G link to support the following analysis. More specifically, in Fig. 3.1, the x-axis is set as the same direction as the link and the radial velocity between the UAV and the ground node is $\mathbf{v}_{\mathrm{x}}$.

All key assumptions applied in this chapter are listed as follows.

Assumption 1. *The hovering height of the RW UAV is much higher than those of buildings and other scatterers to keep the LoS wireless A2G link, as in [99]. Moreover, the probability of the LoS link between the RW UAV and the BS is high and the dominant propagation mechanism is free space transmission [16]. When the UAV is hovering at a high altitude, for the multipath channel model, scatterers nearby the ground node will be considered together. Therefore, all links in this chapter based on Assumption 1 are assumed as LoS links.*

Assumption 2. *The velocity of UAV mechanical wobbling is the superposition of the radial velocity and the tangential velocity in the millimetre-wave RW UAV A2G link, which is shown in Fig. 3.1. The tangential velocity of the UAV wobbling may lead to the variation of angles of arrival and departure in the UAV A2G link, which could affect the Doppler effect in the UAV A2G channel model. However, this effect could be negligible when the ground node position is fixed and the RW UAV is hovering at a high altitude [73], which are defined in Assumption 1. Therefore, the Doppler effect in the proposed model is only caused by the radial velocity of the RW UAV wobbling. The radial velocity, denoted by $V(t)$, to describe the wobbling movement of the RW UAV is modelled [100].*

Assumption 3. *Since the RW UAV mechanical wobbling has period property, $V(t)$ is assumed periodical variation in the time domain [21, 64]. Moreover, the envelope of velocity is time-varying in practical scenarios. Therefore, the value of time-varying $V(t)$ is assumed as*

$$V(t) = a(t)\cos(\omega_{\mathrm{v}} t + \phi_0), \tag{3.1}$$

where $a(t)$ is the random amplitude envelope of the radial velocity under the RW UAV wobbling, ω_{v} is the mechanical vibration frequency from rotor, t is the time, and ϕ_0 is the random phase at $t = 0$, which is uniformly distributed from 0 to 2π.

Assumption 4. *For the sake of simplicity, $a(t)$ is assumed to be a stationary Gaussian random process with the distribution $\mathcal{N}(0, \sigma_{\mathrm{v}}^2)$. In practical scenarios, the radial velocity of the RW UAV wobbling may be influenced by wind gusts and mechanical vibration. Therefore, the autocorrelation of $a(t)$ and $a(t+\Delta t)$ is assumed as $\mathrm{E}[a(t)a(t+\Delta t)] = \sigma_{\mathrm{v}}^2 e^{-\mu\Delta t}$, where σ_{v}^2 is the variance of the radial velocity and μ is the parameter to measure how fast the envelope of radial velocity changes with time.*

Based on Assumption 3, the wobbling distance $d(t)$ of the hovering RW UAV system is calculated by

$$d(t) = \int_0^t V(t)\,\mathrm{d}t = \int_0^t \mathrm{Re}\left\{a(t)\,e^{j\omega_{\mathrm{v}}t+\phi_0}\right\}\mathrm{d}t. \tag{3.2}$$

Based on all assumptions, patterns of the UAV wobbling movement are summarized as follows:

- When $\mu \neq 0$ and $\omega_{\mathrm{v}} \neq 0$, the UAV wobbling movement is influenced by the random mechanical vibration and the autocorrelation of the movement velocity simultaneously.
- When $\mu = 0$ and $\omega_{\mathrm{v}} = 0$, the UAV moves towards to a random direction with a stationary Gaussian distributed velocity, like the FW UAV.
- When $\mu \neq 0$ and $\omega_{\mathrm{v}} = 0$, the UAV wobbling movement does not have the mechanical vibration but moves randomly with the temporally correlated velocity, i.e., wind guts.
- When $\mu = 0$ and $\omega_{\mathrm{v}} \neq 0$, the UAV wobbling movement is influenced by the mechanical vibration with a stationary amplitude of the movement velocity.

In this chapter, the average wobbling movement distance of different UAV movement patterns is defined as

$$\sigma_{\mathrm{d}} = \sqrt{\mathrm{E}\left[|d(t) - d(t+\Delta t)|^2\right]}. \tag{3.3}$$

Lemma 3.1. When Δt approaches infinity, the variance of vibration distance σ_{d}^2 is computed by

$$\sigma_{\mathrm{d}}^2 = \begin{cases} \sigma_{\mathrm{v}}^2 \frac{\mu \Delta t}{\omega_{\mathrm{v}}^2 + \mu^2}, & \mu \neq 0, \omega_{\mathrm{v}} \neq 0, \\ \sigma_{\mathrm{v}}^2 \frac{(\Delta t)^2}{2}, & \mu = 0, \omega_{\mathrm{v}} = 0, \\ \sigma_{\mathrm{v}}^2 \frac{\Delta t}{\mu}, & \mu \neq 0, \omega_{\mathrm{v}} = 0, \\ \sigma_{\mathrm{v}}^2 \frac{1-\cos(\omega_{\mathrm{v}} \Delta t)}{\omega_{\mathrm{v}}^2}, & \mu = 0, \omega_{\mathrm{v}} \neq 0. \end{cases} \tag{3.4}$$

Proof. See Appendix A.1. □

To validate Lemma 1, σ_{d}^2 are plotted against Δt in Fig. 3.2. The simulator computes the averaged wobbling distance based on (3.2) and (3.3). These simulation processes require time-consuming repetition of different UAV wobbling velocity generation to estimate the variance of vibration distance σ_{d}^2, which is compared with the analytical results computed by (3.4). Since the motor vibration frequency is high, the time separation of UAV movement caused by motor vibration will be on a millisecond scale, where the simulation time range is large enough to consider the Δt approaching infinity. The following observations are made therein.

- The analytical results match the simulation well.
- Except for the scenario with $\mu = 0$ and $\omega_{\mathrm{v}} \neq 0$, σ_{d}^2 increases with Δt enlarging.
- For the scenario with $\mu = 0$ and $\omega_{\mathrm{v}} \neq 0$, the UAV moves periodically.
- ω_{v} has a significant impact on the amplitude of σ_{d}^2.

According to [101], the CIR of the RW UAV channel with the mechanical vibration can be written as the function of the UAV wobbling distance, i.e.,

$$h(t) = h_0 e^{j\frac{\omega_{\mathrm{c}}}{c} \int_0^t \mathrm{Re}\left\{a(t) e^{j(\omega_{\mathrm{v}} t + \phi_0)}\right\} \mathrm{d}t}, \tag{3.5}$$

where h_0 is the amplitude of the CIR, ω_{c} is the carrier frequency, and c is speed of light.

Assuming that $h(t)$ is stationary [65], the temporal ACF, defined by [102], is employed to characterize the time-varying characteristics of the wireless channel. Using the CIR defined

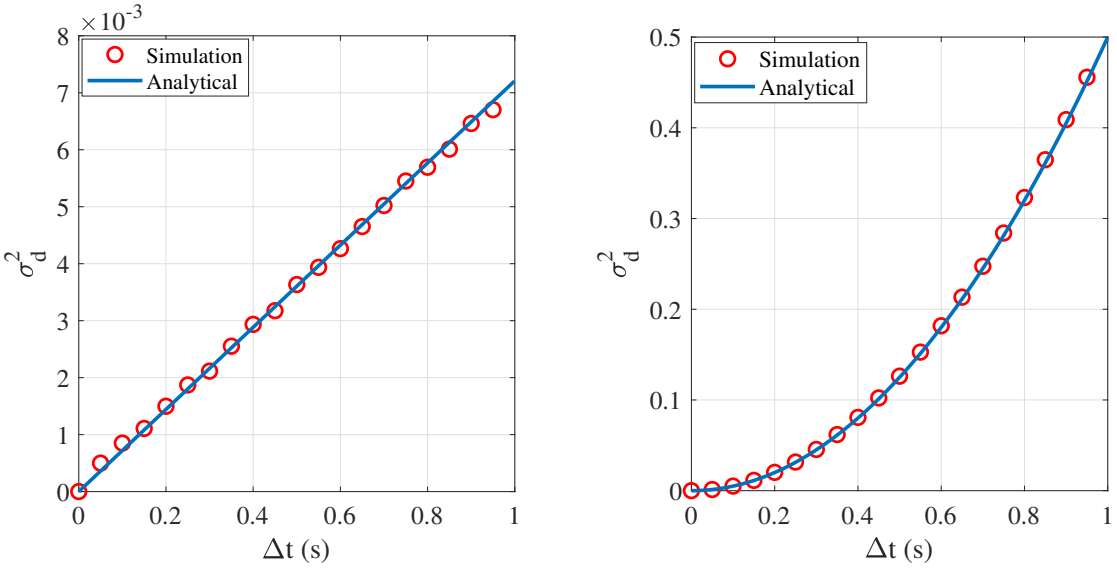

(a) $\mu = 40,\ \omega_v = 20\pi$

(b) $\mu = 0,\ \omega_v = 0$

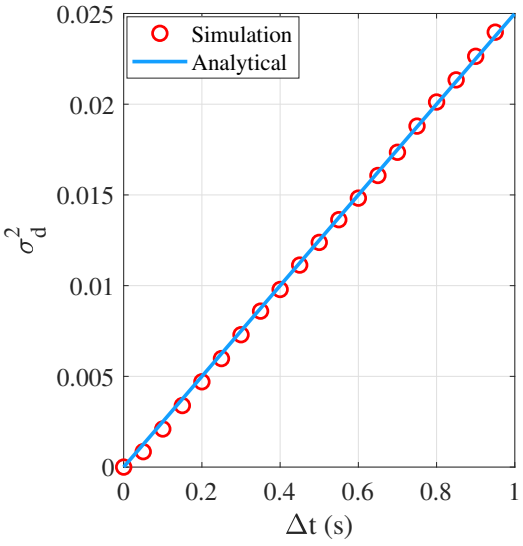

(c) $\mu = 40,\ \omega_v = 0$

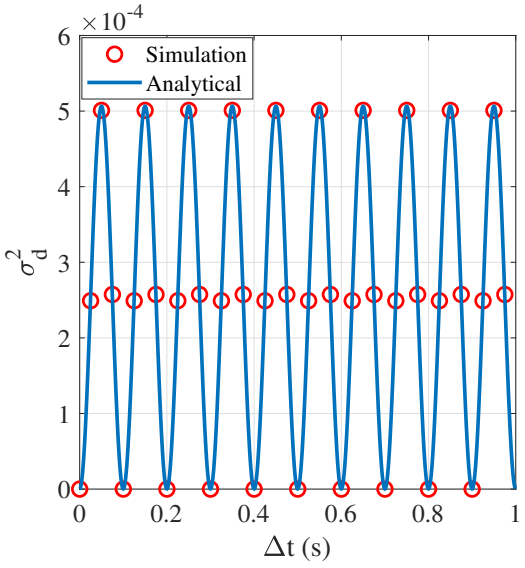

(d) $\mu = 0,\ \omega_v = 20\pi$

Fig. 3.2 The analytical and simulation σ_d^2 at different cases with $\sigma_v = 1$. Solid lines illustrate analytical results and makers show simulation results.

in (3.5), the temporal ACF can be computed by

$$C(\Delta t) = \frac{1}{|h_0|^2}\mathrm{E}\left[h(t)\,h^*(t+\Delta t)\right], \tag{3.6}$$

where $(\cdot)^*$ denotes the complex conjugate operator. When the received signal is non-stationary, the temporal ACF becomes a function of both t and $t+\Delta t$, and will be denoted as $C(t, t+\Delta t)$.

In the next section, $C(\Delta t)$ will be derived in a closed-form expression. Based on the closed-form temporal ACF, the Doppler PSD will be calculated.

3.3 Analytical Results

3.3.1 Closed-form Temporal ACF Expression

The closed-form expression of the temporal ACF is derived in this subsection.

Theorem 3.1. The temporal ACF, $C(\Delta t)$, can be computed by

$$\begin{aligned} C(\Delta t) = {} & e^{-0.5\sigma_{\mathrm{v}}^2\left(\frac{\omega_{\mathrm{c}}}{c\left(\omega_{\mathrm{v}}^2+\mu^2\right)}\right)^2\left(\mu\Delta t\left(\omega_{\mathrm{v}}^2+\mu^2\right)-2\mu\omega_{\mathrm{v}}\sin(\omega_{\mathrm{v}}\Delta t)e^{-\mu\Delta t}+\left(\mu^2-\omega_{\mathrm{v}}{}^2\right)\cos(\omega_{\mathrm{v}}\Delta t)e^{-\mu\Delta t}-\mu^2+\omega_{\mathrm{v}}{}^2\right)} \\ & \times J_0\left(j0.5\sigma_{\mathrm{v}}^2\left(\frac{\omega_{\mathrm{c}}}{c}\right)^2\frac{\mu\sin(\omega_{\mathrm{v}}\Delta t)-\omega_{\mathrm{v}}\cos(\omega_{\mathrm{v}}\Delta t)+\omega_{\mathrm{v}}e^{-\mu\Delta t}}{\left(\omega_{\mathrm{v}}^2+\mu^2\right)\omega_{\mathrm{v}}}\right), \end{aligned} \tag{3.7}$$

where $J_0(\cdot)$ denotes Bessel function of the first kind with an order zero.

Proof. See Appendix A.2. □

From Theorem 3.1, the closed-form expression of the temporal ACF given in (3.7) is directly applicable for $\mu \neq 0$ and $\omega_{\mathrm{v}} \neq 0$ scenario. Moreover, to apply results to the scenario with $\mu = 0$ or $\omega_{\mathrm{v}} = 0$, the temporal ACF for $(\mu \neq 0,\ \omega_{\mathrm{v}} = 0)$, $(\mu = 0,\ \omega_{\mathrm{v}} \neq 0)$, and $(\mu = 0,\ \omega_{\mathrm{v}} = 0)$ are derived as follows by using some straightforward derivations.

When $\mu \neq 0,\ \omega_{\mathrm{v}} = 0$, the temporal ACF, $C(\Delta t)$, is computed by

$$C(\Delta t) = \left[e^{-\frac{1}{2}\sigma_{\mathrm{v}}^2 \left(\frac{\omega_{\mathrm{c}}}{c\mu}\right)^2 \left(\mu\Delta t + e^{-\mu\Delta t} - 1\right)} \right] J_0 \left(j0.5\sigma_{\mathrm{v}}^2 \left(\frac{\omega_{\mathrm{c}}}{c\mu}\right)^2 \left(\mu\Delta t + e^{-\mu\Delta t} - 1\right) \right). \tag{3.8}$$

When $\mu = 0,\ \omega_{\mathrm{v}} \neq 0$, the temporal ACF, $C(\Delta t)$, is computed by

$$C(\Delta t) = \left[e^{-\frac{1}{2}\sigma_{\mathrm{v}}^2 \left(\frac{\omega_{\mathrm{c}}}{c\omega_{\mathrm{v}}}\right)^2 (1-\cos(\omega_{\mathrm{v}}\Delta t))} \right] J_0 \left(j\frac{1}{2}\sigma_{\mathrm{v}}^2 \left(\frac{\omega_{\mathrm{c}}}{c\omega_{\mathrm{v}}}\right)^2 (1-\cos(\omega_{\mathrm{v}}\Delta t)) \right). \tag{3.9}$$

When $\mu = 0,\ \omega_{\mathrm{v}} = 0$, the temporal ACF, $C(\Delta t)$, is computed by

$$C(\Delta t) = \left[e^{-\frac{\Delta t^2}{4}\sigma_{\mathrm{v}}^2 \left(\frac{\omega_{\mathrm{c}}}{c}\right)^2} \right] J_0 \left(j\frac{\Delta t^2}{4}\sigma_{\mathrm{v}}^2 \left(\frac{\omega_{\mathrm{c}}}{c}\right)^2 \right). \tag{3.10}$$

3.3.2 The Doppler PSD Expression

According to the Wiener-Khintchine Theorem, the PSD and the ACF are Fourier transform pairs under a wide-sense stationary random process [101]. The Doppler PSD of the proposed channel model can be computed by applying the Fourier transform of the temporal ACF with respect to time separation Δt [44],

$$F(f_D) = \int_{-\infty}^{\infty} C(\Delta t)\, e^{-j2\pi f_{\mathrm{D}}\Delta t} \mathrm{d}\Delta t, \tag{3.11}$$

where f_{D} is the Doppler frequency.

3.4 3D GBSM A2G Channel Model

A 3D UAV geometric model to reflect the millimetre-wave A2G link under wobbling is proposed in this section. In Fig. 3.3, the general description of the proposed GBSM including a LoS component and SB scattering components resulting from nearby and distant scatterers is presented. Fig. 3.4 shows the geometry relationships of the proposed model, where the locations of the UAV and the ground node are presented, respectively.

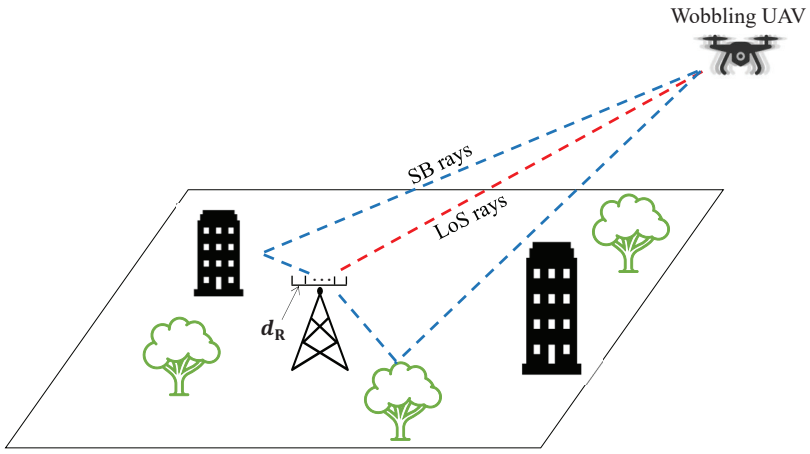

Fig. 3.3 A typical UAV A2G link scenario with LoS and SB scattering components.

In the preliminary stage, it is assumed that the UAV hovers in the air under wobbling and the ground node locates at the fixed position. The ground node is equipped with N_R antennas, while the UAV has a single antenna due to the weight and size constraints [103], where inter-element spacing between the elements is denoted by d_R at the ground node. The orientations of the ground node's antenna array in the azimuth plane (relative to the x-axis) is denoted as θ_R. H_T represents the hover height of the UAV. For the wobbling UAV, the moving direction can be described by the azimuth movement angle γ_T and the elevation movement angle ξ_T in real 3D scenarios. It is assumed that the UAV wobbling with speeds v_T.

Furthermore, it is assumed that there are N scatterers existing on the cylindrical ring around the ground node, and the n-th scatterer is defined as $S^{(n)}$, where $n \in (1,\ldots,N)$. The distance between the projection of $S^{(n)}$ on the x-y plane and the origin is denoted by $R_s^{(n)}$ and the height of $S^{(n)}$ is denoted by $H_s^{(n)}$. $\alpha_T^{(n)}$ and $\beta_T^{(n)}$ denote the azimuth angle of departure (AAoD) and elevation angle of departure (EAoD) of the wave that impinges on the effective scatterer $S^{(n)}$. $\alpha_R^{(n)}$ and $\beta_R^{(n)}$denote the azimuth angle of arrival (AAoA) and elevation angle of arrival (EAoA) of the wave travelling from an effective scatterer $S^{(n)}$.

According to Fig. 3.1, the velocity of UAV mechanical wobbling $\mathbf{v}$ could be superposed by following a Cartesian coordinate system, i.e., $\mathbf{v} = \mathbf{v}_x + \mathbf{v}_y + \mathbf{v}_z$. For wobbling process, the superposition velocity is random generated by (3.1). To simplify the latter calculation,

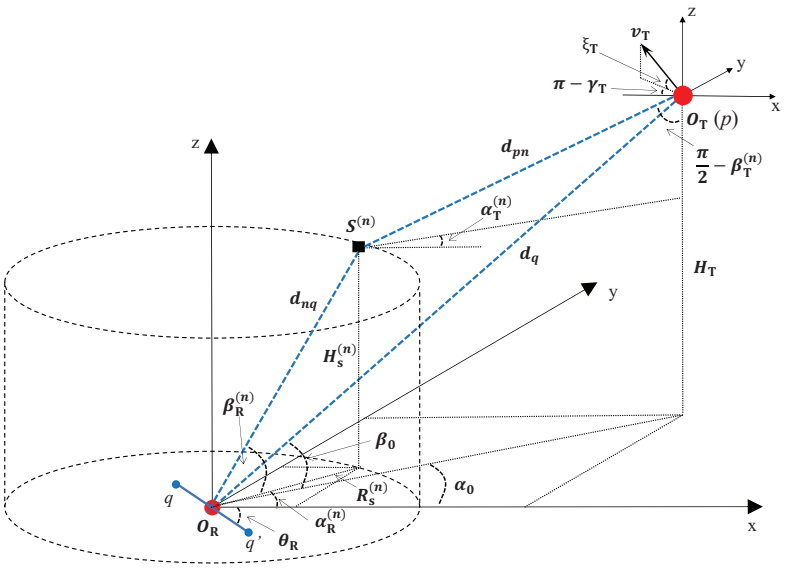

Fig. 3.4 3D GBSM for the A2G channel under UAV wobbling.

wobbling moving direction of the UAV could be expressed by $\gamma_T = \tan^{-1}\left(\frac{v_y}{v_x}\right)$ and $\eta_T = \tan^{-1}\left(\frac{v_z}{\sqrt{v_x^2+v_y^2}}\right)$.

3.4.1 Time-variant Channel Impulse Response

Based on the proposed channel model, the physical properties can be characterized by $1 \times N_R$ matrix $\mathbf{H}(t) = [h_q(t)]$, where $h_q(t)$ represents the CIR from the UAV antenna to the q-th ground node antenna element at time t, where $q \in (1,\ldots,N_R)$. From the above GBSM, the complex CIR is a superposition of the LoS component and SB component scattering from scatterers [50], i.e.,

$$h_q(t) = h_q^{\text{LoS}}(t) + h_q^{\text{SB}}(t), \tag{3.12}$$

where

$$h_q^{\text{LoS}}(t) = \sqrt{\frac{KP_q}{K+1}} e^{\frac{-j2\pi f_c d_q(t)}{c}} e^{j2\pi t f_{D,\text{LoS}}}, \tag{3.13}$$

$$h_q^{\text{SB}}(t) = \lim_{N\to\infty} \sqrt{\frac{P_q}{N(K+1)}} \sum_{n=1}^{N} e^{j\phi_n - \frac{j2\pi f_c (d_{pn}(t)+d_{nq})}{c}} e^{j2\pi t f_{D,n}}, \tag{3.14}$$

f_c is carrier frequency, P_q is the transmitted power of the the $p-q$ link, K is the Ricean factor, and ϕ_n is assumed to be an independent random variable and it is uniformly distributed from

0 to 2π. The Doppler terms in (3.13) and (3.14) can be expressed as

$$f_{D,\mathrm{LoS}} = \frac{v_\mathrm{T}}{\lambda}\cos\left(\alpha_\mathrm{T}^{(\mathrm{LoS})} - \gamma_\mathrm{T}\right)\cos\beta_\mathrm{T}^{(\mathrm{LoS})}\cos\xi_\mathrm{T} + \frac{v_\mathrm{T}}{\lambda}\sin\beta_\mathrm{T}^{(\mathrm{LoS})}\sin\xi_\mathrm{T}, \tag{3.15}$$

and

$$f_{D,\mathrm{n}} = \frac{v_\mathrm{T}}{\lambda}\cos\left(\alpha_\mathrm{T}^{(n)} - \gamma_\mathrm{T}\right)\cos\beta_\mathrm{T}^{(n)}\cos\xi_\mathrm{T} + \frac{v_\mathrm{T}}{\lambda}\sin\beta_\mathrm{T}^{(n)}\sin\xi_\mathrm{T}, \tag{3.16}$$

where λ is the carrier wavelength. From Fig. 3.3, the corresponding propagation distances of the respective waves can be derived as follows:

$$d_q(t) = \sqrt{x_q^2 + y_q^2 + z_q^2}, \tag{3.17}$$

$$d_{pn}(t) = \sqrt{x_{pn}^2 + y_{pn}^2 + z_{pn}^2}, \tag{3.18}$$

$$d_{nq} = \sqrt{x_{nq}^2 + y_{nq}^2 + z_{nq}^2}, \tag{3.19}$$

where $x_q = \Delta_\mathrm{R}\cos\theta_\mathrm{R}$, $y_q = \Delta_\mathrm{R}\sin\theta_\mathrm{R}$, $z_q = H_\mathrm{T}$, $x_{pn} = -R_\mathrm{s}^{(n)}\cos(\alpha^{(n)})$, $y_{pn} = R_\mathrm{s}^{(n)}\sin(\alpha^{(n)})$, $z_pn = H_\mathrm{T} - H_\mathrm{s}^{(n)}$, $x_{nq} = \Delta_\mathrm{R}\cos\theta_\mathrm{R} + R_\mathrm{s}^{(n)}\cos(\alpha^{(n)})$, $y_{nq} = \Delta_\mathrm{R}\sin\theta_\mathrm{R} + R_\mathrm{s}^{(n)}\sin(\alpha^{(n)})$, $z_{nq} = H_\mathrm{s}^{(n)}$, and Δ_R denotes the distance from the q-th antenna at receiver to the centre of transmitter. From the geometrical relationship, we have

$$\Delta_\mathrm{R} = \frac{N_\mathrm{R} - 2q + 1}{2} d_\mathrm{R}. \tag{3.20}$$

The above GBSM assumes that the number of scatterers in infinite. Hence, the parameters $\alpha^{(n)}$, $\beta_\mathrm{T}^{(n)}$ can be characterised with a joint probability density function (PDF). Since the random variables are independent of each other, the joint PDF can be simplified to the product of marginal PDF. Thus, the azimuth angle is described by using the von Mises PDF [104], which is given by

$$f(\alpha) = \frac{e^{k\cos(\alpha-\alpha_\mu)}}{2\pi I_0(k)}, -\pi \le \alpha \le \pi, \tag{3.21}$$

where $I_0(\cdot)$ is the zeroth-order modified Bessel function of the first kind, $\alpha_\mu \in [-\pi, \pi]$ is the mean angle at which the scatterers are distributed in the horizontal direction, and k controls

the spread of scatterers around the mean angle. The elevation angle β_{T} is described by the cosine PDF [104], which can be expressed by

$$f(\beta_{\mathrm{T}}) = \frac{\pi}{4\beta_{\mathrm{m}}} \cos\left(\frac{\pi(\beta_{\mathrm{T}} - \beta_{\mu})}{2\beta_{\mathrm{m}}}\right), |\beta_{\mathrm{T}} - \beta_{\mu}| \leq |\beta_{\mathrm{m}}| \leq \frac{\pi}{2}, \tag{3.22}$$

where β_{μ} and β_{m} denote the central angle and the maximum offset near the central elevation angle, respectively. For simplicity, we assume $\beta_{\mathrm{T1}} = \beta_{\mu} - \beta_{\mathrm{m}}$ and $\beta_{\mathrm{T2}} = \beta_{\mu} + \beta_{\mathrm{m}}$, i.e., $\beta_{\mathrm{T}} \in [\beta_{\mathrm{T1}}, \beta_{\mathrm{T2}}]$.

3.4.2 Time-variant Space-time Correlation Function

Assuming that the LoS and SB components are independent to each other, thus space-time correlation function can be written as follows

$$R_{q,\tilde{q}}(d_{\mathrm{R}}, t, \Delta t) = R^{\mathrm{LoS}}_{q,\tilde{q}}(d_{\mathrm{R}}, t, \Delta t) + R^{\mathrm{SB}}_{q,\tilde{q}}(d_{\mathrm{R}}, t, \Delta t). \tag{3.23}$$

Based on the derived CIR, the normalized space-time correlation function of the LoS component can be written as

$$\begin{aligned} R^{\mathrm{LoS}}_{q,\tilde{q}}(d_{\mathrm{R}}, t, \Delta t) &= \frac{\mathrm{E}\left[h^{\mathrm{LoS}}_{q}(t) h^{\mathrm{LoS}}_{q}(t+\Delta t)^{*}\right]}{\sqrt{P_q P_{\tilde{q}}}} \\ &= \frac{K}{K+1} e^{\frac{-j2\pi f_{\mathrm{C}}(d_q(t) - d_{\tilde{q}}(t))}{c}} e^{j2\pi \Delta t f_{D,\mathrm{LoS}}}. \end{aligned} \tag{3.24}$$

Similarly, the expression of the space-time correlation function of the SB component can be obtained as

$$\begin{aligned} R^{\mathrm{SB}}_{q,\tilde{q}}(d_{\mathrm{R}}, t, \Delta t) &= \frac{\mathrm{E}\left[h^{\mathrm{SB}}_{q}(t) h^{\mathrm{SB}}_{q}(t+\Delta t)^{*}\right]}{\sqrt{P_q P_{\tilde{q}}}} \\ &= \lim_{N\to\infty} \frac{1}{N(K+1)} \sum_{n=1}^{N} \mathbf{E}\left[e^{\frac{j2\pi f_{\mathrm{C}}(d_{pn}(t) + d_{nq})}{\lambda}} e^{-j2\pi t f_{D,\mathrm{n}}} e^{\frac{j2\pi f_{\mathrm{C}}(d_{\tilde{p}n}(t) + d_{n\tilde{q}})}{\lambda}} e^{-j2\pi (t+\Delta t) f_{D,\mathrm{n}}} \right]. \end{aligned} \tag{3.25}$$

More specifically, (3.25) has no closed-form solution, we can apply numerical method to investigate the results of space-time correlation function.

3.5 Numerical Results

In this section, the impacts of the mechanical vibration frequency and the velocity envelope covariance on the temporal ACF and Doppler PSD of millimetre-wave RW UAV channel are investigated.

The simulator computes the UAV wobbling velocity based on (3.1) with ϕ_0, μ, Ω_{v}, σ_{v}, σ_{d}, and Δt and then generates the CIR of the UAV A2G link based on (3.5) at 28 GHz. Finally, the temporal ACF is computed by generated CIRs based on (3.6). These simulation processes require time-consuming repetition of channel generation to estimate the temporal ACF of the UAV A2G link to compare with the analytical results. The parameters used for the temporal ACF simulations are summarized in Table 3.1. Since the mechanical wobbling is less than 10 cm from the UAV producer data sheet [105], the distance variance parameters could be set as the 1 mm, 5 mm, and 10 mm, which is presented in σ_{v} and σ_{d} as the constant 0.001, 0.005, and 0.01, respectively. When $\mu = 10,\ 30$, and 50 at $\Delta t = 0.001$ second, it means the $\mathrm{E}[a(t)a(t+\Delta t)] = 0.99,\ 0.97$, and 0.95, respectively. If the autocorrelation of $a(t)$ and $a(t+\Delta t)$ is low, the temporal ACF will decrease too fast. When $\omega_{\mathrm{v}} = 10\pi,\ 20\pi$, and 30π, it means that mechanical vibration change frequencies are 5 Hz, 10 Hz, and 15 Hz, respectively.

Fig. 3.5 shows the temporal ACF of millimetre-wave UAV A2G link for analytical and simulation model at different σ_{v}. The simulation and analytical results fit well, which ensures the correctness of our derivations. According to Fig. 3.5, when σ_{v} increases, the temporal ACF decreases faster for all cases. In different scenarios cases, the temporal ACF presents different models. For Fig. 3.5 (b), since $\mu = 0$ and $\omega_{\mathrm{v}} \neq 0$, the UAV wobbling movement is influenced by mechanical vibration with a stationary amplitude of the movement velocity. Hence, the temporal ACF changes with mechanical vibration in periodic.

Fig. 3.6 and 3.7 present the impact of ω_{v} on the temporal ACF of millimetre-wave UAV A2G link. According to Fig. 3.6, the temporal ACF has some fluctuations at the value of ω_{v} much bigger than μ. When ω_{v} is 10π and μ is 30, the temporal ACF does not have the fluctuations. However, when ω_{v} is noticeable greater than the value of μ, the temporal ACF has the fluctuations. The fluctuation is defined as the derivation value of the temporal ACF

Table 3.1 Simulation parameters for ACF

μ	ω_{v}	σ_{v} [m/s]	σ_{d} [m]	Figure
0	0	$0.001\sqrt{2}$	$0.001\Delta t$	3.5(a)
0	0	$0.005\sqrt{2}$	$0.005\Delta t$	3.5(a)
0	0	$0.01\sqrt{2}$	$0.01\Delta t$	3.5(a)
0	20π	$0.001\frac{\omega_{\mathrm{v}}}{\sqrt{2}}$	$0.001\sin(\frac{1}{2}\omega_{\mathrm{v}}\Delta t)$	3.5(b)
0	20π	$0.005\frac{\omega_{\mathrm{v}}}{\sqrt{2}}$	$0.005\sin(\frac{1}{2}\omega_{\mathrm{v}}\Delta t)$	3.5(b)
0	20π	$0.01\frac{\omega_{\mathrm{v}}}{\sqrt{2}}$	$0.01\sin(\frac{1}{2}\omega_{\mathrm{v}}\Delta t)$	3.5(b)
30	0	$0.001\sqrt{\mu}$	$0.001\sqrt{\Delta t}$	3.5(c)
30	0	$0.005\sqrt{\mu}$	$0.005\sqrt{\Delta t}$	3.5(c)
30	0	$0.01\sqrt{\mu}$	$0.01\sqrt{\Delta t}$	3.5(c)
30	20π	$0.001\sqrt{\frac{\omega_{\mathrm{v}}^2+\mu^2}{\mu}}$	$0.001\sqrt{\Delta t}$	3.5(d)
30	20π	$0.005\sqrt{\frac{\omega_{\mathrm{v}}^2+\mu^2}{\mu}}$	$0.005\sqrt{\Delta t}$	3.5(d)
30	20π	$0.01\sqrt{\frac{\omega_{\mathrm{v}}^2+\mu^2}{\mu}}$	$0.01\sqrt{\Delta t}$	3.5(d)
0	10π	$0.005\frac{\omega_{\mathrm{v}}}{\sqrt{2}}$	$0.005\sin(\frac{1}{2}\omega_{\mathrm{v}}\Delta t)$	3.6(a)
0	20π	$0.005\frac{\omega_{\mathrm{v}}}{\sqrt{2}}$	$0.005\sin(\frac{1}{2}\omega_{\mathrm{v}}\Delta t)$	3.6(a)
0	30π	$0.005\frac{\omega_{\mathrm{v}}}{\sqrt{2}}$	$0.005\sin(\frac{1}{2}\omega_{\mathrm{v}}\Delta t)$	3.6(a)
30	10π	$0.005\sqrt{\frac{\omega_{\mathrm{v}}^2+\mu^2}{\mu}}$	$0.005\sqrt{\Delta t}$	3.6(b)
30	20π	$0.005\sqrt{\frac{\omega_{\mathrm{v}}^2+\mu^2}{\mu}}$	$0.005\sqrt{\Delta t}$	3.6(b)
30	30π	$0.005\sqrt{\frac{\omega_{\mathrm{v}}^2+\mu^2}{\mu}}$	$0.005\sqrt{\Delta t}$	3.6(b)
10	0	$0.005\sqrt{\mu}$	$0.005\sqrt{\Delta t}$	3.8(a)
30	0	$0.005\sqrt{\mu}$	$0.005\sqrt{\Delta t}$	3.8(a)
50	0	$0.005\sqrt{\mu}$	$0.005\sqrt{\Delta t}$	3.8(a)
10	20π	$0.005\sqrt{\frac{\omega_{\mathrm{v}}^2+\mu^2}{\mu}}$	$0.005\sqrt{\Delta t}$	3.8(b)
30	20π	$0.005\sqrt{\frac{\omega_{\mathrm{v}}^2+\mu^2}{\mu}}$	$0.005\sqrt{\Delta t}$	3.8(b)
50	20π	$0.005\sqrt{\frac{\omega_{\mathrm{v}}^2+\mu^2}{\mu}}$	$0.005\sqrt{\Delta t}$	3.8(b)

increasing first and then decreasing, i.e., $\frac{\partial C(\Delta t)}{\partial \Delta t}$ having a zero point. When the value of ω_v is noticeable greater than μ, the UAV wobbling distance is impacted by the high-frequency UAV mechanical vibration with a high autocorrelation UAV wobbling velocity, which makes the UAV wobbling trajectory partially repeatable. When ω_{v} enhances, according to Fig. 3.7, the temporal ACF changing frequency is increase. Since ω_{v} enhances, it also caused σ_{v} boost, which results in the decrease rate of the temporal ACF rising. Meanwhile, the simulation results are compared with the analytical results to ensure the correctness of our derivations.

Fig. 3.8 illustrates the impact of μ on the temporal ACF of millimetre-wave UAV A2G link. For Fig. 3.8 (a), the temporal ACF decreases faster, when μ increases. In this situation, the UAV wobbling movement does not have mechanical vibration. Therefore, the velocity change may be caused by environmental factors, i.e., wind gusts. For Fig. 3.8 (b), when μ increases with mechanical vibration, the temporal ACF will decrease slower. The reason for this situation is μ has a greater effect of the increase or decrease trend of σ_{d} than ω_{v} at $\mu \neq 0$ and $\omega_{\mathrm{v}} \neq 0$ scenario.

Fig. 3.9 can be used to explain why the decrease rate of the temporal ACF abate when μ rise in Fig. 3.8 (b). According to Fig. 3.9 (a), when μ increases, σ_{v}^2 will decrease firstly and then increase very slow. According to Fig. 3.5, when σ_{v} increases, the decrease rate of temporal ACF will boost. Therefore, the decrease rate of temporal ACF will abate when μ increases at $\mu \neq 0$ and $\omega_{\mathrm{v}} \neq 0$ scenarios. Moreover, in Fig. 3.9 (b), at the same time slot, when μ enhances, the temporal ACF enhance firstly and then keep flat because the value of σ_{v}^2 change little.

Fig. 3.10 shows the impact of σ_{v} on the Doppler PSD. The shape of the Doppler PSD slightly widens along the Doppler frequencies axis. Furthermore, the value of the Doppler PSD will increase, when σ_{v} decreases. Moreover, as σ_{v} increasing, the fluctuation of the Doppler PSD will be widened. σ_{v} characterises the standard deviation of $a(t)$ that is amplitude of mechanical sinusoidal vibration of the UAV. The Doppler frequency is centred at 0, as a sinusoidal vibration has an average value of zero even though its amplitude changes. Nevertheless, the mechanical sinusoidal vibration is severer with a greater σ_{v}, and the Doppler spread becomes stronger even though the centre Doppler frequency is unchanged as

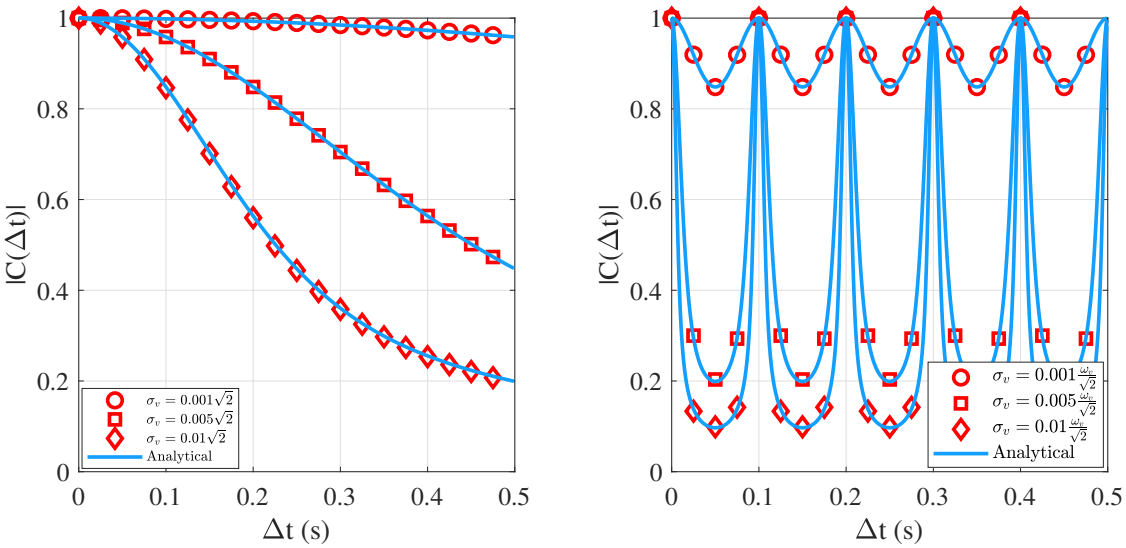

(a) $\mu = 0,\ \omega_v = 0$

(b) $\mu = 0,\ \omega_v = 20\pi$

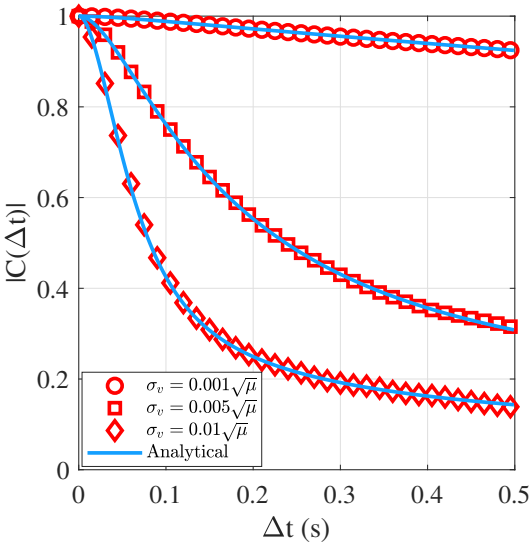

(c) $\mu = 30,\ \omega_v = 0$

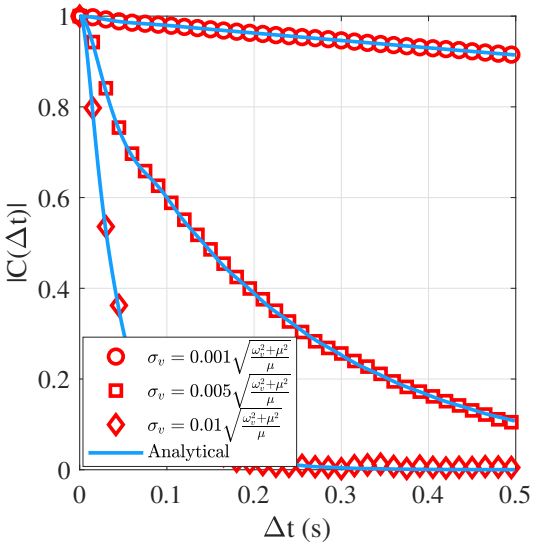

(d) $\mu = 30,\ \omega_v = 20\pi$

Fig. 3.5 The impact of σ_v on temporal ACF. Solid lines illustrate analytical results and makers show simulation results.

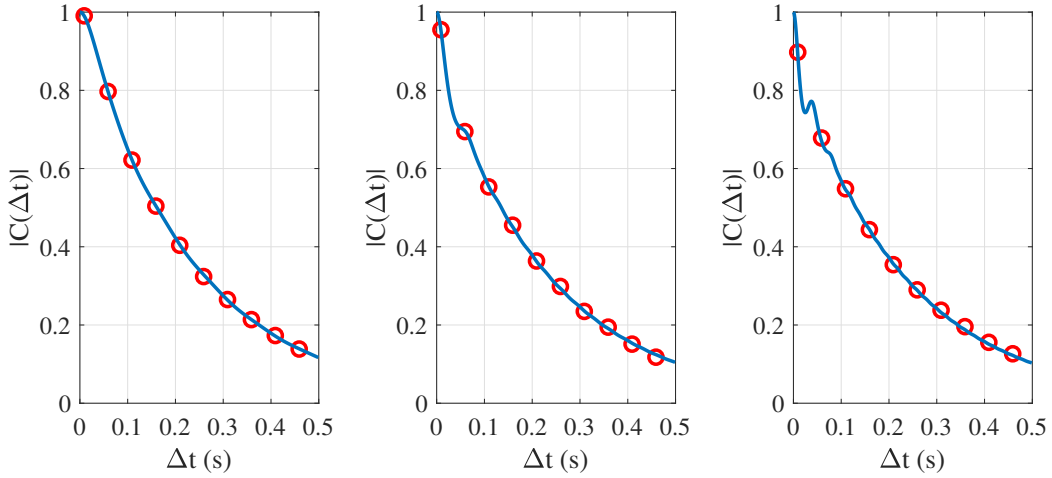

(a) $\omega_{\mathrm{v}} = 10\pi$ (b) $\omega_{\mathrm{v}} = 30\pi$ (c) $\omega_{\mathrm{v}} = 50\pi$

Fig. 3.6 The impact of ω_{v} on the temporal ACF of millimetre-wave UAV A2G link under wobbling at $\mu = 30,\ \sigma_{\mathrm{v}} = 0.005\sqrt{\frac{\omega_{\mathrm{v}}^2+\mu^2}{\mu}}$. Solid lines illustrate analytical results and markers show simulation results.

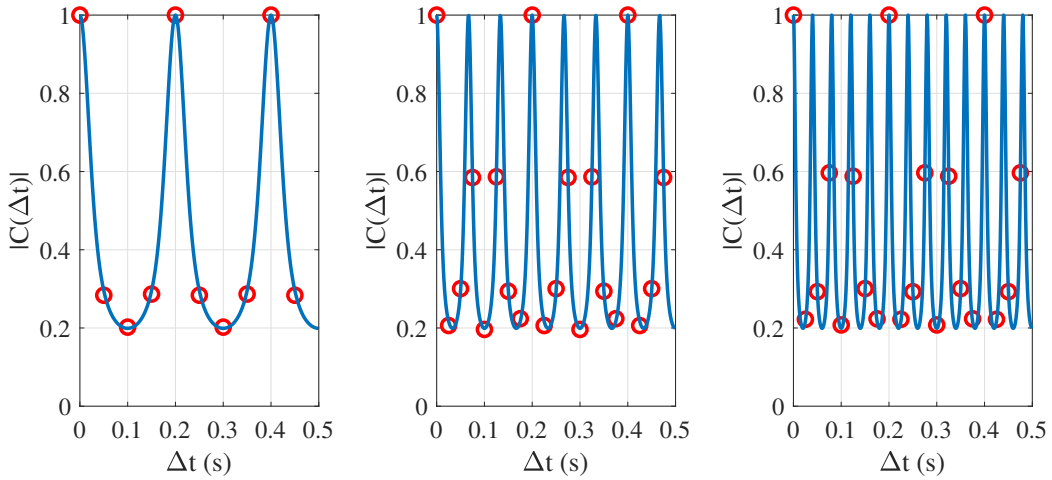

(a) $\omega_{\mathrm{v}} = 10\pi$ (b) $\omega_{\mathrm{v}} = 30\pi$ (c) $\omega_{\mathrm{v}} = 50\pi$

Fig. 3.7 The impact of ω_{v} on the temporal ACF of millimetre-wave UAV A2G link under wobbling at $\mu = 0, \sigma_{\mathrm{v}} = 0.005\frac{\omega_{\mathrm{v}}}{\sqrt{2}}$. Solid lines illustrate analytical results and markers show simulation results.

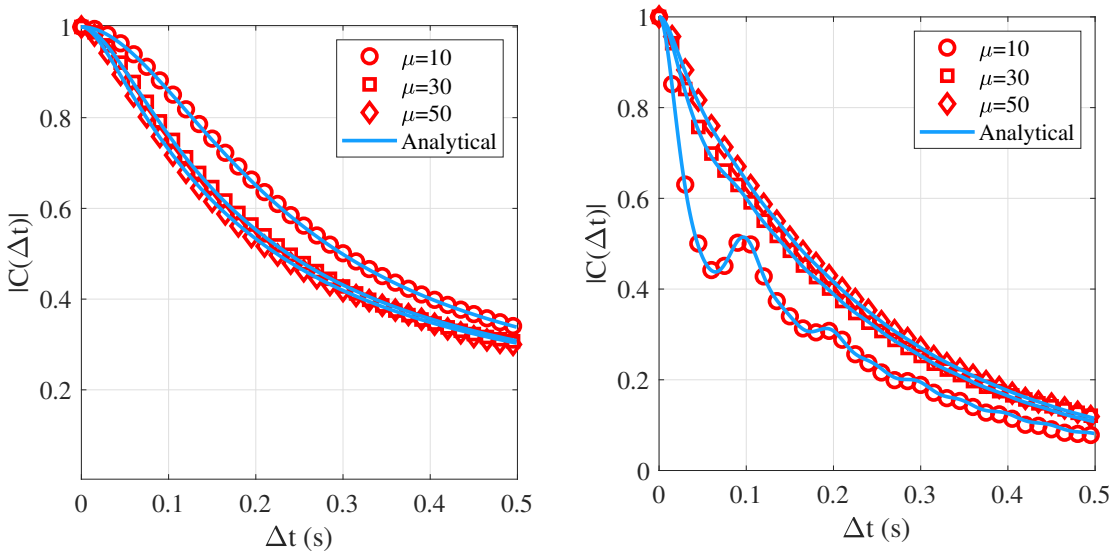

(a) $\omega_{\mathrm{v}} = 0, \sigma_{\mathrm{v}} = 0.005\sqrt{\mu}$ (b) $\omega_{\mathrm{v}} = 20\pi,\ \sigma_{\mathrm{v}} = 0.005\sqrt{\frac{\omega_{\mathrm{v}}^2+\mu^2}{\mu}}$

Fig. 3.8 The impact of μ on the temporal ACF. Solid lines illustrate analytical results and markers show simulation results.

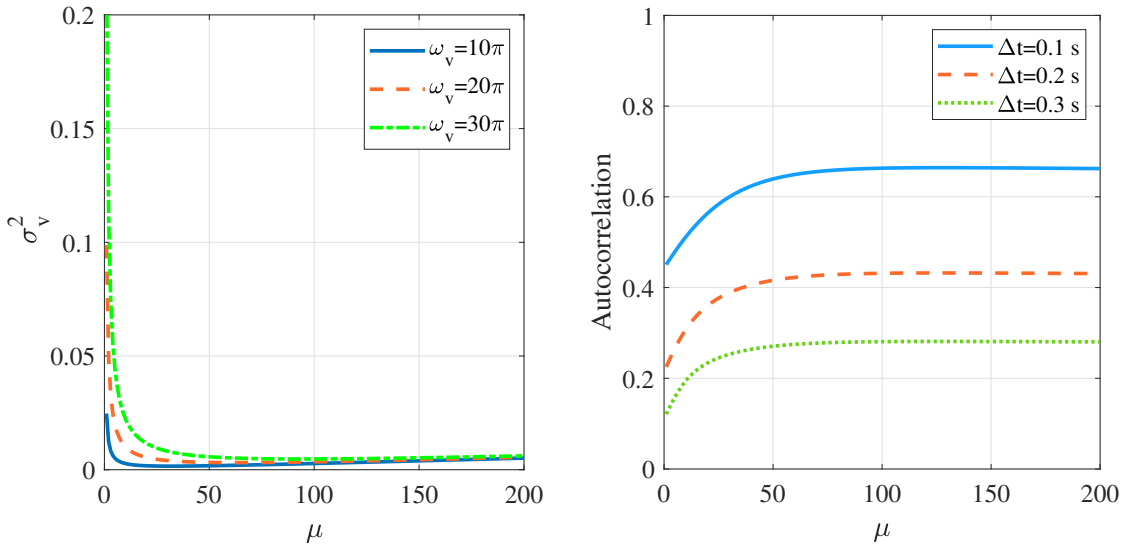

(a) $\sigma_{\mathrm{v}} = 0.005\sqrt{\frac{\omega_{\mathrm{v}}^2+\mu^2}{\mu}}$ (b) $\omega_{\mathrm{v}} = 20\pi,\ \sigma_{\mathrm{v}} = 0.005\sqrt{\frac{\omega_{\mathrm{v}}^2+\mu^2}{\mu}}$

Fig. 3.9 (a) The impact of μ on σ_{d}^2 with different ω_{v}; (b) The impact of μ on the temporal ACF at different time slot.

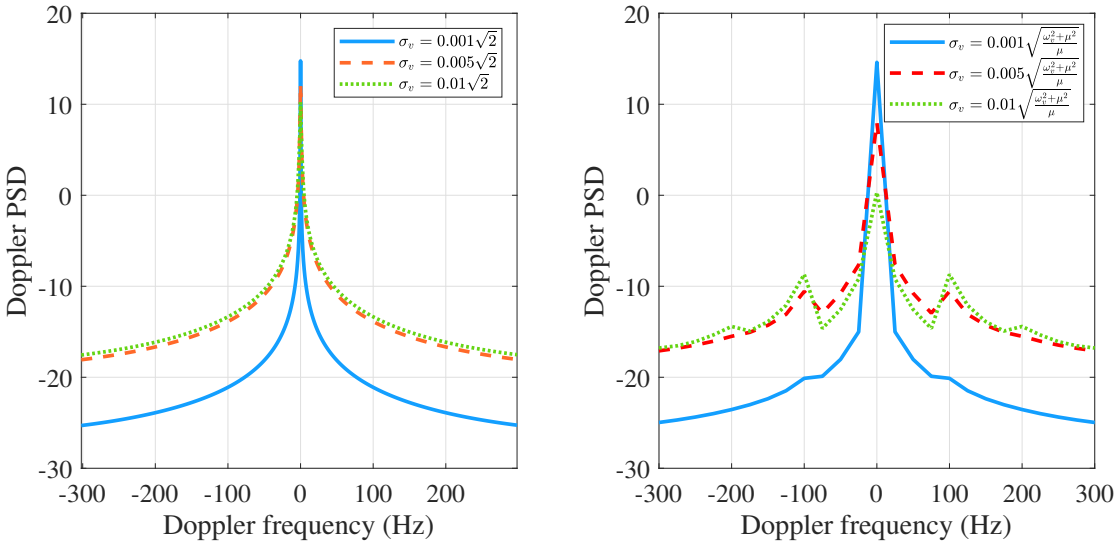

(a) $\omega_v = 0, \mu = 0$ (b) $\omega_v = 200\pi, \mu = 30$

Fig. 3.10 The impact of σ_v on the Doppler PSD with different μ and ω_v.

zero. That is why the Doppler frequency is unchanged while the Doppler PSD spreads more severely with a greater σ_v.

Fig. 3.11 compares the different value of ω_v on the Doppler PSD. When the value of ω_v rises, the fluctuation range of the Doppler PSD broadens. The Doppler frequency of the bulge is rise when the value of ω_v increases. The fluctuation becomes significant as ω_v enhances because the fast mechanical wobbling of UAV.

Fig. 3.12 illustrates the impact of μ on the Doppler PSD. When μ increases, the fluctuation of the Doppler PSD abates. However, μ will not change the Doppler frequency of the bulge. Moreover, the value of μ influences the number of the Doppler PSD bulges. When the value of μ is small and the value of ω_v is large, the UAV wobbles more randomly, which leads to the richer Doppler PSD components in the Doppler domain. Hence, the lower value of μ has more Doppler PSD bulges.

Fig. 3.13 shows the BEP performance of millimetre-wave UAV A2G link employing with M-ary PSK or M-ary QAM signals under mechanical wobbling. μ and ω_v sets as 30 and 20π in this case, respectively. For millimetre-wave UAV A2G link, the channel estimation process finishes at $\Delta t = 0$ and then the signal transmission begins. According to Fig. 3.13,

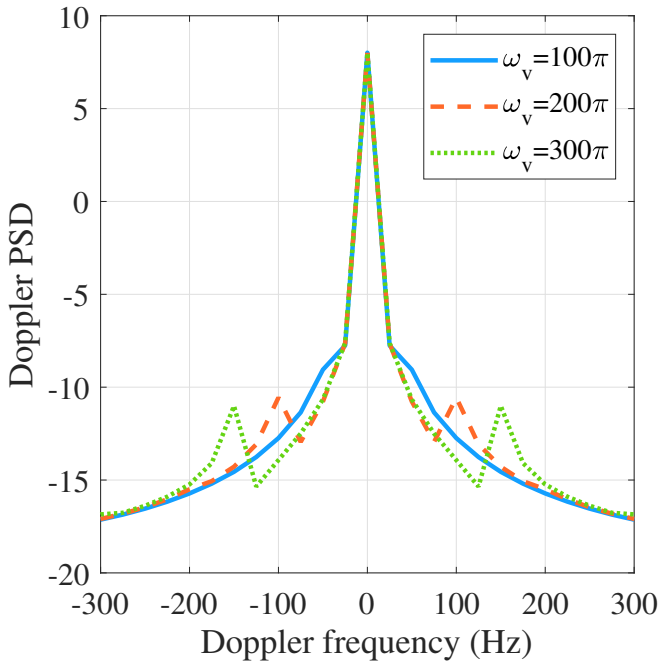

Fig. 3.11 The impact of ω_{v} on the Doppler PSD with $\sigma_{\mathrm{v}} = 0.005\sqrt{\frac{\omega_{\mathrm{v}}^2+\mu^2}{\mu}}$ and $\mu = 30$.

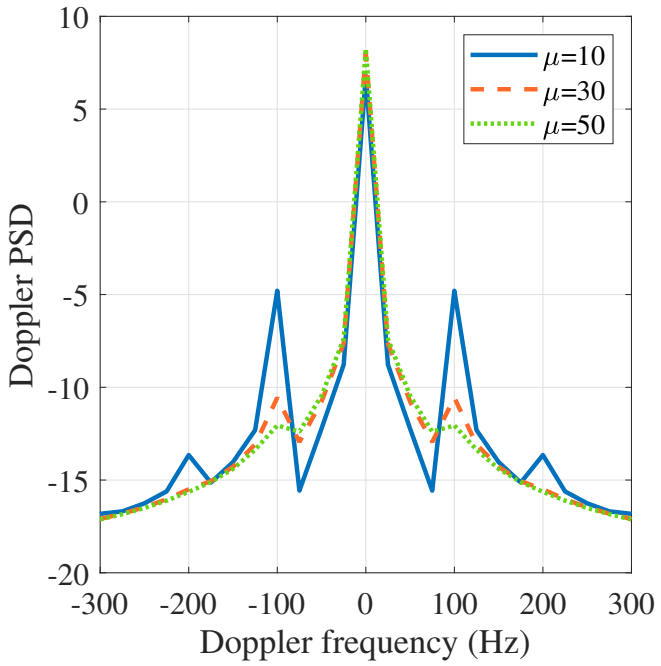

Fig. 3.12 The impact of μ on the Doppler PSD with $\sigma_{\mathrm{v}} = 0.005\sqrt{\frac{\omega_{\mathrm{v}}^2+\mu^2}{\mu}}$ and $\omega_{\mathrm{v}} = 200\pi$.

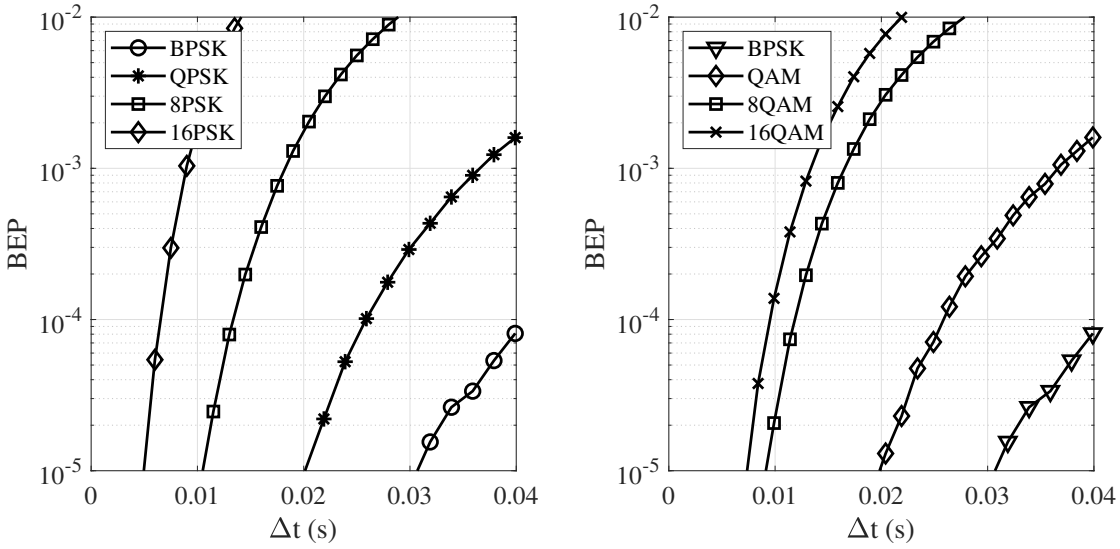

(a) PSK (b) QAM

Fig. 3.13 The BEP performance of millimeter-wave RW UAV A2G link under mechanical wobbling employing with PSK and QAM signals with $\sigma_{\mathrm{v}} = 0.005\sqrt{\frac{\omega_{\mathrm{v}}^2+\mu^2}{\mu}}$.

the BEP performance of the transmission becomes worse in a short transmission period. During the same transmission period, the UAV has weak wobbling because the distance variance parameters sets as 5 mm, which is shown in Fig. 3.5(d). Hence, a key observation is that even for weak UAV wobbling, the BEP of the millimetre-wave RW UAV A2G link deteriorates quickly, which may lead to an unreliable communication link.

The effect of GBSM parameters on the performance of the space-time correlation function is numerically investigated. The parameters are selected as suggested in [104], which are listed here or specified otherwise: f_{c} = 2 GHz, $d_{\mathrm{R}} = 0.5\lambda$, $K = 0.3$, $N_{\mathrm{R}} = 2$, $H_{\mathrm{T}} = 100$ m, $\theta_{\mathrm{R}} = -\frac{\pi}{2}$, $\alpha_{\mu} = \pi$, $R_{\mathrm{S}} = 3$ m, $\omega_{\mathrm{v}} = 30\pi$, $\mu = 30$, $H_{\mathrm{S}} = 5$ m, $k = 3$, $\beta_{\mu} = \beta_{\mathrm{m}} = \frac{\pi}{24}$. In the repeatedly verification, the rays number in each scatterer is chosen as 20 in our simulation model, which ensures both the accuracy and simplification. In the following, the influence of UAV wobbling on the space-time correlation is analysed in detail.

According to Fig. 3.14, when σ_{v} increases, the temporal ACF decreases faster. This observation is same as the previous results because the bigger σ_{v} leads to the larger change of velocity amplitude.

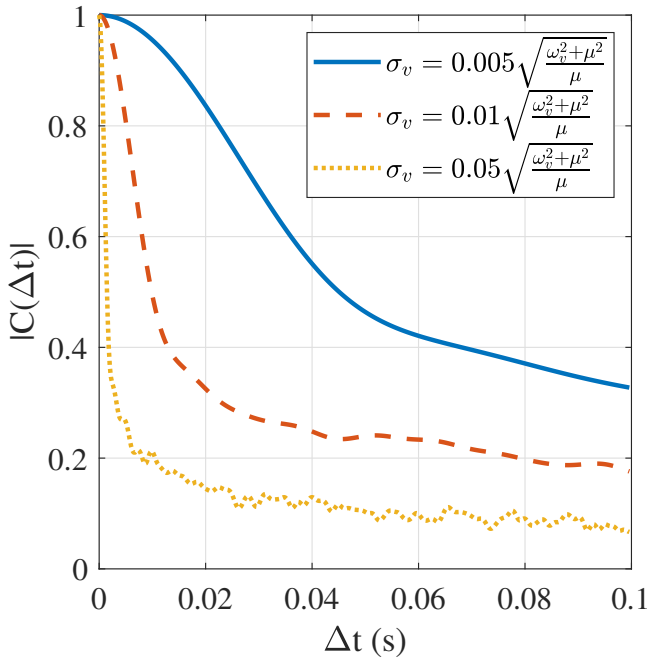

Fig. 3.14 The impact of σ_v on temporal ACF with $\omega_v = 30\pi$ and $\mu = 30$ for 3D GBSM.

Fig. 3.15 presents the absolute value of the space correlation function for UAV wobbling. It can be seen from the figure that the correlation curve decreases with the increase of receiver antenna spacing.

3.6 Conclusions

In this chapter, the analytical model of the Doppler effect brought by the mechanical wobbling in the millimetre-wave RW UAV A2G link is proposed. Applying the RW UAV wobbling movement model at hovering status, the closed-form expression of the temporal ACF has been derived and verified via the Monte-Carlo simulation. Moreover, the Doppler PSD of millimetre-wave RW UAV channel has been computed based on the analytical temporal ACF. Numerical results show that the mechanical vibration frequency and the radial velocity envelope covariance interact on the decrease rate and fluctuation model of the temporal ACF. The Doppler spread range broadens as the mechanical vibration frequency enhances while the value and the number of the Doppler PSD bulge degrade as the radial velocity envelope

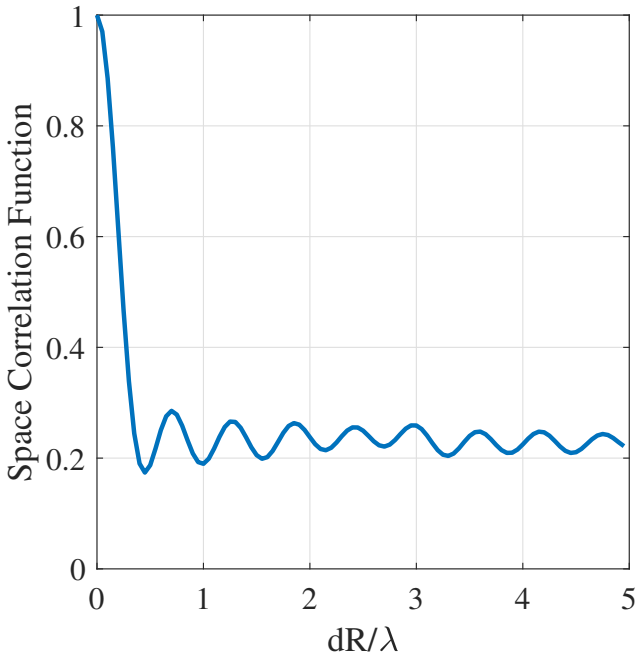

Fig. 3.15 The space correlation function of wobbling UAV with $\sigma_{\mathrm{v}} = 0.01\sqrt{\frac{\omega_{\mathrm{v}}^2+\mu^2}{\mu}}$, $\omega_{\mathrm{v}} = 30\pi$ and $\mu = 30$.

covariance increases. Therefore, the UAV designer has to jointly consider the vibration frequency and the radial velocity envelope covariance carefully to mitigate the impact of the Doppler effect brought by the RW UAV mechanical wobbling on the A2G wireless link.

Chapter 4

Adaptive Modulation of Millimetre-wave UAV A2G Link under Imperfect CSI

Overview

The emerging millimetre-wave UAV A2G communications are facing challenges due to the Doppler effect that arises from the inevitable wobbling of the UAV and fast time-varying channel characteristics that may lead to the outdated CSI from the channel estimation. In this chapter, two detectors to demodulate the received signal are introduced and the instantaneous BEP of a millimetre-wave UAV A2G link under imperfect CSI is computed. Based on designed detectors, an adaptive modulation scheme is proposed, which maximises the average transmission rate under imperfect CSI by optimizing the data transmission time subject to the maximum tolerable BEP. Numerical results show that the proposed adaptive modulation scheme maximises the temporally averaged data rate of the millimetre-wave UAV A2G link under imperfect CSI.

4.1 Introduction

UAV A2G communications have been widely investigated for providing flexible coverage and capacity enhancements, where UAVs carry aerial BSs or mobile relay nodes as part

of 5G cellular systems [3, 12]. UAV A2G links have also been designed to operate in millimetre-wave bands to support high data rates [25].

While hovering in the air, UAVs will be inevitably wobbling due to various environmental and mechanical issues, such as wind gusts, bad weather, and high vibration frequency of their propellers and rotors [21]. Such UAV wobbling leads to the Doppler effect on the millimetre-wave UAV A2G link [25, 26], making the wireless channel unstable and unpredictable [21]. Although the CSI of a UAV A2G link can be estimated with a low mean square error under the Doppler effect by exploiting some known channel characteristics [106, 107], the channel estimation for the time-varying channel has to be updated sufficiently frequently; otherwise the outdated CSI will increase the BEP and reduce the throughput of the UAV A2G link [96].

Adaptive modulation technique has been widely used in mobile communication systems to improve spectral efficiency and throughput by adapting the modulation order to the time-varying channel [108]. In [109], assuming the perfect CSI for an adaptively modulated MIMO system, the multiple modulation order regions were divided by comparing the SNR at the receiver with a predefined switching threshold to maximise the spectral efficiency subject to the BEP and power constraints. In [110], the authors proposed a signal-to-interference-plus-noise-ratio (SINR) estimation algorithm under imperfect CSI and used the estimated instantaneous SINR to decide the modulation order to improve the spectral efficiency. In [111], the authors analysed the impact of imperfect CSI on an adaptively modulated terrestrial communication system by using discrete correlation coefficients between the predicted and the true SNR at the receiver. On the contrary, for a UAV A2G link, a continuous temporal correlation function of the CIR is more suitable to describe the CSI than discrete correlation coefficients because the hovering UAV is not completely stationary causing time-varying Doppler effects on the A2G channel [21, 112]. The trade-off between the channel estimation time and the data transmission time has not been sufficiently studied to maximise the average transmission rate of an adaptive modulation scheme under imperfect CSI.

In this chapter, a novel adaptive modulation scheme to maximise the average transmission rate of a millimetre-wave UAV A2G link while considering imperfect CSI due to the UAV wobbling is proposed. More specifically, the optimum transmission time of the adaptive

modulation scheme that maximises the average transmission rate of the wobbling millimetre-wave UAV A2G link subject to the maximum tolerable BEP and a channel estimation time constraint is derived. The major contributions of this chapter are summarized as follows:

- The imperfect CSI is modelled by a novel continuous temporal ACF of the UAV A2G CIR. The continuous temporal ACF of the CIR is used to obtain the instantaneous BEP, which is used by the adaptive modulation scheme to adjust the modulation order.

- Two detectors are introduced for millimetre-wave UAV A2G links under imperfect CSI, i.e., the maximum likelihood detector and the sub-optimum detector, which both use the continuous temporal ACF as the reference to demodulate the received signal and get the instantaneous BEP. To speed up the calculation of the instantaneous BEP, the sub-optimum detector ignores the power differences among symbols in a constellation diagram, leading to a computational complexity lower than that of the maximum likelihood detector. The closed-form UUB on the BEP for the sub-optimum detector under imperfect CSI is derived and its accuracy is verified by comparing it with the Monte-Carlo simulations.

- The adaptive modulation scheme is proposed based on the designed detectors to maximise the average transmission rate of the millimetre-wave UAV A2G link under imperfect CSI by optimizing the data transmission time and the modulation order (among M-ary PSK or M-ary QAM) subject to a BEP threshold, constant transmission power, and a channel estimation time constraint.

- Numerical results show that the proposed sub-optimum detector with a lower computational complexity achieves a similar demodulation accuracy as that of the maximum likelihood detector. The proposed optimum adaptive modulation scheme is able to achieve the maximum average transmission rate of the millimetre-wave UAV A2G link under imperfect CSI.

The rest of this chapter is organized as follows. In Section II, the system model of a millimetre-wave UAV A2G link with the adaptive modulation under imperfect CSI and two

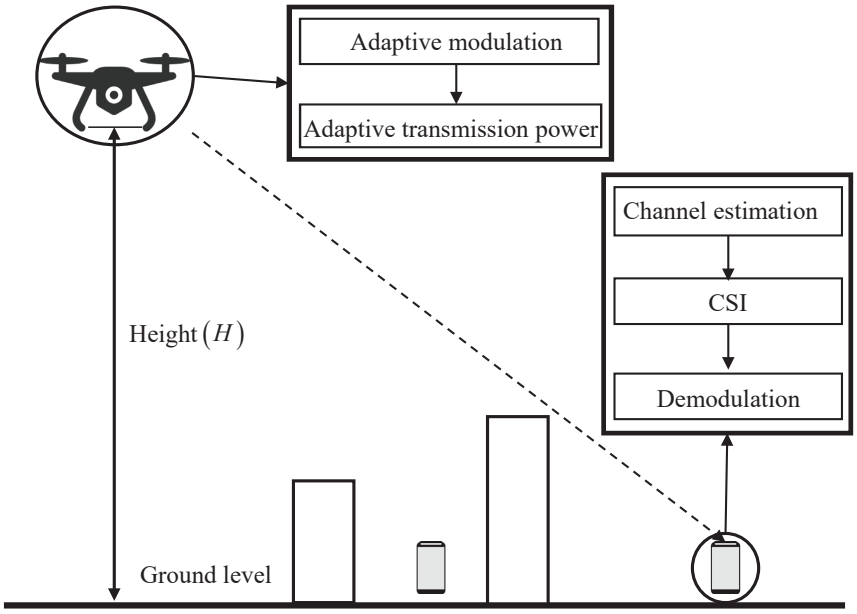

Fig. 4.1 The millimetre-wave UAV A2G link.

designed detectors are presented. In Section III, the maximisation of the average transmission rate is formulated and solved. In Section IV, numerical results are provided to evaluate the performance of the optimum adaptive modulation scheme under imperfect CSI. Finally, in Section V, main conclusions are drawn.

4.2 System Model

A wobbling millimetre-wave UAV A2G link is considered, as illustrated in Fig. 4.1, where the ground node is equipped with N_{R} antennas, while the UAV has a single antenna due to the weight and size constraints [103]. The UAV hovers at a height H above the ground and its horizontal location is $(0,0)$. The horizontal location of the ground node is denoted by $\mathbf{w} \in \mathbb{R}^{2\times 1}$.

Each transmission frame is composed of a fixed channel estimation period T_{e} (seconds) followed by a variable signal transmission period T_{c} (seconds), which is long enough to allow the transmission of at least one symbol. The frame structure schematic diagram is shown in Fig 4.2. In the channel estimation period, the UAV transmits mutually orthogonal

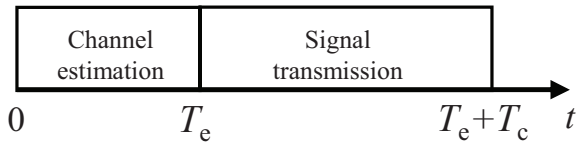

Fig. 4.2 The schematic diagram of the frame structure.

pilot sequences to the N_R receiving antennas at the ground node, where the CSI of the A2G channel is estimated for the current transmission frame. Based on the estimated CSI, the ground node decides the modulation order and the transmission power for A2G transmission and sends the decision to the UAV without any error or delay. This assumption is made for analytical trackability. In the signal transmission period, the UAV will transmit data signal using the modulation order and transmission power level informed by the ground node, and the ground node receiver will use the estimated CSI to demodulate the received signal.

Without loss of generality, we assume that the current transmission frame starts at time t = 0. The average transmission rate in a transmission frame is given by

$$R_{\text{ave}}(T_c) = \frac{1}{T_e + T_c} \int_{T_e}^{T_e+T_c} R(t)\,\mathrm{d}t, \tag{4.1}$$

where $R(t)$ is the transmission rate (bit/symbol) at time t.

4.2.1 Time-varying Channel Impulse Response

At the end of the channel estimation period T_e, the ground node receiver obtains the estimated CIR $\hat{\mathbf{h}}(T_e)$, which is an N_R-by-1 vector and will be used by the ground node detector for signal demodulation during the entire signal transmission period. If the channel estimation at T_e is perfect, then the estimated CIR is equal to the actual CIR, i.e., $\hat{\mathbf{h}}(T_e) = \mathbf{h}(T_e)$. However, due to UAV wobbling, the actual CIR $\mathbf{h}(t)$ in the signal transmission period may become different from $\mathbf{h}(T_e)$ and is given by [31],

$$\mathbf{h}(t) = \mathbf{h}(T_e)\,C(T_e,t) + \mathbf{h}_{\text{rd}}\sqrt{1-|C(T_e,t)|^2}, \tag{4.2}$$

where $C(T_e,t) = \mathrm{E}[\mathbf{h}(T_e)\mathbf{h}^*(t)]$ is the temporal ACF of the millimetre-wave UAV A2G CIR, and $\mathbf{h}_{rd}$ is a N_R-by-1 vector consisting of random elements each following an independent and identical Gaussian distribution $\mathscr{CN}(0,1)$. Hence, the channel estimation $\hat{\mathbf{h}}(T_e)$, even though perfect at T_e, becomes imperfect CSI at t in the signal transmission period.

The received signal at the ground node receiver at time t in the signal transmission period is given by

$$\mathbf{y}(t) = \sqrt{\gamma}\mathbf{h}(t)\,s + \mathbf{n}, \tag{4.3}$$

where $\gamma = \frac{P_T}{P_L N_0}$ is the average SNR [113], P_L is the path loss between the UAV and the ground node UAV transmission power, P_T is the UAV transmission power, N_0 is the power of thermal noise, s is the transmitted symbol, and $\mathbf{n} \sim \mathscr{CN}(0,\mathbf{I}_{N_R})$ is the additive white Gaussian noise (AWGN).

4.2.2 Adaptive Modulation

In this subsection, the different signal transmission processes in transmission frame will be illustrated firstly and then the basic adaptive modulation method is described below.

The schematic diagram of different signal transmission processes is shown in Fig. 4.3. For the conventional transmission process in the time-varying channel, which is shown in Fig. 4.3 (a), the channel estimation only happened at the beginning of the signal transmission in the transmission frame and the channel will not be estimated again until the signal transmission finished. Therefore, the low modulation order, e.g., BPSK and QPSK, will be used to guarantee the demodulation of the signal correctly for most transmission time, which wastes the energy and spectrum [114]. To improve the BEP performance, the time-varying channel will be estimated again before the BEP over the maximum tolerable BEP threshold, which is illustrated in Fig. 4.3 (b). Accordingly, the signal that could be transmitted in one frame by using conventional process will be divided into two transmission frame. The transmission modulation order and the channel estimation interval should also have a trade-off by considering spectral efficiency. The transmission modulation order cannot set as the maximum modulation order at the specific transmission environment [96]. To improve the

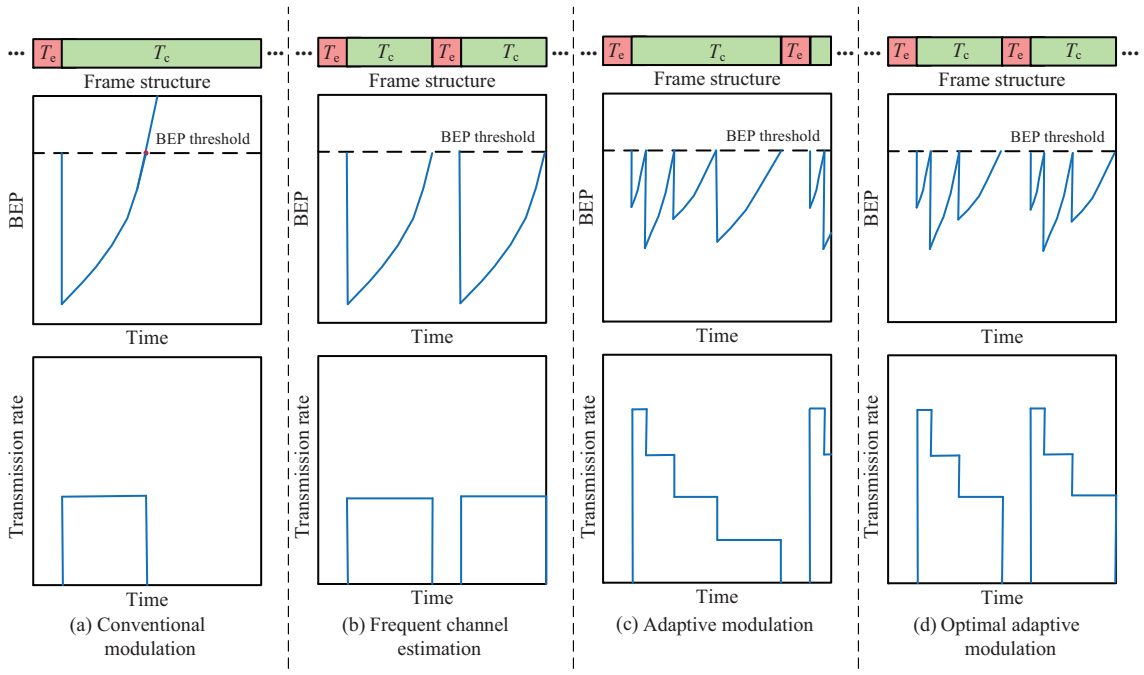

Fig. 4.3 The schematic diagram of the defined problem and the potential solutions.

spectral efficiency further, the adaptive modulation technique is used to extend the signal transmission time and increase the achievable transmission modulation order, which is shown in Fig. 4.3 (c). After the channel estimation, the transmission signal will be followed the adaptive modulation scheme based on instantaneous BEP to adapt the transmission modulation order, where the transmission rate of the signal will decrease step by step until zero. When the transmission rate is 0 or the BEP performance of the link is over the BEP threshold, the wireless channel will be estimated again. The adaptive modulation scheme detail is described below.

An adaptive modulation scheme employing the M-ary PSK or M-ary QAM modulation scheme, $M = \{2,4,8,16,\dots\}$, is considered as the component modulations. The modulation order M is adaptively changed according to how the instantaneous BEP β_i is compared to a BEP threshold β_{th} [115]. Denoting the maximum achievable modulation order that maintains the BEP below the BEP threshold under perfect CSI by $M_{\max}$, then the maximum achievable transmission rate is given by $R_{\max} = \log_2 M_{\max}$.

The adaptive transmission rate at time t in the current transmission frame under imperfect CSI is given by

$$R(t) = \begin{cases} n, & C_n < C(T_e, t) \leq C_{n+1}, \\ 0, & C(T_e, t) \leq C_1, \end{cases} \tag{4.4}$$

where $n \in \{1, \ldots, R_{\max}\}$ is the transmission rate when the value of the temporal ACF $C(T_e, t)$ is between C_n and C_{n+1}, $C_n \in \{C_1, \cdots, C_{R_{\max}}\}$ stands for the minimum required temporal ACF for the instantaneous BEP β_i to be kept below the BEP threshold β_{th} when the transmission rate is n, $C_{R_{\max}+1} = 1$, and the value of C_n can be computed by using the dichotomy method to solve the equation $\text{BEP}[C(T_e, t)] = \beta_{th}$ for $C(T_e, t)$ for 2^n-ary PSK or QAM, where the expression of $\text{BEP}[C(T_e, t)]$ will be given in (4.9) in next subsection. According to Fig 3.5, the temporal ACF $C(T_e, t)$ under UAV wobbling monotonically decreases with t, hence there is a one-to-one match between the temporal ACF C_n and the corresponding transmission time t_n, i.e., $C_n = C(T_e, t_n)$, and $C_{n+1} > C_n$ for $t_{n+1} < t_n$. Thus, the adaptive transmission rate at time t in the current transmission frame under imperfect CSI can be rewritten as

$$R(t) = \begin{cases} n, & t_{n+1} < t \leq t_n, \\ 0, & t_1 \leq t. \end{cases} \tag{4.5}$$

where $t_{R_{\max}+1} = T_e$. When the adaptive modulation scheme adopts the transmission rate of n, the corresponding transmission period is from t_{n+1} to t_n, $n \in \{1, \ldots, R_{\max}\}$.

4.2.3 Maximum Likelihood Detector and Sub-optimum Detector

In this subsection, the maximum likelihood detector and the sub-optimum detector are introduced, which can demodulate the received signal under imperfect CSI to compute the instantaneous BEP. Moreover, the analytical BEP from of the sub-optimum detector is derived.

The maximum likelihood detector under imperfect CSI in [116] was designed for generalized polarization-space modulation. In this work, the spatial domain and polarization state of the detector is neglected for simplicity. Accordingly, the maximum likelihood detector

detects the M-ary PSK or M-ary QAM signals under imperfect CSI, which is provided in Theorem 4.1.

Theorem 4.1. The maximum likelihood detector under imperfect CSI is given by

$$\hat{k} = \underset{k\in\{1,2,\cdots,M\}}{\arg\min} \left\{ \ln \sigma_{\mathrm{e},k}^2 + \frac{\left\| \mathbf{y}(t) - \sqrt{\gamma}\mathbf{h}(T_\mathrm{e}) C(T_\mathrm{e},t)\, s_k \right\|^2}{\sigma_{\mathrm{e},k}^2} \right\}, \tag{4.6}$$

where s_k is the k-th constellation point in the M-ary PSK or M-ary QAM modulation, $k \in \{1,2,...,M\}$,

$$\sigma_{\mathrm{e},k}^2 = \gamma \left(1 - [C(T_\mathrm{e},t)]^2\right) |s_k|^2 + 1, \tag{4.7}$$

and $\sigma_{\mathrm{e},k}^2$ is the effective covariance of the k-th constellation point containing the power differences among symbols in a constellation diagram.

Proof. See Appendix B.1. □

The computational complexity of the maximum likelihood detector is very high because of its searching process and complex computation process. The computational complexity of the detector could be reduced by neglecting the power differences among symbols in a constellation diagram [117]. i.e., $\sigma_{\mathrm{e},k}^2 = 1$. Accordingly, the sub-optimum detector under imperfect CSI is given by

$$\hat{m} = \underset{m\in\{1,2,\cdots,M\}}{\arg\min} \left\{ \left\| \mathbf{y}(t) - \sqrt{\gamma}\mathbf{h}(T_\mathrm{e}) C(T_\mathrm{e},t)\, s_m \right\|^2 \right\}, \tag{4.8}$$

where s_m is the m-th constellation point in the M-ary PSK or M-ary QAM modulation, $m \in \{1,2,...,M\}$.

The UUB technique [116] is employed to derive a tight upper bound on the BEP of the sub-optimum detector for the millimetre-wave UAV A2G link under imperfect CSI, which is provided in Theorem 4.2. Since the sub-optimum detector is used to compute the instantaneous BEP of the millimetre-wave UAV A2G link, the analytical BEP of the sub-optimum detector could be considered as the instantaneous BEP β_i of the millimetre-wave UAV A2G link.

Theorem 4.2. The BEP of the sub-optimum detector for the millimetre-wave UAV A2G link under imperfect CSI is upper bounded by

$$\mathrm{BEP} \leq \sum_{m=1}^{M} \sum_{\hat{m}=1}^{M} \frac{\mathscr{N}_{(m\to\hat{m})} \mathrm{P}_{(m\to\hat{m})}}{M \log_2(M)} \equiv \mathrm{UUB}, \tag{4.9}$$

where we define UUB, $\mathscr{N}_{(m\to\hat{m})}$ is the Hamming distance between symbols s_m and $s_{\hat{m}}$, $s_{\hat{m}}$ is the modulation symbol determined by the sub-optimum detector, $\mathrm{P}_{(m\to\hat{m})}$ is the pairwise error probability (PEP), and is given by

$$\mathrm{P}_{(m\to\hat{m})} = Q\left(\sqrt{\frac{\left\|\sqrt{\gamma}\mathbf{h}(T_\mathrm{e})C(T_\mathrm{e},t)\right\|^2 |s_m - s_{\hat{m}}|^2}{2\gamma\left(1 - C(T_\mathrm{e},t)^2\right)|s_m|^2 + 2}}\right). \tag{4.10}$$

Proof. See Appendix B.2. □

The performance of the maximum likelihood detector and the sub-optimum detector comparison with M-ary PSK or M-ary QAM signals are shown in Fig. 4.4. The simulator of the maximum likelihood detector and the sub-optimum detector is based on (4.6) and (4.8), respectively. Simulation processes require time-consuming repetition of transmission signal generation to estimate the BEP of the UAV A2G link to compare with the analytical result. The analytical results are computed by (4.9) for $N_\mathrm{R} = 8$. The table of $\mathbf{h}(T_\mathrm{e})$ value is shown in the Appendix B.3, where case 1 is used. The following observations are made therein.

- The BEP of the sub-optimum detector is tight with that of the maximum likelihood detector at all SNR regimes. Especially, when the M-ary PSK modulation scheme is used, the performance of the maximum likelihood detector and the sub-optimum detector is the same because the modulus value of the M-ary PSK signal is 1.

- Under perfect or imperfect CSI, the analytical upper bound on the BEP of the sub-optimum detector is tight with simulation in the high SNR regime. Therefore, (4.9) can be used to compute the instantaneous BEP β_i of the adaptive modulation algorithm for the millimetre-wave UAV A2G link in the high SNR regime.

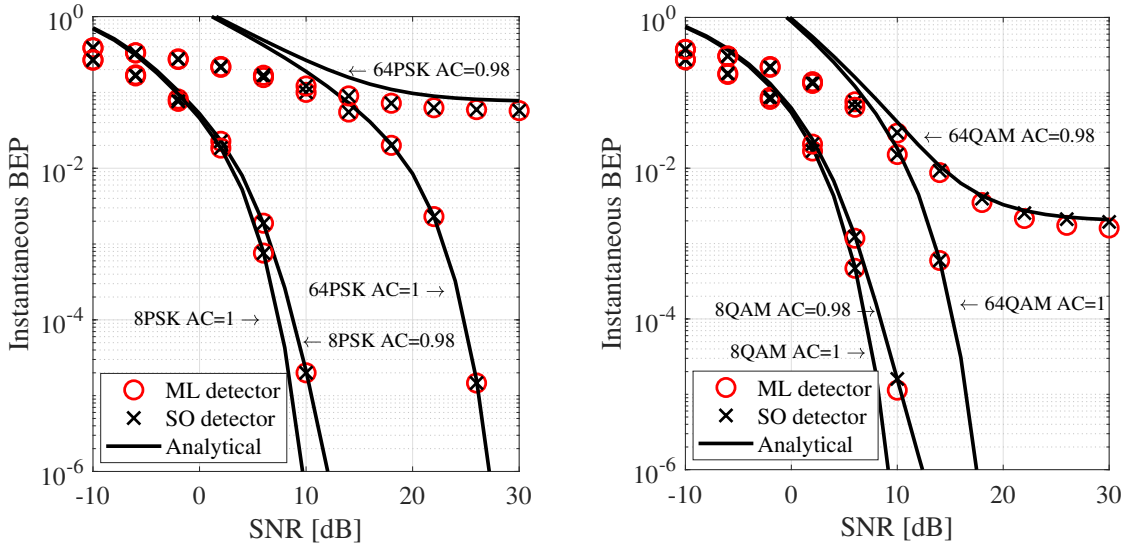

(a) PSK (b) QAM

Fig. 4.4 The performance comparison of maximum likelihood and sub-optimum detector for PSK or QAM scheme. Markers show simulation results and solid lines illustrate analytical results. ML and SO denote maximum likelihood and sub-optimum, respectively. AC denotes the value of temporal autocorrelation.

- The M-ary QAM modulation scheme has better BEP performance than that of the M-ary PSK modulation scheme in the maximum likelihood detector and the sub-optimum detector under perfect or imperfect CSI.
- The BEP will be significantly degraded by the imperfect CSI, which has the significant influence on BEP at the high modulation order.

4.3 Optimum Transmission Time for Adaptive Modulation

4.3.1 Problem Formulation

In the 5G and beyond communications, UAVs usually need to transmit mission-related information for different tasks, such as sensor data and high-resolution images, to ground terminals, where the high transmission rate is one of the most vital requirements for the UAV A2G link [118]. Thus, the high data rate as the first priority requirement to achieve in

the system is considered. However, if the transmission process with just a simple adaptive modulation scheme, which is illustrated in Fig. 4.3 (c), the average transmission rate in transmission frame will become low with a long channel estimation interval according to (4.1). Hence, the method to find the optimum transmission time of the system to achieve the maximum average transmission rate should be discussed.

We formulate the following optimization problem to maximize the average transmission rate of the millimetre wave UAV A2G link under UAV wobbling by optimizing the transmission time T_{c} subject to the BEP threshold and a constant transmission power, i.e.,

$$(\mathrm{P1}): \quad \max_{T_{\mathrm{c}}} \quad R_{\mathrm{ave}}(T_{\mathrm{c}}), \tag{4.11}$$

$$\text{s.t.} \quad \beta_i \leq \beta_{\mathrm{th}}, \tag{4.11a}$$

$$0 \leq T_{\mathrm{c}}, \tag{4.11b}$$

$$P_{\mathrm{T}} = P_{\max}, \tag{4.11c}$$

where (4.11a) requires that the instantaneous BEP β_i computed by (4.9) must be kept below the predetermined BEP threshold β_{th}; (4.11b) is the non-negative constraint on the transmission time; and (4.11c) requires that the transmission power is set at the maximum transmission power, which can support the maximum modulation order of the adaptive modulation under imperfect CSI. Fig. 4.3 (c) and (d) shows a schematic diagram of the optimization of T_{c}.

4.3.2 Problem Solution: Optimum Adaptive Modulation Scheme

In this subsection, the algorithm to find the optimum transmission time as a solution for the problem is described in detail below.

According to (4.1) and (4.5), the average transmission rate for $T_{\mathrm{c}} = t - T_{\mathrm{e}}$ and the corresponding transmission time t_n, $n \in \{1, \ldots, R_{\max}\}$ can be written as

$$R_{\mathrm{ave}}(T_{\mathrm{c}}) = \begin{cases} \frac{t_{R_{\max}} + t_{R_{\max}-1} + \cdots + t_{n+1} - R_{\max} T_{\mathrm{e}}}{T_{\mathrm{c}} + T_{\mathrm{e}}} + R(t), & t_{n+1} < t \leq t_n, \\ \frac{t_{R_{\max}} + \cdots + t_1 - R_{\max} T_{\mathrm{e}}}{T_{\mathrm{c}} + T_{\mathrm{e}}}, & t_1 \leq t. \end{cases} \tag{4.12}$$

Algorithm 1: The optimum transmission time finder.

Input: T_{e}, t_n, $R(t)$, t.
Output: $R_{\mathrm{ave,max}}$, T_{max}.
$R' \leftarrow$ (4.13) with t and T_{e};
if $R' == 0$ **then**
  $T_{\mathrm{max}} \leftarrow T_{\mathrm{c}}$;
else
  $T_{\mathrm{max}} \leftarrow \max(\mathrm{find}(R' < 0))$;
end
$R_{\mathrm{ave,max}} \leftarrow$ (4.12) with $R(t)$, T_{max} and T_{e};

We take the derivation of (4.12) with respect to T_{c} and obtain

$$\frac{\mathrm{d}R_{\mathrm{ave}}(T_{\mathrm{c}})}{\mathrm{d}T_{\mathrm{c}}} = \begin{cases} \frac{R_{\max}T_{\mathrm{e}} - t_{R_{\max}} - \cdots - t_{n+1}}{(T_{\mathrm{c}}+T_{\mathrm{e}})^2}, & t_{n+1} < t \leq t_n, \\ -\frac{t_{R_{\max}} + \cdots + t_1 - R_{\max}T_{\mathrm{e}}}{(T_{\mathrm{c}}+T_{\mathrm{e}})^2}, & t_1 \leq t. \end{cases} \tag{4.13}$$

The signal transmission time to maximize average transmission rate T_{max} can be computed by the basic derivative property based on (4.13). If the derivation of R_{ave} does not have a zero point, the first negative value of derivation will be detected as T_{max}. When T_{max} is founded, the value of maximum average transmission rate $R_{\mathrm{ave,max}}$ can be computed by (4.5) and (4.12), respectively. The pseudo-code of the proposed optimum adaptive modulation scheme is given in Algorithm 1, where R' is a local variable. The flow chart of the optimum adaptive modulation scheme of the mm-wave UAV A2G link under imperfect CSI is shown in Fig. 4.5.

The system complexity is indeed increased by adopting the proposed adaptive modulation. In comparison with the conventional modulation systems with a constant rate, the following perspectives need to be considered in the design of the proposed adaptive modulation system. Firstly, extra computing resources are required at the receiver to compute the temporal ACF and data rate. The temporal ACF has to be known at the receiver via UAV mechanical modelling, A2G channel sounding, or ACF estimation. The data rate could be achieved by following the proposed adaptive modulation scheme. The computation is on the basis of tractable analytic results, and thus requires little computation resource. In this thesis, I assume that the ground node has sufficient computing resources to execute the computation

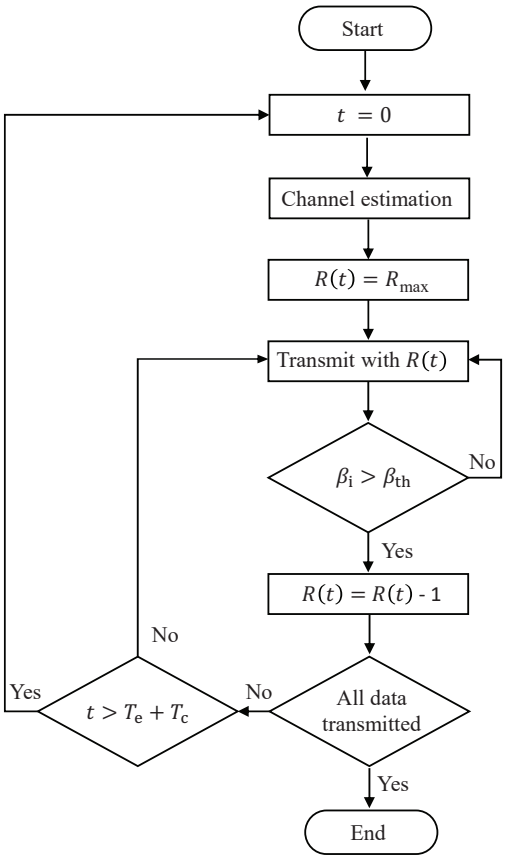

Fig. 4.5 Flow chart of the optimum adaptive modulation scheme under imperfect CSI with time increase.

Furthermore, a feedback link is required between the UAV and the ground node. More specifically, an extra control message is required from the ground node to inform the UAV of the initial transmission rate $R_{\max}$ (one integral number) and the corresponding switching transmission time t_n (multiple floating numbers) required for adaptive modulation. This assumption is widely adopted in published adaptive modulation systems.

4.4 Numerical Results

In this section, the performance of the optimum adaptive modulation scheme of a millimetre-wave UAV A2G link under imperfect CSI is evaluated. How the SNR, BEP threshold, and the UAV wobbling impact the maximum transmission rate will be analysed below.

Table 4.1 Simulation parameters

$\gamma_{\max}$	25 dB
f	28 GHz
ω_{v}	20π rad/sec
μ	30
β_{th}	10^{-5}
N_{R}	8
T_{e}	10^{-3} s

We perform the simulations based on the temporal ACF of the mm-wave UAV A2G link, which is given by (4.14) [112],

$$C(\Delta t) = e^{-0.5\sigma_{\mathrm{v}}^2\left(\frac{\omega_{\mathrm{c}}}{c\left(\omega_{\mathrm{v}}^2+\mu^2\right)}\right)^2\left(\mu\Delta t\left(\omega_{\mathrm{v}}^2+\mu^2\right)-2\mu\omega_{\mathrm{v}}\sin(\omega_{\mathrm{v}}\Delta t)e^{-\mu\Delta t}+\left(\mu^2-\omega_{\mathrm{v}}^2\right)\cos(\omega_{\mathrm{v}}\Delta t)e^{-\mu\Delta t}-\mu^2+\omega_{\mathrm{v}}^2\right)}$$
$$\times J_0\left(j0.5\sigma_{\mathrm{v}}^2\left(\frac{\omega_{\mathrm{c}}}{c}\right)^2\frac{\mu\sin(\omega_{\mathrm{v}}\Delta t)-\omega_{\mathrm{v}}\cos(\omega_{\mathrm{v}}\Delta t)+\omega_{\mathrm{v}}e^{-\mu\Delta t}}{\left(\omega_{\mathrm{v}}^2+\mu^2\right)\omega_{\mathrm{v}}}\right). \tag{4.14}$$

where $\Delta t = t - T_{\mathrm{e}}$, $J_0(\cdot)$ denotes the Bessel function of the first kind with an order zero, σ_{v}^2 is the variance of the UAV movement velocity, ω_{c} is the carrier frequency, ω_{v} is mechanical vibration frequency of the UAV, μ is the parameter to measure how fast the envelope of velocity changes with time. The general system parameters used for temporal ACF and system model simulation to obtain the results are shown in Table 4.1. Especially, $\sigma_{\mathrm{v}}^2 = (0.005)^2\frac{\omega_v^2+\mu^2}{\mu}$ is used in this work. Moreover, the guideline for this work to decide the BEP threshold is based on [119] and [115], where introduced that maximum BEP of the speech, video, and data signals are known as 10^{-3}, 10^{-5}, and 10^{-6}, respectively.

According to Fig. 4.6 and 4.7, the simulation and analytic UUB of the mm-wave UAV A2G link with the adaptive modulation scheme under imperfect CSI are matched well. The simulation result is obtained by computing (4.8) and the analytic UUB is computed based on (4.9) with same estimated CIR. The adaptive modulation (solid line) is obtained following (4.5). The adaptive modulation scheme decreases the modulation order step by step to keep the instantaneous BEP of the system lower than the BEP threshold for M-ary PSK or M-ary QAM signals. M-ary QAM signals have higher modulation order than that of M-ary PSK signals because the Euclidean distance of the M-ary QAM signals are greater than or equal

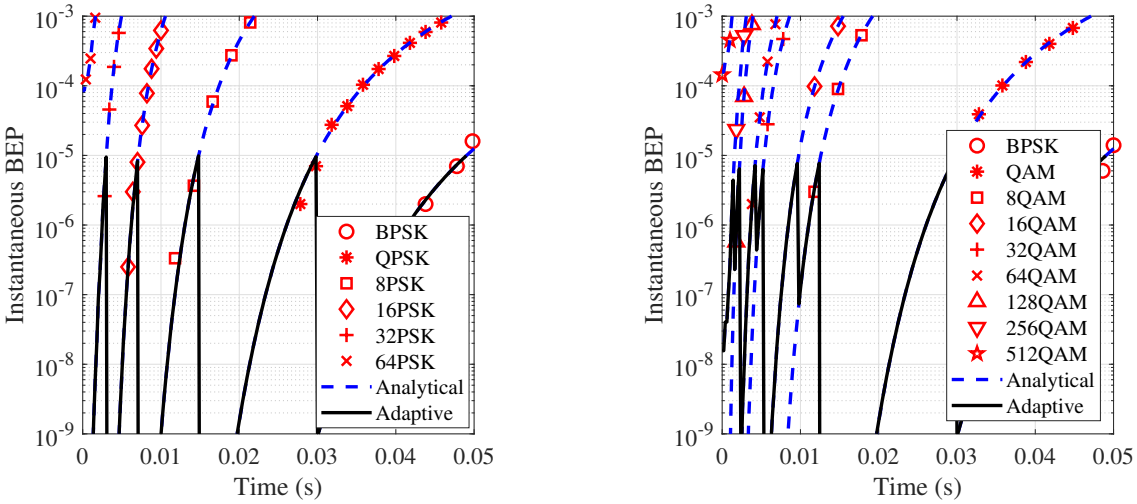

(a) PSK (b) QAM

Fig. 4.6 Adaptive modulation scheme employing M-ary PSK or M-ary QAM under case 1. Markers show simulation results, dash lines illustrate analytical results, and solid lines is the adaptive modulation..

to that of the M-ary PSK signals. These two figures shows the proposed detector and the adaptive modulation algorithm wok well.

The instantaneous and average transmission rates with the adaptive modulation scheme under different estimated CIRs for M-ary PSK and M-ary QAM scheme are shown in Fig. 4.8. The instantaneous transmission rate shows how the adaptive modulation scheme works based on the transmission policy, which is also a supplement of the Fig. 4.6 and 4.7. The instantaneous transmission rate of M-ary QAM scheme is more sensitive to $\mathbf{h}(T_e)$ than that of M-ary PSK scheme. The average transmission rate computed by (4.1) increases first and then decreases as transmission time increases, where the maximum average transmission rate is shown.

Fig. 4.9 (a) and (b) show the maximum average transmission rate $R_{\text{ave,max}}$ at different value of BEP threshold and SNR employing M-ary PSK or M-ary QAM signals based on the optimum adaptive modulation. As Fig. 4.3 (d), the optimum adaptive modulation scheme will estimated the channel again when the maximum average transmission rate is achieved. Hence, the performance evaluation of optimum adaptive modulation require time-consuming repetition of the channel situation generation. $R_{\text{ave,max}}$ increases with an increasing SNR at

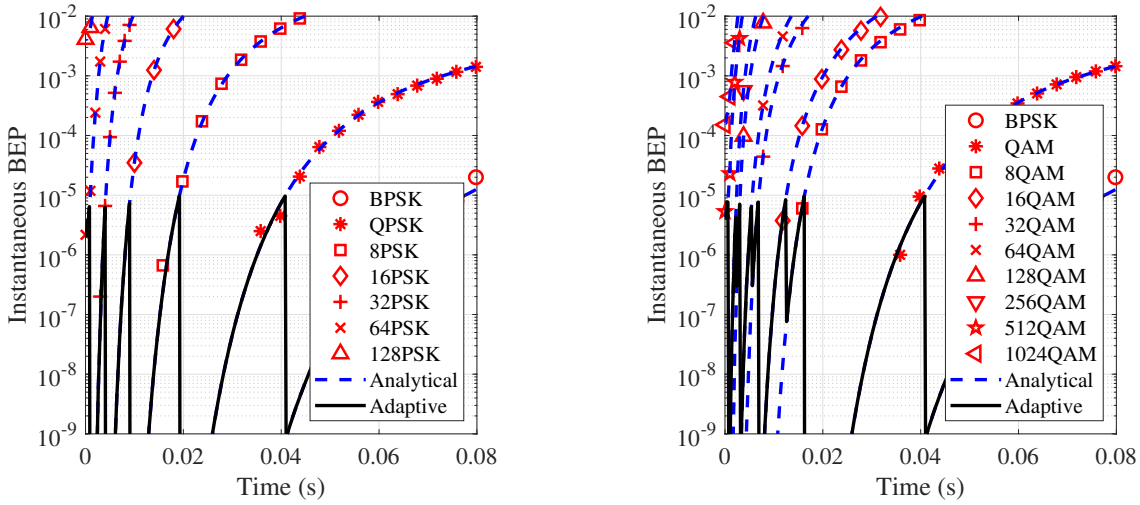

(a) PSK (b) QAM

Fig. 4.7 Adaptive modulation scheme employing M-ary PSK or M-ary QAM under case 2. Markers show simulation results, dash lines illustrate analytical results, and solid lines is the adaptive modulation.

the same BEP threshold. In contrast, $R_{\text{ave,max}}$ decreases with the BEP threshold decrease at the same SNR. Since the maximum achievable transmission rate of M-ary QAM is higher than that of M-ary PSK, M-ary QAM have a higher $R_{\text{ave,max}}$ than that of M-ary PSK at the same BEP threshold and SNR.

4.5 Conclusions

In this chapter, the novel adaptive modulation scheme of the millimetre-wave UAV A2G link under imperfect CSI to maximise the average transmission rate have proposed. The channel estimation time and transmission time will have an optimized trade-off based on the algorithm to achieve the maximum average transmission rate subjects to the maximum tolerable BEP threshold. Moreover, how the operating environment influences the average transmission rate is also discussed. These can give a guideline for engineers to design the millimetre-wave UAV A2G link for maintaining the BEP performance under the maximum tolerable BEP threshold while maximizing the average transmission rate.

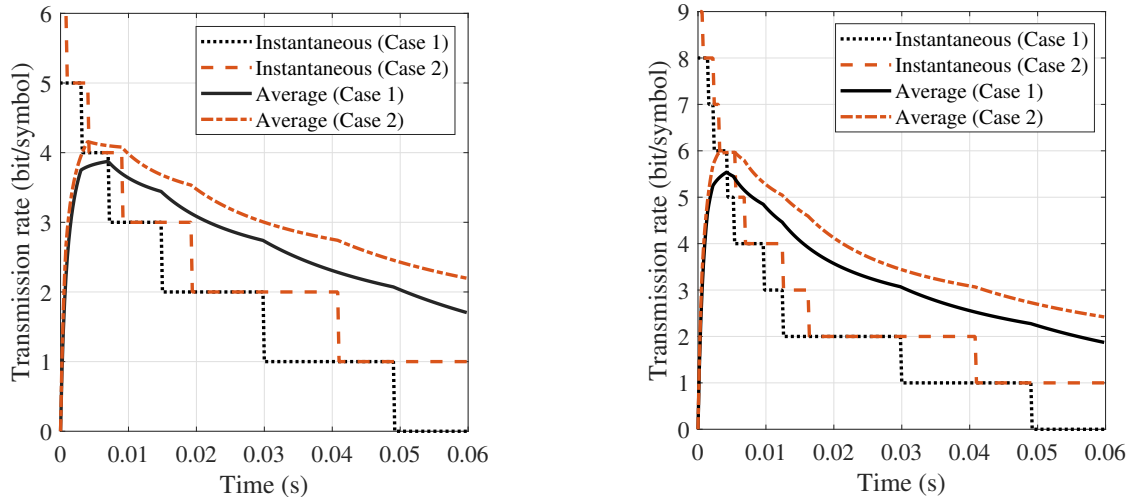

(a) PSK (b) QAM

Fig. 4.8 The instantaneous and average transmission rate for two cases of $\mathbf{h}(T_e)$ with adaptive modulation scheme at BEP threshold 10^{-5}.

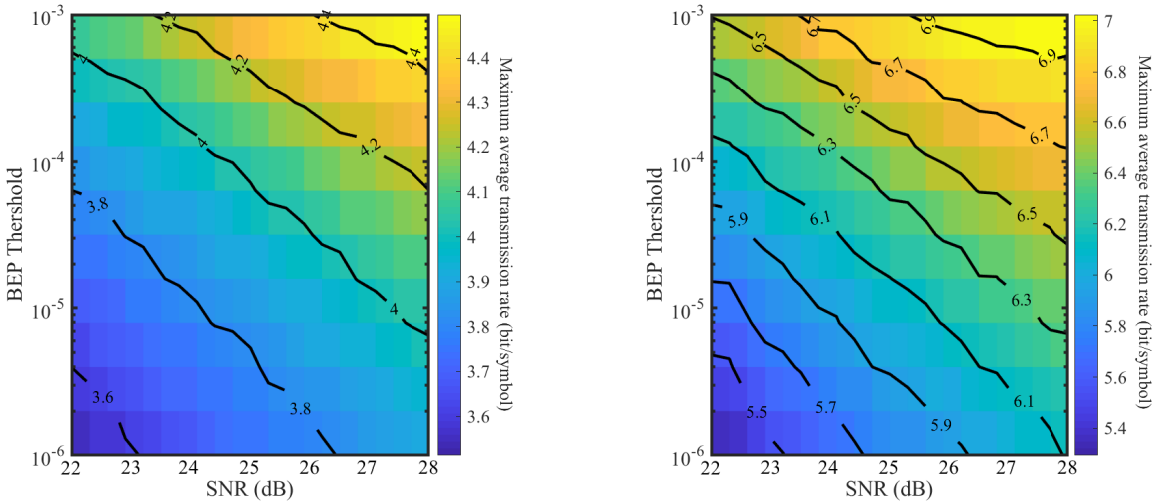

(a) PSK (b) QAM

Fig. 4.9 Comparison of maximum average data rates for the designed adaptive modulation scheme employing M-ary PSK or M-ary QAM under different SNR and BEP thresholds.

Chapter 5

Power Control Policy of Millimetre-wave UAV A2G Link

Overview

The emerging millimetre-wave UAV A2G communications are facing challenges due to the size, weight, and battery capacity restrictions of UAVs. The UAV operating time has become a bottleneck of using UAV A2G networks. In this chapter, a power control policy that minimises the transmission power while maintaining both the instantaneous BEP under the BEP threshold and the maximised average transmission rate is introduced. Numerical results show that the power control policy minimises the transmission power consumption of the millimetre-wave UAV A2G link under imperfect CSI. The EE performance of the millimetre-wave UAV A2G link with power control policy is evaluated.

5.1 Introduction

UAV A2G communications have been widely investigated for providing flexible coverage and capacity enhancements, where UAVs carry aerial BSs or mobile relay nodes as part of 5G cellular systems [3, 12]. However, under the size, weight, and battery capacity restrictions of UAVs, the UAV operating time has become a bottleneck for the UAV-carried aerial BSs or mobile relay nodes [19].

Although adaptive modulation schemes, which is described in chapter 4, can be used to improve the spectral efficiency of an A2G link, they also need to be supported by a power control policy to maintain the EE because using constant transmission power while reducing the modulation order will waste the energy of the UAV [120]. In [24], the authors proposed power allocation mechanisms for fixed BSs and steady UAVs to maximise the system sum rate or minimise the system power consumption of a UAV-assisted millimetre-wave heterogeneous cellular network. In [94], the authors maximised the average achievable rate of a steady UAV A2G link, which shared the spectrum with terrestrial wireless communication links, by optimizing the UAV's 3D trajectory and transmission power. The combination of the adaptive modulation and the power control for wobbling millimetre-wave UAV A2G links to maintain the maximum achievable transmission rate has not been studied in the published literature.

In this chapter, a novel power control policy to minimise the instantaneous transmission power of a millimetre-wave UAV A2G link while considering imperfect CSI due to the UAV wobbling is proposed. The power control policy minimises the instantaneous transmission power for the adaptive modulation scheme, while maintaining the maximised average transmission rate subject to the BEP threshold. The major contributions of this chapter are summarized as follows:

- A new power control policy is designed to minimize the instantaneous transmission power of the adaptive modulation subject to the BEP threshold at the receiver and the maximum transmission power constraint, while maintaining the maximum average transmission rate. The BEP approximation based on the signal-space concept and the Netwon-Raphson method is used to compute the minimized instantaneous transmission power for M-ary PSK and M-ary QAM, respectively.

- The EE performance of the millimetre-wave UAV A2G link with the power control policy is evaluated under the constant transmission rate or the adaptive modulation scheme. The trade-off between the transmission time and the estimation time is analysed to find the maximum EE of the system.

- Numerical results show that the power control policy is able to achieve the maximum average transmission rate of the millimetre-wave UAV A2G link under imperfect CSI, while keeping the minimum transmission power consumption of the UAV subject to the BEP threshold.

The rest of this chapter is organized as follows. In Section II, the system model of a millimetre-wave UAV A2G link under imperfect CSI are presented and the minimisation of the average transmission power is formulated. In Section III, the power control policy is designed. In Section IV, the EE performance of the millimetre-wave UAV A2G link under imperfect CSI is evaluated. In Section V, numerical results are provided to evaluate the performance of the power control policy under imperfect CSI. Finally, in Section VI, main conclusions are drawn.

5.2 System Model and Problem Formulation

5.2.1 System Model

A wobbling millimetre-wave UAV A2G link illustrates in Fig. 5.1, where the ground node is equipped with N_{R} antennas, while the UAV has a single antenna due to the weight and size constraints [103]. The UAV is assumed hovering at a height H above the ground and its horizontal location is $(0,0)$. The horizontal location of the ground node is denoted by $\mathbf{w} \in \mathbb{R}^{2\times 1}$. Thus, the distance between the UAV and the ground node is given by $d = \sqrt{H^2 + \|\mathbf{w}\|^2}$. The path loss between the UAV and the ground node is given by [93]

$$P_{\mathrm{L}} = \left(\frac{4\pi d f}{c}\right)^2 \left(\mathbf{P}_{\mathrm{LoS}}\mu_{\mathrm{LoS}} + \mathbf{P}_{\mathrm{NLoS}}\mu_{\mathrm{NLoS}}\right), \tag{5.1}$$

where f is the signal frequency, c is the speed of light, $\mathbf{P}_{\mathrm{LoS}}$ and $\mathbf{P}_{\mathrm{NLoS}}$ are the LoS and the NLoS probability between the UAV and the ground node, and μ_{LoS} and μ_{NLoS} are the additional attenuation factors of the LoS and the NLoS UAV A2G link, respectively. The LoS probability between the UAV and the ground node is modeled based on the ITU work

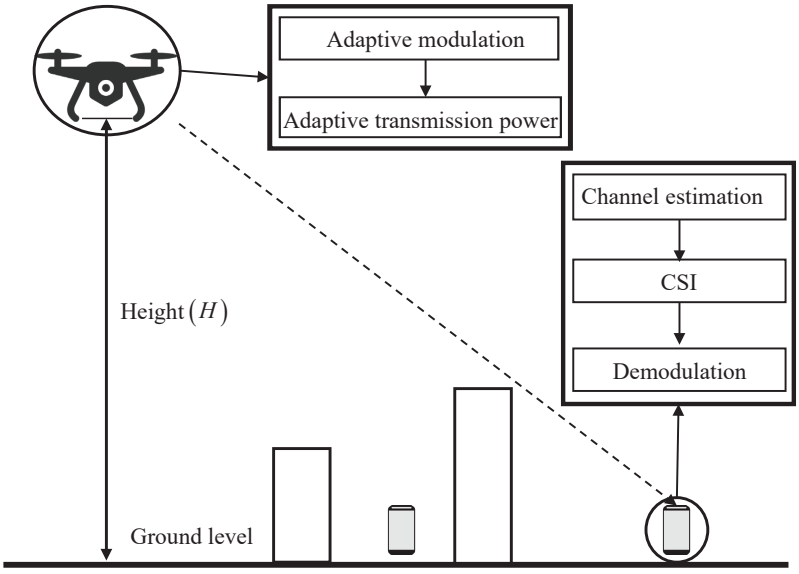

Fig. 5.1 The millimetre-wave UAV A2G link.

[77]. And then, it is simplified to the Sigmoid function form, which is shown below

$$\mathbf{P}_{\mathrm{LoS}}(\theta) = \frac{1}{1 + a\exp\left[-b(\theta - a)\right]}, \tag{5.2}$$

where a and b are parameters to incorporate the environments (rural, urban, dense urban, etc.) [78], and $\theta = \tan^{-1}\left(\frac{H}{\|\mathbf{w}\|}\right)$ is elevation angle. Hence, the NLoS probability between the UAV and the ground node is given as $\mathbf{P}_{\mathrm{NLoS}} = 1 - \mathbf{P}_{\mathrm{LoS}}$.

Each transmission frame is composed of a fixed channel estimation period T_{e} (seconds) followed by a variable signal transmission period T_{c} (seconds), which is long enough to allow the transmission of at least one symbol. The frame structure schematic diagram is shown in Fig 5.2. In the channel estimation period, the UAV transmits mutually orthogonal pilot sequences to the N_{R} receiving antennas at the ground node, where the CSI of the A2G channel is estimated for the current transmission frame. Based on the estimated CSI, the ground node decides the modulation order and the transmission power for A2G transmission and sends the decision to the UAV without any error or delay. This assumption is made for analytical trackability. In the signal transmission period, the UAV will transmit data signal

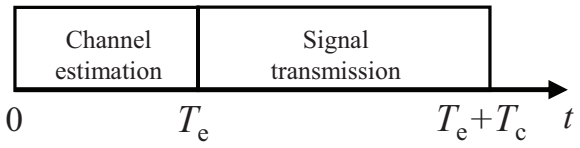

Fig. 5.2 The schematic diagram of the frame structure.

using the modulation order and transmission power level informed by the ground node, and the ground node receiver will use the estimated CSI to demodulate the received signal.

Without loss of generality, we assume that the current transmission frame starts at time t = 0. The average transmission rate in a transmission frame is given by

$$R_{\text{ave}}(T_c) = \frac{1}{T_e + T_c} \int_{T_e}^{T_e+T_c} R(t)\,\mathrm{d}t, \tag{5.3}$$

where $R(t)$ is the transmission rate (bit/symbol) at time t.

The total power consumption of the UAV includes the communication-related power and the propulsion power. The communication-related power is caused by radiation, signal processing, and other circuitry in the UAV. The UAV propulsion power is used to support the UAV mobility and hovering. The UAV circuitry power consumption P_c and the UAV propulsion power consumption P_p are set constant for analytical simplicity [23, 121].

The energy efficiency (in bits/Joule) is defined as the ratio of the transmission rate based on the adaptive modulation $R(t)$ to the total power consumption of the UAV working and can be expressed as

$$\eta = \frac{\sum_0^t R(t)}{\sum_0^t \left(P_{\min}(t) + P_L + P_c + P_p\right)}, \tag{5.4}$$

where $P_{\min}(t)$ is the minimum instantaneous transmission power.

5.2.2 Problem Formulation

In the 5G and beyond communications, UAVs may work in some disaster emergency situations, where the long working time is one of the vital requirements for the UAV A2G link

[93]. Since the battery capacity is limited to the size of the UAV, the power consumption problems should also be considered [120].

We formulate the following optimization problem to minimize the transmission power of the millimetre-wave UAV A2G link under UAV wobbling while maintaining the maximized average transmission rate of adaptive modulation subject to the BEP threshold, i.e.,

$$
\begin{aligned}
(\mathrm{P2}): \quad & \min \quad P(t), && (5.5)\\
& \text{s.t.} \quad 0 \leq t \leq T_{\mathrm{e}} + T_{\mathrm{c}}, && (5.5a)\\
& \qquad R_{\mathrm{ave}}(t) = R_{\mathrm{ave,max}}, && (5.5b)\\
& \qquad \beta_i \leq \beta_{\mathrm{th}}, && (5.5c)\\
& \qquad 0 < P(t) \leq P_{\mathrm{max}}, && (5.5d)
\end{aligned}
$$

where (5.5a) is the constraint on power control policy adopting period; (5.5b) requires the transmission rate must be kept at the highest instantaneous transmission rate; (5.5c) requires that the instantaneous BEP β_i of the wobbling millimetre-wave UAV A2G link must be kept below the predetermined BEP threshold β_{th}; (5.5d) is the adaptive transmission power constraint on maximum transmission power P_{max}. Fig. 5.3 shows a schematic diagram of the optimization of the transmission power.

5.3 Power Control Policy

In this section, how the power control policy working with the optimum adaptive modulation scheme for saving power is described. The power control policy should adaptively adjust the transmission power based on the BEP and the transmission rate to cooperate with the adaptive modulation scheme.

The SNR is a key parameter to bridge the transmission power and the system performance. The minimum instantaneous transmission power can be achieved when the minimum required instantaneous SNR is employed in the transmission frame [122]. Although it is hard to get the value of the instantaneous SNR directly from (4.9), an alternative expression of BEP

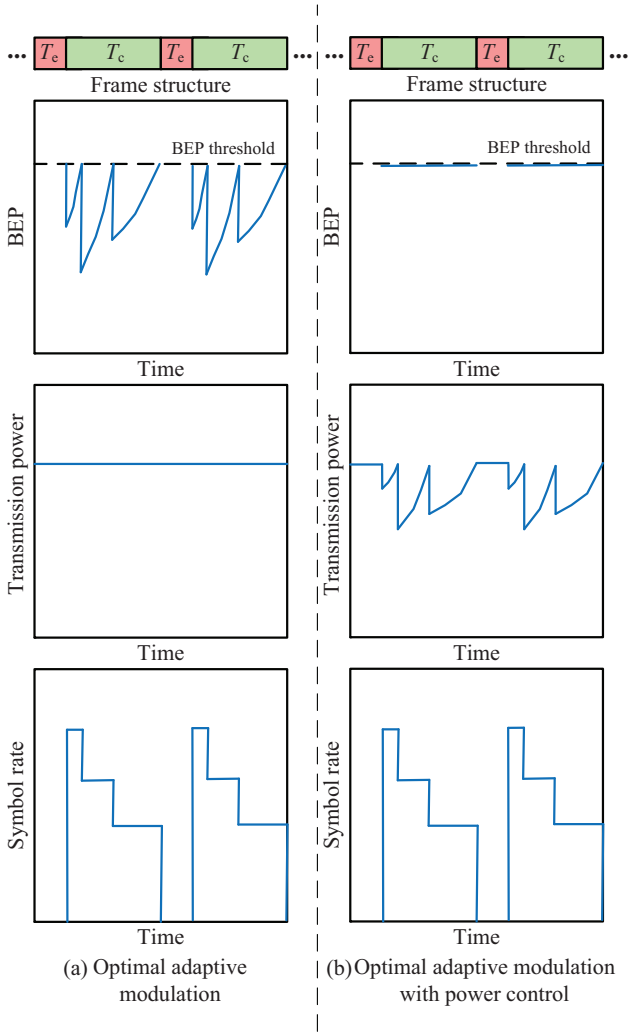

Fig. 5.3 The schematic diagram of the defined problem and potential solutions.

exists to reduce the complexity of computation. According to [123], the signal-space concept could be used to obtain accurate BEP approximations of (4.9) for M-ary PSK modulation scheme. For the signal-space concept, an error in an adjacent symbol is accompanied by one and only one bit error based on the Gray code mapping property. For M-ary PSK and $|s_m| = 1$, (4.9) based on signal-space concept [123] can be rewritten as

$$\beta_{\text{th}} = \begin{cases} Q\left(\sqrt{\dfrac{2\left\|\sqrt{\gamma}\mathbf{h}(T_e)C(T_e,t)\right\|^2}{\gamma\left(1-C(T_e,t)^2\right)|s_m|^2+1}}\right), & M=2, \\ \dfrac{2}{\log_2(M)}Q\left(\sqrt{\dfrac{\left\|\sqrt{\gamma}\mathbf{h}(T_e)C(T_e,t)\right\|^2\left(1-\cos\left(\frac{2\pi}{M}\right)\right)}{\gamma\left(1-C(T_e,t)^2\right)|s_m|^2+1}}\right), & M>2. \end{cases} \tag{5.6}$$

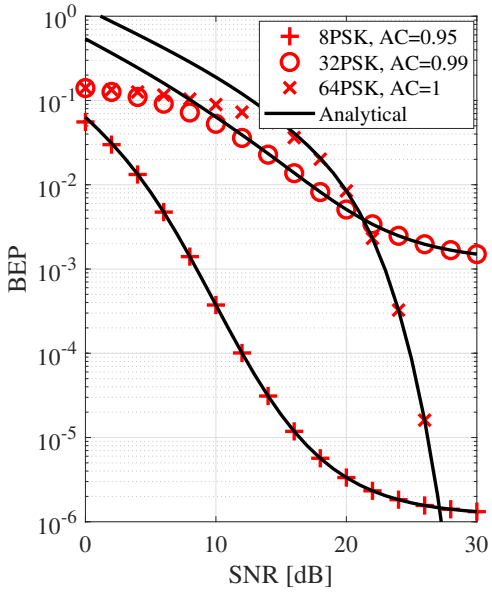

Fig. 5.4 The BEP approximation of (4.9) employing M-ary PSK. Markers show approximate results and solid lines illustrate analytical results. AC denotes the value of temporal ACF.

Fig. 5.4 shows the BEP approximations of M-ary PSK modulation scheme are close to the analytical upper bound on the BEP of the sub-optimum detector in high SNR regime. The analytical and approximation results are computed by (4.9) and (5.6), respectively.

We take the derivation of (5.6) with respect to the BEP threshold β_{th} and obtain the instantaneous SNR,

$$\gamma_{\min} = \begin{cases} \dfrac{\mathrm{Q}^{-1}(\beta_{\text{th}})^2}{2\|\mathbf{h}(T_{\text{e}})C(T_{\text{e}},t)\|^2 - \left(1-C(T_{\text{e}},t)^2\right)\mathrm{Q}^{-1}(\beta_{\text{th}})^2}, & M=2, \\ \dfrac{\alpha^2}{\|\mathbf{h}(T_{\text{e}})C(T_{\text{e}},t)\|^2(1-\cos(2\pi/M)) - \left(1-C(T_{\text{e}},t)^2\right)\alpha^2}, & M>2, \end{cases} \tag{5.7}$$

where $\alpha = \mathrm{Q}^{-1}\left(\frac{\beta_{\text{th}}\log_2(M)}{2}\right)$ and $\mathrm{Q}^{-1}(\cdot)$ stands for the inverse function of the Q-function.

For M-ary QAM ($M>2$), the instantaneous SNR of the millimetre-wave UAV A2G link is the root of

$$\beta_{\text{th}} = \sum_{m=1}^{M}\sum_{\hat{m}=1}^{M} \frac{\mathcal{N}_{(m\to\hat{m})}\mathrm{P}_{(m\to\hat{m})}}{M\log_2(M)}. \tag{5.8}$$

Then, the Newton-Raphson method [124] could be employed to derive the approximation root, which is provided in Lemma 1. More specifically, Lemma 1 should be replicated

multiple times to get an accurate approximation root of (5.8) as the instantaneous SNR of the millimetre-wave UAV A2G link under UAV wobbling.

Lemma 5.1. The approximation root of (5.8) using the Newton-Raphson method is given by

$$\gamma_{\mathrm{re}+1} = \gamma_{\mathrm{re}} \left(\frac{u_m}{\beta_{\mathrm{th}}} \right)^{\frac{u_m}{v_m}}, \tag{5.9}$$

where

$$u_m = \sum_{m=1}^{M} \sum_{\hat{m}=1}^{M} \frac{\mathscr{N}_{(m\to\hat{m})} \mathrm{Q}\left(\sqrt{\frac{\Lambda\gamma_{\mathrm{re}}}{\psi\gamma_{\mathrm{re}}+2}} \right)}{M \log_2(M)}, \tag{5.10}$$

$$v_m = \sum_{m=1}^{M} \sum_{\hat{m}=1}^{M} \frac{\mathscr{N}_{(m\to\hat{m})} \Lambda \sqrt{\gamma_{\mathrm{re}}} \exp\left(-\frac{\Lambda\gamma_{\mathrm{re}}}{2\psi\gamma_{\mathrm{re}}+4} \right)}{M \log_2(M) \sqrt{2\pi\Lambda \left(\gamma_{\mathrm{re}}\psi + 2\right)^3}}, \tag{5.11}$$

$$\Lambda = \left\| \mathbf{h}\left(T_{\mathrm{e}}\right) C\left(T_{\mathrm{e}}, t\right) \right\|^2 \left| s_m - s_{\hat{m}} \right|^2, \tag{5.12}$$

$$\psi = 2\left(1 - C\left(T_{\mathrm{e}}, t\right)^2\right) \left| s_m \right|^2, \tag{5.13}$$

γ_{re} stands the initial guess root, and $\gamma_{\mathrm{re}+1}$ is the result of approximation root.

Proof. According to (5.8), we can obtain

$$f(\gamma_{\mathrm{re}}) = \ln(\beta_{\mathrm{th}}) - \ln\left(\sum_{m=1}^{M} \sum_{\hat{m}=1}^{M} \frac{\mathscr{N}_{(m\to\hat{m})} \mathrm{Q}\left(\sqrt{\frac{\Lambda\gamma_{\mathrm{re}}}{\psi\gamma_{\mathrm{re}}+2}} \right)}{M \log_2(M)} \right) = 0, \tag{5.14}$$

where $\mathrm{Q}(x) = \int_x^{+\infty} \frac{1}{\sqrt{2\pi}} e^{\left(-\frac{w^2}{2}\right)} \mathrm{d}w$.

According to Newton–Raphson method, the approximation root can computed as

$$\ln(\gamma_{\mathrm{re}+1}) = \ln(\gamma_{\mathrm{re}}) - \frac{f(\gamma_{\mathrm{re}})}{f'(\gamma_{\mathrm{re}})}. \tag{5.15}$$

We take the derivation of (5.14) with respect to γ_{re} and obtain

$$\ln(\gamma_{\mathrm{re}+1}) = \ln(\gamma_{\mathrm{re}}) - u_m \frac{\ln(\beta_{th}) - \ln(u_m)}{v_m}. \tag{5.16}$$

After reforming (5.16), we obtain (5.9). □

In general, the thermal noise power is calculated by $N_0(\text{dBm}) = 10\log_{10}(k_\text{b}TB)$, where k_b is the Boltzmann constant (1.38×10^{-23} J/K), T is temperature in K, and B is bandwidth. Therefore, the minimum instantaneous transmission power is derived as

$$P_{\min}(t)\,(\text{dBm}) = \gamma_{\min}(t) + P_\text{L} + N_0. \tag{5.17}$$

To support the adaptive modulation with the power control policy, an extra control message is required from the ground node to inform the UAV of the initial transmission rate $R_{\max}$ (one integral number) and the corresponding switching transmission time t_n (multiple floating numbers) required for adaptive modulation, and the transmission power $P(t)$ (multiple floating numbers) required for power control.

5.4 Energy Efficiency of The Millimetre-wave UAV A2G Link

The transmission rate and the transmission power have been related to support evaluation of EE performance in the millimetre-wave UAV A2G link under imperfect CSI. The evaluation of EE performance can help know the effective of power control policy. Following (5.4), the EE performance of the adaptive modulation scheme with power control policy under imperfect CSI can be evaluated.

The proposed methodology here is to optimize the signal transmission time to provide the millimetre-wave UAV A2G link under wobbling with high EE performance. This optimization is different with what have done in the chapter 4, where the transmission time is optimized to achieve the maximum average transmission rate of the millimetre-wave UAV A2G link. The objective of our work is to maximize the system EE, thus maximizing the throughput while minimizing the power consumed, which is evident form (5.4). Moreover, due to the imperfect CSI and the adaptive modulation properties, we formulated the optimization problem to maximize EE of the millimetre-wave UAV A2G link

under wobbling by optimizing the signal transmission time, i.e.,

$$(\mathrm{P3}): \quad \max_{t} \quad \eta, \tag{5.18}$$

$$\text{s.t.} \quad 0 < P_{\mathrm{T}}(t) \leq P_{\max}, \tag{5.18a}$$

$$R_{\min} \leq \frac{\sum_0^t R(t)}{t}, \tag{5.18b}$$

$$\mathrm{BEP} \leq \beta_{\mathrm{th}}, \tag{5.18c}$$

where (5.18a) is the adaptive transmission power constraint on the maximum transmission power and $P_{\mathrm{T}}(t) = P_{\mathrm{r}}(t) + P_{\mathrm{L}}$; (5.18b) is the spectral efficiency constraint on the minimum required spectral efficiency; (5.18c) requires that the BEP of the system must be kept below the predetermined BEP threshold β_{th}.

The kind of dual-optimization problem is solved by first applying power control policy to compute the minimum power required to transmit information data reliably for the adaptive modulation. Since the (5.4) is a nonlinear equation, we solve the optimization problem through the numerical method to obtain the optimal signal transmission time for the mm-wave UAV A2G link under aged CSI. The pseudo-code of the proposed optimal signal transmission time finder is given in Algorithm 2.

Algorithm 2: The optimum transmission time finder.

Input: T_{e}, $R(t)$, t, $R_{\min}$, P_{c}, P_{p}, P_{L}.
Output: t_{op}.
$P_{\mathrm{r}}(t) \leftarrow$ (5.17) with $R(t)$;
$P_{\mathrm{T}}(t) \leftarrow P_{\mathrm{r}}(t)$ and P_{L};
$R_{\mathrm{ave}}(t) \leftarrow \frac{\mathrm{sum}(R(t))}{t}$;
if $R_{\mathrm{ave}}(t) \geq R_{\min}$ **then**
  $\eta(t) \leftarrow$(5.4) with $R(t)$, $P_{\mathrm{T}}(t)$, P_{c}, and P_{p};
end
$t_{\mathrm{op}} \leftarrow \mathrm{find}(\eta == max(\eta))$;

Table 5.1 Simulation Parameters

Carrier frequency (f)	28 GHz
Additional path loss by LoS connection (μ_{LoS})	1.6
Additional path loss by NLoS connection (μ_{NLoS})	23
Dense urban environemnt constants (a, b)	(12.08, 0.11)
Number of antenna at receiver (N_{R})	8
Maximum transmission power ($P_{\max}$)	35 dBm
Power of thermal noise (N_0)	94 dBm
Power of circuitry (P_{c})	1 w
Power of propulsion (P_{p})	168 w
Mechanical vibration frequency of the UAV ω_{v}	20π
Correlation of UAV wobbling velocity μ	30
Temperature T	300 K

5.5 Numerical Results

In this section, the performance of the power control algorithm of a millimetre-wave UAV A2G link under imperfect CSI is evaluated. How effective the power control policy of optimum adaptive modulation scheme will be shown. The EE performance of the adaptive modulation scheme under imperfect CSI with power control policy is discussed. The simulator has a UAV and a ground node with a horizontal distance of 50 m and the UAV hover height constraint is set as 120 m [16]. The signal estimation time is set as 1 ms using 100 MHz bandwidth. The adaptive modulation scheme under wobbling is adopted and the simulation results presented in this paper are averaged over 1000 different CSI. The BEP threshold is fixed to 10^{-6} in all examples to keep the data signals transmission reliable [115]. Following [93], the path loss model parameters are summarized in Table 5.1.

The continuous temporal ACF is provided in (5.19) [112],

$$C(\Delta t) = e^{-0.5\sigma_{\text{v}}^2\left(\frac{\omega_{\text{c}}}{c\left(\omega_{\text{v}}^2+\mu^2\right)}\right)^2\left(\mu\Delta t\left(\omega_{\text{v}}^2+\mu^2\right)-2\mu\omega_{\text{v}}\sin(\omega_{\text{v}}\Delta t)e^{-\mu\Delta t}+\left(\mu^2-\omega_{\text{v}}^2\right)\cos(\omega_{\text{v}}\Delta t)e^{-\mu\Delta t}-\mu^2+\omega_{\text{v}}^2\right)} \times J_0\left(j0.5\sigma_{\text{v}}^2\left(\frac{\omega_{\text{c}}}{c}\right)^2\frac{\mu\sin(\omega_{\text{v}}\Delta t)-\omega_{\text{v}}\cos(\omega_{\text{v}}\Delta t)+\omega_{\text{v}}e^{-\mu\Delta t}}{\left(\omega_{\text{v}}^2+\mu^2\right)\omega_{\text{v}}}\right). \tag{5.19}$$

where $\Delta t = t - T_{\text{e}}$, $J_0(\cdot)$ denotes the Bessel function of the first kind with an order zero, σ_{v}^2 is the variance of the UAV movement velocity, ω_{c} is the carrier frequency, ω_{v} is mechanical

vibration frequency of the UAV, μ is the parameter to measure how fast the envelope of velocity changes with time. In this equation, the μ and ω_v are two key parameters to describe how the temporal ACF of millimetre-wave UAV A2G link impacts by the UAV wobbling. The transmission rate is following the transmission scheme used. The general system parameters used for temporal ACF and system model simulation to obtain the results are shown in Table 5.1.

The performances of adaptive modulation scheme with and without power control for the BEP threshold at 10^{-5} employing M-ary PSK or M-ary QAM modulation schemes under case 1 and 2 from Appendix B.3 are shown in Fig. 5.5, 5.6, 5.7, and 5.8, respectively. The initial guess root of Newton-Raphson method for M-ary QAM is 30. The transmission power under power control policy can adapt to the different modulation orders and schemes for maintaining the instantaneous BEP performance below the BEP threshold. The instantaneous BEP computed by the adaptive modulation scheme with power control is close to the BEP threshold, which can save energy comparing with the adaptive modulation scheme without power control. When the channel information is different, the average transmission power for adaptive modulation scheme and the percentage of power-saving in watts are different. Hence, the replication experiment are computed to obtain the average percentage of the power-saving for the power control policy.

For whole adaptive modulation transmission period, the average transmission power for M-ary PSK or M-ary QAM modulation scheme with the power control policy at the BEP threshold 10^{-5} for replication are 21.5 dBm and 21.6 dBm. Therefore, the percentage of power-saving in watts under power control comparing with adaptive modulation scheme without power control policy for M-ary PSK or M-ary QAM modulation scheme are 95.5% and 95.4%. For whole adaptive modulation transmission period, the power control policy has similar effect between M-ary PSK and M-ary QAM modulation scheme because the low modulation order transmission wastes more energy than high modulation order and low modulation order transmission period is longer than high modulation order.

For optimum adaptive modulation transmission period from chapter 4, the average transmission power for M-ary PSK or M-ary QAM modulation scheme with the power

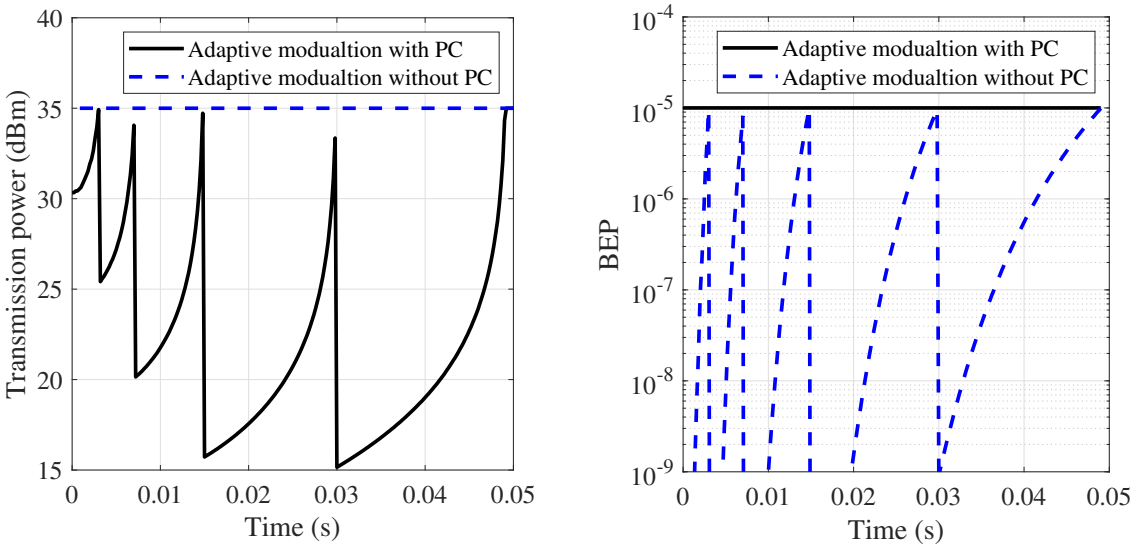

(a) Transmission power (b) BEP

Fig. 5.5 The performance of power control policy for the adaptive modulation scheme for M-ary PSK and BEP threshold at 10^{-5} under case 1. The solid line is the adaptive modulation scheme with power control and the dash line is the adaptive modulation scheme without power control

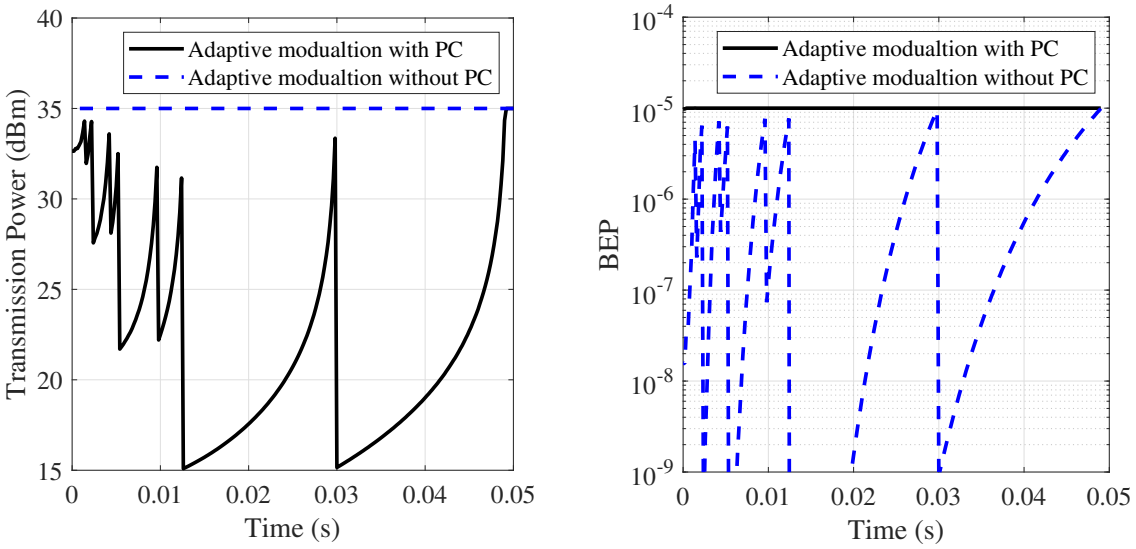

(a) Transmission power (b) BEP

Fig. 5.6 The performance of power control policy for the adaptive modulation scheme for M-ary QAM and BEP threshold at 10^{-5} under case 1. The solid line is the adaptive modulation scheme with power control and the dash line is the adaptive modulation scheme without power control.

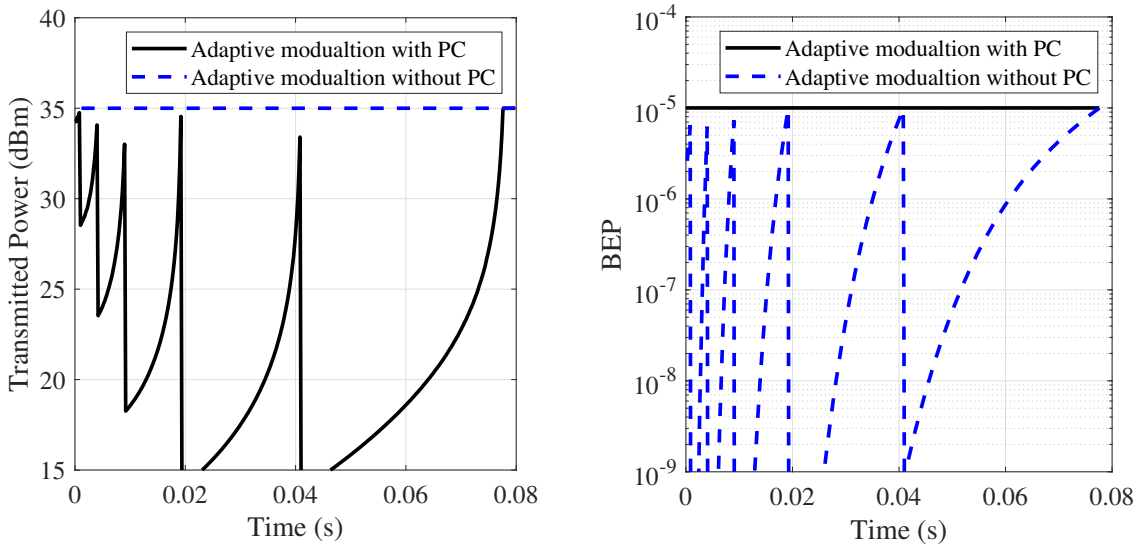

(a) Transmission power (b) BEP

Fig. 5.7 The performance of power control policy for the adaptive modulation scheme for M-ary PSK and BEP threshold at 10^{-5} under case 2. The solid line is the adaptive modulation scheme with power control and the dash line is the adaptive modulation scheme without power control

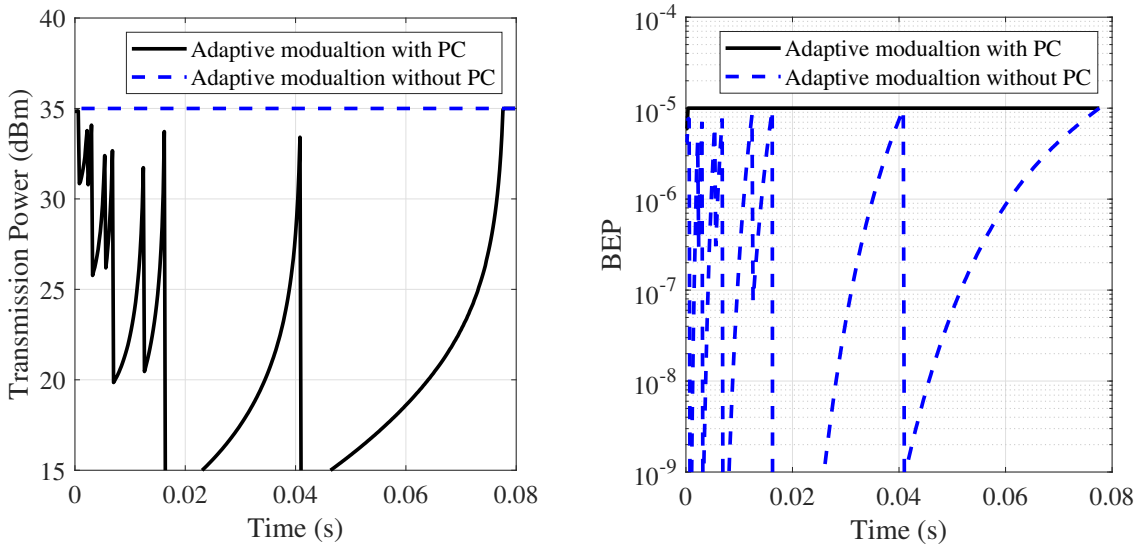

(a) Transmission power (b) BEP

Fig. 5.8 The performance of power control policy for the adaptive modulation scheme for M-ary QAM and BEP threshold at 10^{-5} under case 2. The solid line is the adaptive modulation scheme with power control and the dash line is the adaptive modulation scheme without power control.

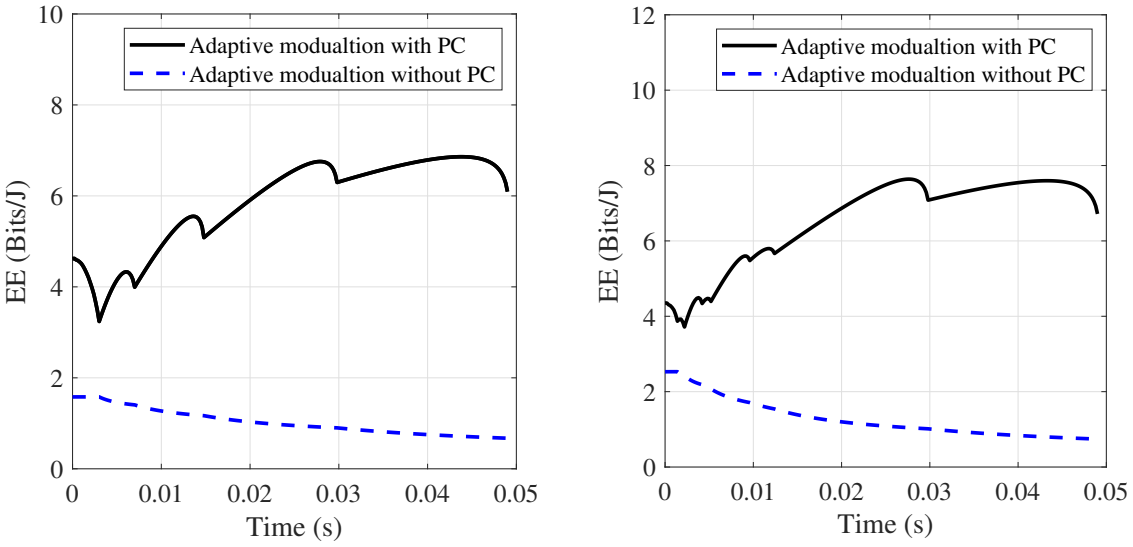

(a) PSK (b) QAM

Fig. 5.9 EE performance of adaptive modulation employing M-ary PSK or M-ary QAM modulation scheme under imperfect CSI for case 1. The solid line is the adaptive modulation scheme without power control and the dash line is the adaptive modulation scheme with power control.

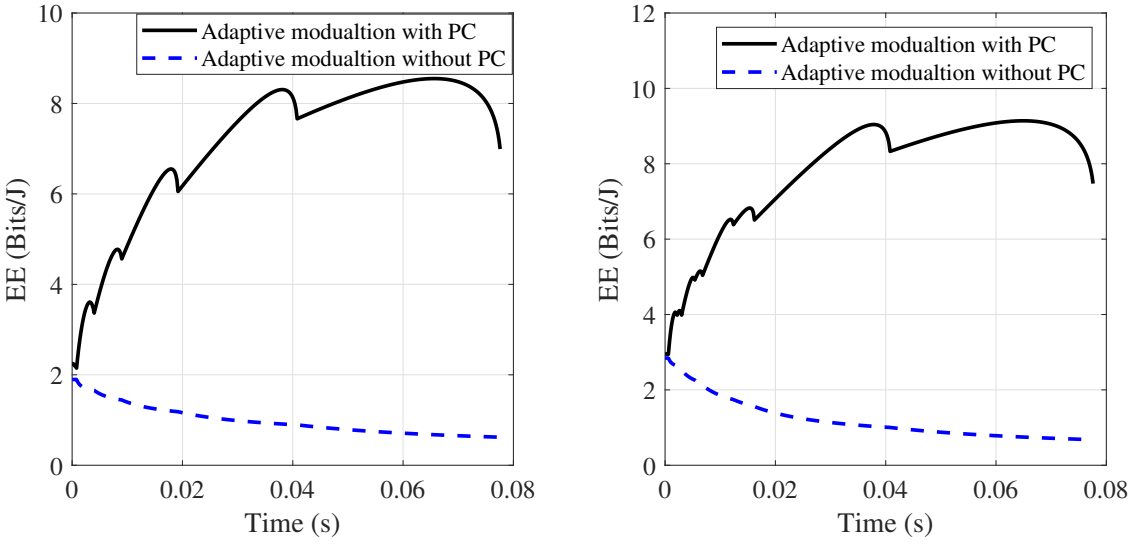

(a) PSK (b) QAM

Fig. 5.10 EE performance of adaptive modulation employing M-ary PSK or M-ary QAM modulation scheme under imperfect CSI for case 2. The solid line is the adaptive modulation scheme without power control and the dash line is the adaptive modulation scheme with power control.

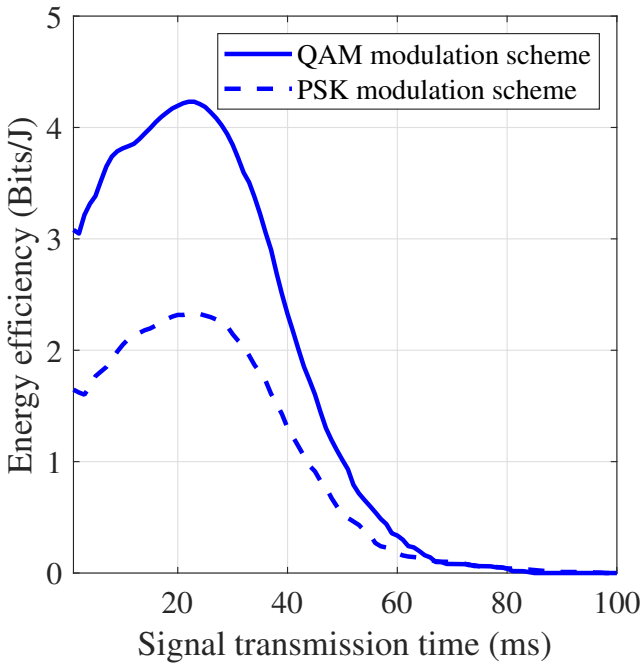

Fig. 5.11 The energy efficiency changing with the signal transmission time for M-ary QAM and M-ary PSK signals ($R_{\min} = 1$ bit/symbol, $H = 100$ m).

control policy at the BEP threshold 10^{-5} for replication are 30.1 dBm and 31.8 dBm. Therefore, the percentage of power-saving in watts under power control comparing with optimum adaptive modulation scheme without power control policy for M-ary PSK or M-ary QAM modulation scheme are 67.7% and 52.2%. For optimum adaptive modulation scheme, the power control policy has a better effect on the PSK scheme because more power wastes in the PSK scheme. Hence, the M-ary PSK is waste more power in transmission period than M-ary QAM and the power control policy is more important for M-ary PSK.

In Fig. 5.9 and 5.10, the EE performance of the adaptive modulation with power control policy and without power control policy is compared where BEP threshold is 10^{-5}. The power control policy improve the EE performance significantly for adapative modulation employing M-ary PSK or M-ary QAM modulation scheme for different CIRs. The EE performance of adaptive modulation without power control policy decreases with the time increasing.

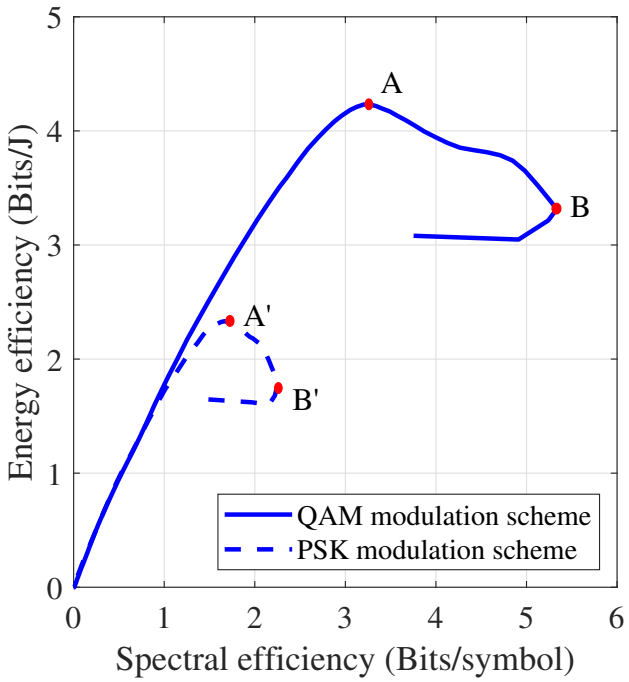

Fig. 5.12 System spectral-energy efficiency trade-off ($R_{\min} = 1$ bit/symbol, $H = 100$ m).

Fig. 5.11 illustrates how the EE changes with the transmission time increasing for M-ary PSK and M-ary QAM modulation schemes. The simulation UAV hover height is 100 m to keep the high LoS probability. The EE of the system has the optimal point for trade-off the signal transmission time and estimation time in one transmission frame under aged CSI. The figure also shows the optimal transmission time is computed by numerically solving (5.18). The M-ary QAM signals have the better EE performance than the M-ary PSK signals because the average transmission rate of M-ary QAM signals is higher than that of the M-ary PSK signals.

Fig. 5.12 shows how the EE changes with the increase in the spectral efficiency for M-ary PSK and M-ary QAM modulation schemes. The flat segment shows the spectral efficiency has no impact on the EE because the power consumption is stable to satisfy (5.18a) for the highest transmission rate of the adaptive modulation under aged CSI. Excepting the flat segment, when the spectral efficiency increases, the EE of the millimetre-wave UAV A2G link under wobbling will increase first and then decreases. This is because the aged CSI has the significant impact on the transmission rate, which is dominant in the spectral efficiency

and EE. The spectral-energy efficiency trade-off is recommended at segment AB and A'B' for M-ary QAM signals and M-ary PSK signals, respectively.

5.6 Conclusions

In this chapter, we have proposed the novel power control policy of the millimetre-wave UAV A2G link under imperfect CSI. The power control policy of the optimum adaptive modulation scheme is presented, which can save 67.7% and 52.2% power compared with adaptive modulation without power control, at the ABEP threshold 10^{-5} for PSK and QAM scheme, respectively. The EE performance with adaptive modulation scheme and the power control policy of the millimetre-wave UAV A2G link under imperfect CSI is significantly improved comparing with the adaptive modulation without power control. The EE performance is changed with the BEP threshold change. These can give a guideline for engineers to design the green millimetre-wave UAV A2G link for maintaining the BEP performance under the maximum tolerable BEP threshold while maximising the average transmission rate.

Chapter 6

Conclusions and Future Works

6.1 Conclusions

Throughout the thesis, comprehensive studies in the millimetre-wave UAV A2G channel model under wobbling and the performance analysis method have been achieved, and their key performance was evaluated along with the proposal of novel solutions to enhance the original performance.

The state-of-the-art literature review focused on the basic properties of the millimetre-wave, popular channel model methods and the millimetre-wave UAV A2G channel model, and the millimetre-wave UAV A2G link performance analysis. The basic properties of the millimetre-wave and UAVs with suitable channel model methods could build the UAV A2G channel model for different communication situations to known channel characteristics properties. UAV types, propagation environments, and electromagnetic wave properties have significant influences on the channel characteristics, e.g., the Doppler shift, the temporal ACF, the spatial correlation, etc.. The UAV A2G channel model is one of the key characteristics for investigating the UAV A2G link. The performance analysis of the UAV A2G link in the existing paper mainly focused on coverage probability, LoS probability, throughput, and EE. These works give the guideline for engineering to design the millimetre-wave UAV A2G communications.

To investigate the wobbling impact of the millimetre-wave UAV A2G link, the research about the channel model of the wobbling millimetre-wave UAV A2G link should be studied. In chapter 3, the analytical model of the Doppler effect brought by the mechanical wobbling in the millimetre-wave RW UAV A2G link is proposed. Applying the RW UAV wobbling movement model at hovering status, the closed-form expression of temporal ACF has been derived and verified via Monte Carlo simulation. Moreover, the Doppler PSD of the millimetre-wave RW UAV channel has been computed based on the analytical temporal ACF. Numerical results show that the mechanical vibration frequency and the radial velocity envelope covariance interact on the decrease rate and fluctuation model of temporal ACF. The Doppler spread range broadens as mechanical vibration frequency enhances while the value and number of the Doppler PSD bulge degrade as radial velocity envelope covariance increases. A key observation is that even for weak UAV wobbling, the BEP of the UAV A2G link deteriorates quickly, making the link difficult to establish a reliable communication link. Therefore, the UAV designer has to jointly consider the vibration frequency and the radial velocity envelope covariance carefully to mitigate the impact of the Doppler effect brought by the RW UAV mechanical wobbling on the A2G wireless link.

After studying the channel model of the wobbling millimetre-wave UAV A2G link, the wobbling has the significant impact on the channel suitability and leads to the BEP decrease. To overcome this problem, in chapter 4, the novel adaptive modulation scheme of the millimetre-wave UAV A2G link under imperfect CSI was proposed. The channel estimation time and transmission time of the adaptive modulation transmission frame will have an optimized trade-off based on the proposed algorithm to achieve the maximum average transmission rate subject to the maximum tolerable BEP threshold. These can give a guideline for engineers to design the millimetre-wave UAV A2G link for maintaining the BEP performance under the maximum tolerable BEP threshold while maximising the average transmission rate.

Since the on-board power limitation of the UAV is the emergence challenge for UAV working, the power control policy should be investigated to extend the UAV working time. In chapter 5, the novel power control policy of the millimetre-wave UAV A2G link under

imperfect CSI was proposed. The power control policy of the optimum adaptive modulation scheme is presented, which can save 67.7% and 52.2% power compared with adaptive modulation without power control at the BEP threshold 10^{-5} for PSK and QAM schemes, respectively. The EE performance of the millimetre-wave UAV A2G link under imperfect CSI with an adaptive modulation scheme and the power control policy is significantly improved comparing with the adaptive modulation without power control at the BEP threshold 10^{-5} for PSK and QAM schemes. These can give a guideline for engineers to design the green millimetre-wave UAV A2G link for maintaining the BEP performance under the maximum tolerable BEP threshold for abundant modulation methods.

Overall, a channel model, a novel adaptive modulation scheme and a power control policy of wobbling millimetre-wave UAV A2G link to keep the system working well are discussed in this thesis.

6.2 Future Works

In this subsection, the challenges and issues with future research directions of millimetre-wave UAV communications for beyond 5G and sixth-generation (6G) communication system are discussed.

- **MIMO for UAV Communication systems**

  Since MIMO or massive MIMO is one of the key technologies in future communication systems, the combination of MIMO and UAV communications should be considered [125]. However, the limited space in UAVs makes the large antenna array installation difficult. Fortunately, the short wavelength of millimetre-wave may miniaturize the size of the MIMO antenna array to support the MIMO technology in UAV communications [6]. Hence, the MIMO antenna configurations of UAVs, and measurements and channel modelling of MIMO or massive MIMO channels in millimetre-wave UAV communication systems should be paid more attention.

- **Wideband UAV Communication systems**

  The narrowband channel model is defined as the signal bandwidth much less than the coherence bandwidth of the multipath fading process, whereas in the definition of wideband channel models the situation is versus [31]. The narrowband channel sounding tests consider the magnitude and phase of a single frequency and the wideband uses frequency domain analysis. For wideband channels, it is composed of many propagation paths including: LoS direct path, reflection path, and scattering path. These propagation paths will lead to more channel statistics parameters than narrowband channel situations, e.g., RMS delay spread [126]. Hence, the measurements and channel model of wideband UAV communication systems should be paid more attention.

- **Reconfigurable Intelligent Surface**

  Reconfigurable intelligent surface (RIS), also referred to as intelligent reflection surface (IRS), is composed of an array of reflecting elements to independently reflect incident signals with reconfigurable amplitudes and phases, which could improve signal quality at direct communication links suffering from blockage [127]. In previous literature [128], the passive beamforming technique is used to adjust phase shifts of all reflection elements in RIS. Hence, the RIS is energy-efficient and cost-effective to use in urban scenarios, where the UAV may have many blockages at low altitudes. The RIS-assisted UAV communications can extend the coverage and reliability of the A2G, accounting for the UAV height and transmission scenarios [129], which is shown in Fig. 6.1. The deployment and trajectories optimization of RIS-assisted UAV communications in practical large-scale networks is the emerging trend in this topic.

- **Space-air-ground-sea Integrated Network**

  The space-air-ground-sea integrated network is new propagation scenarios in the 6G communication system including satellite, UAV, terrestrial, and maritime communications to provide seamless global network coverage, which is shown in Fig. 6.2 [125]. The low altitude UAV scenario in the urban scenario should be considered because the

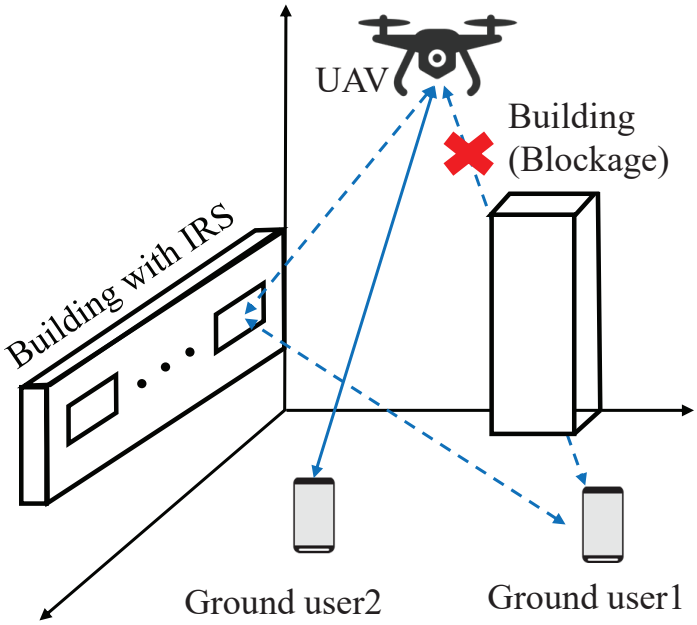

Fig. 6.1 Illustration of RIS in UAV-enabled wireless networks. The dashed and solid arrows denotes NLoS and LoS links, respectively.

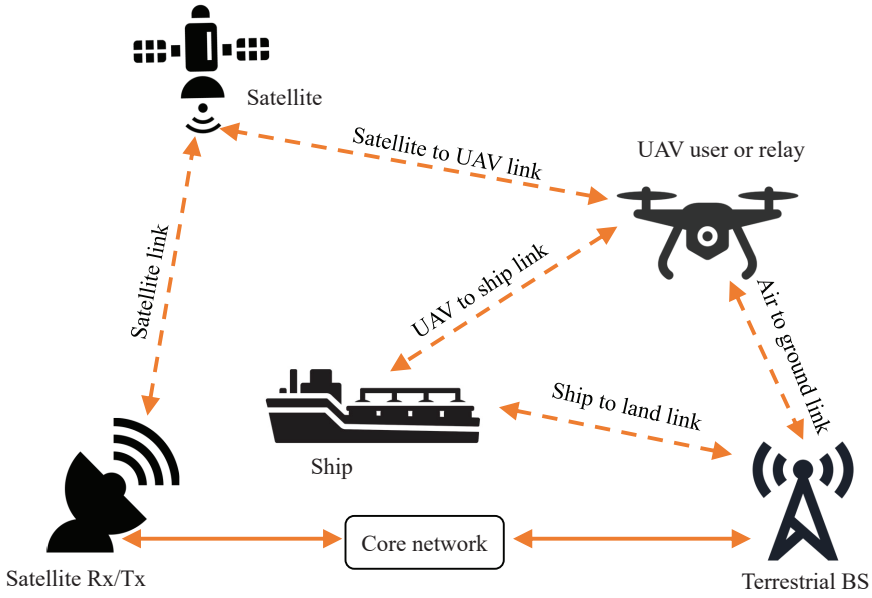

Fig. 6.2 Potential architecture for a space-air-ground-sea integrated network supporting a UAV. The dashed and solid arrows denotes wireless and wired links, respectively. Rx: receiver; Tx: transmitter.

probability of the LoS link will decrease and the tangential velocity will lead to the Doppler effect when the UAV locates at a low altitude [50] [112]. Beyond the A2G wireless channel, the air-to-air (A2A) wireless channel should be modelled to support space-air-ground-sea integrated networks [16]. Satellite communications can fill the ground coverage gaps with feasible services, abundant frequencies band, and lower cost. The protocol, the Doppler effect, and the weather effect are mainly challenges to overcome for the UAV-to-satellite communications [130].

- **UAV Communication at Terahertz Frequency**

  Terahertz is a class of electromagnetic waves which frequency spectrum is between 0.1 and 10 THz. The 100 - 300 GHz band of the terahertz has the overlap of the millimetre-wave band, which has similar properties of millimetre-wave, e.g., large bandwidth, high directivity, large path loss, etc. [125]. Researchers have been studied the millimetre-wave band channel characteristics up to 300 GHz. However, the channel characteristics above 300 GHz are still insufficient. UAV communications at terahertz frequency is a new challenge in the domain of the effects of the trajectories and wobbling of the UAV, the power consumption, the system performance analysis, e.g., the coverage probability and the spectrum efficiency [131] [132]. The terahertz frequency as the basic technique in the communication system can be combined with many new techniques in the 6G era, i.e., RIS-assisted terahertz UAV communication system [133].

Appendix A

Appendix of Chapter 3

A.1 Proof of Lemma 3.1

Substituting (3.2) into (3.3), σ_{d}^2 with different time slots t_1 and t_2 can be expressed by

$$\begin{aligned}\sigma_{\mathrm{d}}^2 &= \mathrm{E}\left[\int_0^{\Delta t} a(t_1)\cos(\omega_{\mathrm{v}} t_1+\phi_0)\,\mathrm{d}t_1 \int_0^{\Delta t} a(t_2)\cos(\omega_{\mathrm{v}} t_2+\phi_0)\,\mathrm{d}t_2\right] \\ &= \mathrm{E}\left[\int_0^{\Delta t}\int_0^{\Delta t} a(t_1)\,a(t_2)\cos(\omega_{\mathrm{v}} t_1+\phi_0)\cos(\omega_{\mathrm{v}} t_2+\phi_0)\,\mathrm{d}t_1\mathrm{d}t_2\right]. \end{aligned} \tag{A.1}$$

Since $\mathrm{E}[a(t)a(t+\Delta t)] = \sigma_{\mathrm{v}}^2 e^{-\mu\Delta t}$, $\mathrm{E}[a(t_1)\,a(t_2)]$ can be expressed by

$$\mathrm{E}[a(t_1)\,a(t_2)] = \sigma_{\mathrm{v}}^2 e^{-\mu|t_1-t_2|}. \tag{A.2}$$

Moreover, $\mathrm{E}[\cos(\omega_{\mathrm{v}} t_1+\phi_0)\cos(\omega_{\mathrm{v}} t_2+\phi_0)]$ can be calculated by

$$\begin{aligned}&\mathrm{E}[\cos(\omega_{\mathrm{v}} t_1+\phi_0)\cos(\omega_{\mathrm{v}} t_2+\phi_0)] \\ &\quad = 0.5\mathrm{E}[\cos(2\phi_0+\omega_{\mathrm{v}} t_1+\omega_{\mathrm{v}} t_2)+\cos(\omega_{\mathrm{v}}|t_1-t_2|)] \\ &\quad = 0.5\cos(\omega_{\mathrm{v}}|t_1-t_2|).\end{aligned} \tag{A.3}$$

Then, substitute (A.2) and (A.3) into (A.1), σ_{d}^2 could be shown as

$$\begin{aligned}\sigma_{\mathrm{d}}^2 = 0.5\sigma_{\mathrm{v}}^2 \int_0^{\Delta t}\int_0^{t_2} e^{-\mu(t_2-t_1)}\cos\left(\omega_{\mathrm{v}}\left(t_2-t_1\right)\right)\mathrm{d}t_1\mathrm{d}t_2 \\ +0.5\sigma_{\mathrm{v}}^2 \int_0^{\Delta t}\int_{t_2}^{\Delta t} e^{-\mu(t_1-t_2)}\cos\left(\omega_{\mathrm{v}}\left(t_1-t_2\right)\right)\mathrm{d}t_1\mathrm{d}t_2.\end{aligned} \tag{A.4}$$

After integral computation of (A.4), the result is shown in

$$\begin{aligned}\sigma_{\mathrm{d}}^2 = \sigma_{\mathrm{v}}^2\frac{\mu\Delta t}{\mu^2+\omega_{\mathrm{v}}^2} \\ +\sigma_{\mathrm{v}}^2\frac{\omega_{\mathrm{v}}^2-\mu^2-\omega_{\mathrm{v}}^2e^{-\mu\Delta t}\cos(\omega_{\mathrm{v}}\Delta t)-2\mu\omega_{\mathrm{v}}e^{-\mu\Delta t}\sin(\omega_{\mathrm{v}}\Delta t)+\mu^2e^{-\mu\Delta t}\cos(\omega_{\mathrm{v}}\Delta t)}{\left(\mu^2+\omega_{\mathrm{v}}^2\right)^2}.\end{aligned} \tag{A.5}$$

$\sigma_{\mathrm{v}}^2\frac{\mu\Delta t}{\mu^2+\omega_{\mathrm{v}}^2}$ part in (A.5) shows the main increase trend of σ_{d}^2 when Δt approaches infinity. When $\mu\neq 0$, $\omega_{\mathrm{v}}\neq 0$ and $\mu\neq 0$, $\omega_{\mathrm{v}}=0$, the result shown in (3.4) only considers $\sigma_{\mathrm{v}}^2\frac{\mu\Delta t}{\mu^2+\omega_{\mathrm{v}}^2}$ part in (A.5), because this part have the main influence of σ_{d}^2. When $\omega_{\mathrm{v}}=0$, $\mu=0$ and $\omega_{\mathrm{v}}\neq 0$, $\mu=0$, the result shown in (3.4) can be computed by direct mathematical computation based on (A.5).

A.2 Proof of Theorem 3.1

Based on CIRs of the millimetre-wave UAV A2G link shown in (3.5), the temporal ACF (non-stationary case) can be computed by

$$C\left(t,t+\Delta t\right) = \mathrm{E}\left[e^{-j\frac{\omega_{\mathrm{c}}}{c}\mathrm{Re}\left\{\int_t^{t+\Delta t} a(t)e^{j\left(\omega_{\mathrm{v}}t+\phi_0\right)}\mathrm{d}t\right\}}\right]. \tag{A.6}$$

It can be seen that $C\left(t,t+\Delta t\right)$ is a function of time t and time separation Δt. Since (A.6) includes a definite integral function, the integral part can be calculated by Riemann sum [134], i.e.,

$$C\left(t,t+\Delta t\right) = \mathrm{E}\left[e^{-j\frac{\omega_{\mathrm{c}}}{c}\lim\limits_{N\to\infty}\mathrm{Re}\left\{\frac{\Delta t}{N}\sum\limits_{n=0}^{N-1} a\left(t+\frac{n\Delta t}{N}\right)e^{j\phi_0}e^{j\omega_{\mathrm{v}}\left(t+\frac{n\Delta t}{N}\right)}\right\}}\right]. \tag{A.7}$$

Lemma A.1. The expression of the $a\left(t+\frac{n\Delta t}{N}\right)$ is

$$a\left(t+\frac{n\Delta t}{N}\right)=e^{-\mu\frac{n\Delta t}{N}}b_1+\sqrt{1-e^{-\mu\frac{2\Delta t}{N}}}\sum_{k=2}^{n+1}e^{-\mu\frac{(n+1-k)\Delta t}{N}}b_k. \tag{A.8}$$

Proof. If (A.8) is correct, according to Assumptions 4 in chapter 3, the autocorrelation value of $a\left(t+\frac{n_1\Delta t}{N}\right)$ and $a\left(t+\frac{n_2\Delta t}{N}\right)$ at $n_1<n_2$ should be computed as

$$R(\Delta t)=\mathrm{E}\left[a\left(t+\frac{n_1\Delta t}{N}\right)a^*\left(t+\frac{n_2\Delta t}{N}\right)\right]=e^{-\mu\frac{(n_2-n_1)\Delta t}{N}}. \tag{A.9}$$

Since b_k in (A.8) are a series of independent and identically distributed random variable, so the expectation of b_k can be computed as

$$\mathrm{E}[b_{k_1}\times b_{k_2}]=\begin{cases}1, & k_1=k_2,\\ 0, & k_1\neq k_2.\end{cases} \tag{A.10}$$

According to (A.10), $R(\Delta t)$ can be computed as

$$\begin{aligned}R(\Delta t)&=\mathrm{E}\left[e^{-\mu\frac{(n_1+n_2)\Delta t}{N}}+\left(1-e^{-\mu\frac{2\Delta t}{N}}\right)\left(\sum_{k=2}^{n_1+1}e^{-\mu\frac{(n_1+1-k)\Delta t}{N}}b_k\right)\left(\sum_{k=2}^{n_1+1}e^{-\mu\frac{(n_2+1-k)\Delta t}{N}}b_k\right)\right]\\&=\mathrm{E}\left[e^{-\mu\frac{(n_1+n_2)\Delta t}{N}}+\left(1-e^{-\mu\frac{2\Delta t}{N}}\right)\left(\sum_{k=2}^{n_1+1}e^{-\mu\frac{(n_1+n_2+2-2k)\Delta t}{N}}\right)\right].\end{aligned} \tag{A.11}$$

Then, the result in (A.9) can be computed easily by using geometric sequence property and straightforward mathematics based on (A.11). □

According to Lemma A.1, the stationary assumption is used to derive the close-from temporal ACF expression. It leads to the expression of $C(t,t+\Delta t)$ can be simplified to

$$C(t,t+\Delta t)=E\left[e^{-j\frac{\omega_c}{c}\lim\limits_{N\to\infty}\left\{\frac{\Delta t}{N}\sum\limits_{n=0}^{N-1}\left[\left(e^{-\mu\frac{n\Delta t}{N}}b_1+\sqrt{1-e^{-\mu\frac{2\Delta t}{N}}}\sum\limits_{k=2}^{n+1}e^{-\mu\frac{(n+1-k)\Delta t}{N}}b_k\right)\cos\left(\omega_v\left(t+\frac{n\Delta t}{N}\right)+\phi_0\right)\right]\right\}}}\right], \tag{A.12}$$

by replacing $a\left(t+\frac{n\Delta t}{N}\right)$ in (A.7). b_1 and b_k in (A.12) are random parameters obey i.i.d. Gaussian distribution.

Then, according to characteristic function $\mathrm{E}\left[e^{jt_cX_c}\right] = e^{jt_c\mu_c - \frac{\sigma_c^2 t_c^2}{2}}$, where t_c is the argument of the characteristic function, X_c is the random variable obeys Gaussian distribution, μ_c is the mean of X_c, and σ_c^2 is the variance of X_c, the $C(\Delta t)$ in (A.12) can be computed [135]. In the case, b_k is X_c, μ_c is 0, and t_c is 1. Therefore, the temporal ACF can be simplified as

$$C(t, t+\Delta t) = e^{-0.5\sigma_{\mathrm{v}}^2 \sigma_X^2(t, t+\Delta t)}, \tag{A.13}$$

where

$$\sigma_X^2(t, t+\Delta t) = \left(\frac{\omega_{\mathrm{c}}}{c}\right)^2 (\alpha + \beta). \tag{A.14}$$

Therein, α and β are computed by

$$\alpha = \lim_{N\to\infty} \left\{ \left(\frac{\Delta t}{N}\right)^2 \left(\sum_{n=0}^{N-1} \cos\left(\omega_{\mathrm{v}} t + \omega_{\mathrm{v}} \frac{n\Delta t}{N} + \phi_0\right) e^{-\mu\Delta t} \right)^2 \right\}, \tag{A.15}$$

and

$$\beta = \lim_{N\to\infty} \left\{ \left(\frac{\Delta t}{N}\right)^2 \left(1 - e^{-\frac{2\mu\Delta t}{N}}\right) \sum_{k=2}^{N} \left(\sum_{n=k-1}^{N-1} \cos\left(\omega_{\mathrm{v}} t + \omega_{\mathrm{v}} \frac{n\Delta t}{N} + \phi_0\right) e^{-\mu \frac{(n+1-k)\Delta t}{N}} \right)^2 \right\}. \tag{A.16}$$

According to definite-integral notation in [134], (A.15) and (A.16) can be equalled to

$$\alpha = \left(\int_0^{\Delta t} \cos\left(\omega_{\mathrm{v}} x + \omega_{\mathrm{v}} t + \phi_0\right) e^{-\mu\Delta t} \mathrm{d}x \right)^2, \tag{A.17}$$

and

$$\beta = 2\mu \int_0^{\Delta t} \left(\int_{x_2}^{\Delta t} \cos\left(\omega_{\mathrm{v}} t + \omega_{\mathrm{v}} x_1 + \phi_0\right) e^{-\mu x_1 + \mu x_2} \mathrm{d}x_1 \right)^2 \mathrm{d}x_2, \tag{A.18}$$

where the variable n in (A.15) is replaced by $\mathrm{d}x$ in (A.17), and the variable k and n in (A.16) are replaced by $\mathrm{d}x_1$ and $\mathrm{d}x_2$ in (A.18), respectively.

The results of (A.17) and (A.18) are computed and substituted into (A.14), the results are described in

$$\sigma_X^2(\Delta t) = \left(\frac{\omega_c}{c}\right)^2 \left[\begin{array}{l} \frac{1}{2\left(\mu^2+{\omega_v}^2\right)\omega_v} \left[\begin{array}{l} -\omega_v \cos(2\phi) - \mu \sin(2\phi) - \omega_v \cos(2\phi + 2\omega_v \Delta t) \\ +\mu \sin(2\omega_v \Delta t + 2\phi) + 2\omega_v e^{-\mu \Delta t} \cos(\omega_v \Delta t + 2\phi) \end{array} \right] \\ +\left(\frac{1}{\mu^2+{\omega_v}^2}\right)^2 \left[\begin{array}{l} \mu \Delta t \left(\omega_v^2 + \mu^2\right) - 2\mu\omega_v \sin(\omega_v \Delta t) e^{-\mu \Delta t} - \mu^2 + {\omega_v}^2 \\ +\mu^2 \cos(\omega_v \Delta t) e^{-\mu \Delta t} - {\omega_v}^2 \cos(\omega_v \Delta t) e^{-\mu \Delta t} \end{array} \right] \end{array} \right]. \tag{A.19}$$

It can be seen that $\sigma_X^2(\Delta t)$ is a function of ϕ, μ, ω_v, ω_c, c, and Δt. $\omega_v t$ and ϕ_0 are set to ϕ in (A.19), where $\omega_v t + \phi_0 = \phi$. $2\phi + \omega_v \Delta t$ could be set to ϕ', which can simplify the computation to

$$\sigma_X^2(\Delta t) = \left(\frac{\omega_c}{c}\right)^2 \left[\begin{array}{l} \frac{1}{\left(\mu^2+{\omega_v}^2\right)\omega_v} \left(-\omega_v \cos(\omega_v \Delta t) + \mu \sin(\omega_v \Delta t) + \omega_v e^{-\mu \Delta t}\right) \cos\phi' \\ +\left(\frac{1}{\mu^2+{\omega_v}^2}\right)^2 \left[\begin{array}{l} \mu \Delta t \left(\omega_v^2 + \mu^2\right) - 2\mu\omega_v \sin(\omega_v \Delta t) e^{-\mu \Delta t} - \mu^2 + {\omega_v}^2 \\ +\mu^2 \cos(\omega_v \Delta t) e^{-\mu \Delta t} - {\omega_v}^2 \cos(\omega_v \Delta t) e^{-\mu \Delta t} \end{array} \right] \end{array} \right]. \tag{A.20}$$

Then, substituting (A.20) into (A.13), the temporal ACF closed-form can be computed by using the Bessel function [134]. Finally, the closed-form result is shown in (3.7).

Appendix B

Appendix of Chapter 4

B.1 Proof of Theorem 4.1

According to (4.3), if the transmitted symbol is s_k, the distribution of the received signal is

$$y_k \sim \mathscr{CN}\left(\sqrt{\gamma}\mathbf{h}\left(T_{\mathrm{e}}\right)C\left(T_{\mathrm{e}},t\right)s_k, \gamma\left(1-\left|C\left(T_{\mathrm{e}},t\right)\right|^2\right)\left|s_k\right|^2+1\right). \tag{B.1}$$

Hence, the real part y_k^{R} and the imaginary part y_k^{I} of y_k follow the following distributions respectively,

$$\begin{aligned} y_k^{\mathrm{R}} &\sim \mathscr{N}\left(\mathrm{Re}\left[\sqrt{\gamma}\mathbf{h}\left(T_{\mathrm{e}}\right)C\left(T_{\mathrm{e}},t\right)s_k\right], 0.5\left[\gamma\left(1-\left|C\left(T_{\mathrm{e}},t\right)\right|^2\right)\left|s_k\right|^2+1\right]\right), \\ y_k^{\mathrm{I}} &\sim \mathscr{N}\left(\mathrm{Im}\left[\sqrt{\gamma}\mathbf{h}\left(T_{\mathrm{e}}\right)C\left(T_{\mathrm{e}},t\right)s_k\right], 0.5\left[\gamma\left(1-\left|C\left(T_{\mathrm{e}},t\right)\right|^2\right)\left|s_k\right|^2+1\right]\right). \end{aligned} \tag{B.2}$$

Therefore, the joint probability density function (PDF) of y_k is given by

$$F_{y_k}\left(y\right) = F_{y_k^{\mathrm{R}}}\left(y\right)F_{y_k^{\mathrm{I}}}\left(y\right) = \frac{1}{\sigma_{\mathrm{e},k}^2\pi}e^{-\frac{\left|y-\sqrt{\gamma}\hat{\mathbf{h}}\left(T_{\mathrm{e}}\right)C\left(T_{\mathrm{e}},t\right)s_k\right|^2}{\sigma_{\mathrm{e},k}^2}}, \tag{B.3}$$

where $\sigma_{\mathrm{e},k}^2$ is shown in (4.7).

Based on the maximum likelihood theorem [136], the demodulated symbol index is given by

$$\hat{k} = \underset{k\in\{1,2,\cdots,M\}}{\arg\max} \left\{ \frac{1}{\sigma_{\mathrm{e},k}^2 \pi} e^{-\frac{\left|\mathbf{y}(t)-\sqrt{\gamma}\hat{\mathbf{h}}(T_\mathrm{e})C(T_\mathrm{e},t)s_k\right|^2}{\sigma_{\mathrm{e},k}^2}} \right\}. \tag{B.4}$$

After some mathematical manipulation of (B.4), (4.6) could be obtained.

B.2 Proof of Theorem 4.2

According to (4.8), the UUB on the ABEP of the sub-optimum detector is given by

$$\mathrm{ABEP} \leq \sum_{m=1}^{Nt} \sum_{\hat{m}=1}^{Nt} \frac{\mathscr{N}_{(m\to\hat{m})} \mathrm{P}_{(m\to\hat{m})}}{M \log_2(M)}. \tag{B.5}$$

According to [137, 138], the PEP is defined by

$$\begin{aligned} \mathrm{P}_{(m\to\hat{m})} &\triangleq \mathrm{P}\left(\|\mathbf{y}(t) - \sqrt{\gamma}\mathbf{h}(T_\mathrm{e})C(T_\mathrm{e},t)s_m\|^2 > \|\mathbf{y}(t) - \sqrt{\gamma}\mathbf{h}(T_\mathrm{e})C(T_\mathrm{e},t)s_{\hat{m}}\|^2 \right) \\ &= Q\left(\sqrt{\frac{\left\|\sqrt{\gamma}\mathbf{h}(T_\mathrm{e})C(T_\mathrm{e},t)\right\|^2 |s_m - s_{\hat{m}}|^2}{2\gamma\left(1-C(T_\mathrm{e},t)^2\right)|s_m|^2 + 1}} \right), \end{aligned} \tag{B.6}$$

where $Q(x) = \frac{1}{\pi}\int_0^{\frac{\pi}{2}} e^{\left(-\frac{x^2}{2\sin^2\theta}\right)} \mathrm{d}\theta$.

B.3 The Table of $\mathbf{h}(T_e)$ Value in the Monte Carlo Simulations

Table B.1 $\mathbf{h}(T_e)$ Value in the Monte Carlo Simulations

	Case 1	Case 2
h_1	1.5511+ 0.1561i	0.9578+2.0563i
h_2	-0.4685 + 0.3031i	-0.7581+0.5835i
h_3	0.8435 - 0.3901i	0.6795+0.9751i
h_4	1.2329 + 0.4709i	0.0877-0.7482i
h_5	-0.4971 - 1.1352i	1.0159-0.3314i
h_6	0.1728 + 0.2262i	-1.3866-0.1927i
h_7	0.1781 - 0.4837i	-0.1398+0.7767i
h_8	-0.5205 + 0.6567i	-0.8541-0.1965i

References

[1] J. Lyu and R. Zhang, "Network-connected UAV: 3-D system modeling and coverage performance analysis," *IEEE Internet Things J.*, vol. 6, no. 4, pp. 7048–7060, Aug. 2019.

[2] B. Wang, Y. Sun, N. Zhao *et al.*, "Learn to coloring: Fast response to perturbation in UAV-assisted disaster relief networks," *IEEE Trans. Veh. Technol.*, vol. 69, no. 3, pp. 3505–3509, Mar. 2020.

[3] T. Hou, Y. Liu, Z. Song *et al.*, "UAV-to-everything (U2X) networks relying on NOMA: A stochastic geometry model," *IEEE Trans. Veh. Technol.*, vol. 69, no. 7, pp. 7558–7568, Jul. 2020.

[4] J. G. Andrews, S. Buzzi, W. Choi *et al.*, "What will 5G be?" *IEEE J. Sel. Areas Commun.*, vol. 32, no. 6, pp. 1065–1082, Jun. 2014.

[5] W. Zhang, W. Zhang, and J. Wu, "UAV beam alignment for highly mobile millimeter wave communications," *IEEE Trans. Veh. Technol.*, vol. 69, no. 8, pp. 8577–8585, Aug. 2020.

[6] T. Rappaport, S. Sun, R. Mayzus *et al.*, "Millimeter wave mobile communications for 5G cellular: It will work!" *IEEE Access*, vol. 1, pp. 335–349, 2013.

[7] Z. Ma, B. Ai, R. He *et al.*, "A wideband non-stationary air-to-air channel model for UAV communications," *IEEE Trans. Veh. Technol.*, vol. 69, no. 2, pp. 1214–1226, Feb. 2020.

[8] F. Boccardi, R. W. Heath, A. Lozano *et al.*, "Five disruptive technology directions for 5G," *IEEE Commun. Mag.*, vol. 52, no. 2, pp. 74–80, Feb. 2014.

[9] FAA. FAA Aerospace Forecast Fiscal Years 2020-2040. Accessed: Mar. 19, 2021. [Online]. Available: https://www.faa.gov/data_research/aviation/aerospace_forecasts/media/FY2020-40_FAA_Aerospace_Forecast.pdf

[10] A. Aragon-Zavala, J. Cuevas-Ruíz, and J. Delgado-Penín, *High-Altitude Platforms for Wireless Communications*. Chichester: John Wiley, 2008.

[11] A. Al-Hourani, S. Kandeepan, and S. Lardner, "Optimal LAP altitude for maximum coverage," *IEEE Wireless Commu. Lett.*, vol. 3, no. 6, pp. 569–572, Dec. 2014.

[12] Y. Zeng, R. Zhang, and T. J. Lim, "Wireless communications with unmanned aerial vehicles: Opportunities and challenges," *IEEE Commun. Mag.*, vol. 54, no. 5, pp. 36–42, May 2016.

[13] H. C. Nguyen, R. Amorim, J. Wigard *et al.*, "How to ensure reliable connectivity for aerial vehicles over cellular networks," *IEEE Access*, vol. 6, pp. 12 304–12 317, 2018.

[14] Y. Zeng, J. Lyu, and R. Zhang, "Cellular-connected UAV: Potential, challenges, and promising technologies," *IEEE Wireless Commun.*, vol. 26, no. 1, pp. 120–127, Feb. 2019.

[15] 3GPP, " Study on enhanced LTE support for aerial vehicles ," 3rd Generation Partnership Project (3GPP), TR 36.777 V15.0.0, Dec. 2017. [Online]. Available: https://www.3gpp.org/uas-uav

[16] Y. Zeng, Q. Wu, and R. Zhang, "Accessing from the sky: A tutorial on UAV communications for 5G and beyond," *Proc. IEEE*, vol. 107, no. 12, pp. 2327–2375, Dec. 2019.

[17] A. A. Khuwaja, Y. Chen, N. Zhao *et al.*, "A survey of channel modeling for UAV communications," *IEEE Commun. Surv. Tut.*, vol. 20, no. 4, pp. 2804–2821, Fourthquarter 2018.

[18] Q. Zhang, H. Sun, Z. Feng *et al.*, "Data-aided Doppler frequency shift estimation and compensation for UAVs," *IEEE Internet Things J.*, vol. 7, no. 1, pp. 400–415, Jan. 2020.

[19] L. Chen, Y. Yang, X. Chen *et al.*, "Energy-efficient link adaptation on Rayleigh fading channel for OSTBC MIMO system with imperfect CSIT," *IEEE Trans. Veh. Technol.*, vol. 62, no. 4, pp. 1577–1585, May 2013.

[20] Z. Hasan, H. Boostanimehr, and V. K. Bhargava, "Green cellular networks: A survey, some research issues and challenges," *IEEE Commun. Surv. Tut.*, vol. 13, no. 4, pp. 524–540, Fourthquarter 2011.

[21] M. Banagar, H. S. Dhillon, and A. F. Molisch, "Impact of UAV wobbling on the air-to-ground wireless channel," *IEEE Trans. Veh. Technol.*, vol. 69, no. 11, pp. 14 025–14 030, Nov. 2020.

[22] W. Khawaja, I. Guvenc, D. W. Matolak *et al.*, "A survey of air-to-ground propagation channel modeling for unmanned aerial vehicles," *IEEE Commun. Surv. Tut.*, vol. 21, no. 3, pp. 2361–2391, Thirdquarter 2019.

[23] Y. Zeng, J. Xu, and R. Zhang, "Energy minimization for wireless communication with rotary-wing UAV," *IEEE Trans. Wireless Commun.*, vol. 18, no. 4, pp. 2329–2345, Apr. 2019.

[24] J. Chakareski, S. Naqvi, N. Mastronarde *et al.*, "An energy efficient framework for UAV-Assisted millimeter wave 5G heterogeneous cellular networks," *IEEE Trans. Green Commun. Netw.*, vol. 3, no. 1, pp. 37–44, Mar. 2019.

[25] Z. Xiao, P. Xia, and X. Xia, "Enabling UAV cellular with millimeter-wave communication: Potentials and approaches," *IEEE Commun. Mag.*, vol. 54, no. 5, pp. 66–73, May 2016.

[26] C. Zhang, W. Zhang, W. Wang *et al.*, "Research challenges and opportunities of UAV millimeter-wave communications," *IEEE Wireless Commun.*, vol. 26, no. 1, pp. 58–62, Feb. 2019.

[27] Z. Pi and F. Khan, "An introduction to millimeter-wave mobile broadband systems," *IEEE Commun. Mag.*, vol. 49, no. 6, pp. 101–107, Jun. 2011.

[28] S. Rangan, T. S. Rappaport, and E. Erkip, "Millimeter-wave cellular wireless networks: Potentials and challenges," *Proc. IEEE*, vol. 102, no. 3, pp. 366–385, Mar. 2014.

[29] T. S. Rappaport, J. N. Murdock, and F. Gutierrez, "State of the art in 60-GHz integrated circuits and systems for wireless communications," *Proc. IEEE*, vol. 99, no. 8, pp. 1390–1436, Aug. 2011.

[30] T. S. Rappaport, R. W.Heath, R. C. Daniels *et al.*, *Millimeter Wave Wireless Communications*. Upper Saddle River, N.J.: Prentice Hall PTR, 2015.

[31] A. Goldsmith, *Wireless Communications*. Cambridge: Cambridge University Press, 2005.

[32] T. S. Rappaport, E. Ben-Dor, J. N. Murdock *et al.*, "38 GHz and 60 GHz angle-dependent propagation for cellular peer-to-peer wireless communications," in *Proc. IEEE ICC*, Ottawa, ON, Canada, 2012, pp. 4568–4573.

[33] T. S. Rappaport, "Wireless communications: Principles and practice," 2002.

[34] M. Shafi, J. Zhang, H. Tataria *et al.*, "Microwave vs. millimeter-wave propagation channels: Key differences and impact on 5G cellular systems," *IEEE Commun. Mag.*, vol. 56, no. 12, pp. 14–20, Dec. 2018.

[35] C. Wang, J. Bian, J. Sun *et al.*, "A survey of 5G channel measurements and models," *IEEE Commun. Surv. Tut.*, vol. 20, no. 4, pp. 3142–3168, Fourthquarter 2018.

[36] T. K. Sarkar, Z. Ji, K. Kim *et al.*, "A survey of various propagation models for mobile communication," *IEEE Antennas Propag. Mag.*, vol. 45, no. 3, pp. 51–82, Jun. 2003.

[37] C. Yang, B. Wu, and C.Ko, "A ray-tracing method for modeling indoor wave propagation and penetration," *IEEE Trans. Antennas Propag.*, vol. 46, no. 6, pp. 907–919, Jun. 1998.

[38] K. A. Remley, H. R. Anderson, and A. Weisshar, "Improving the accuracy of ray-tracing techniques for indoor propagation modeling," *IEEE Trans. Veh. Technol.*, vol. 49, no. 6, pp. 2350–2358, Nov. 2000.

[39] S. Grubisic, W. P. Carpes, J. P. A. Bastos *et al.*, "Association of a PSO optimizer with a quasi-3D ray-tracing propagation model for mono and multi-criterion antenna positioning in indoor environments," *IEEE Trans. Magn.*, vol. 49, no. 5, pp. 1645–1648, May 2013.

[40] S. Y. Seidel and T. S. Rappaport, "Site-specific propagation prediction for wireless in-building personal communication system design," *IEEE Trans. Veh. Technol.*, vol. 43, no. 4, pp. 879–891, Nov. 1994.

[41] D. M. Rose, S. Rey, and T. Kurner, "Differential 3D ray-launching using arbitrary polygonal shapes in time-variant indoor scenarios," in *Proc. GSMM*, Espoo, Finland, 2016, pp. 1–4.

[42] W. Ying, S. Safavi-Naeini, and S. Chaudhuri, "A hybrid technique based on combining ray tracing and FDTD methods for site-specific modeling of indoor radio wave propagation," *IEEE Trans. Antennas Propag.*, vol. 48, no. 5, pp. 743–754, May 2000.

[43] X. Zhang and C. Sarris, "A high-accuracy ADI scheme for the vector parabolic equation applied to the modeling of wave propagation in tunnels," *IEEE Antennas Wirel. Propag. Lett.*, vol. 13, pp. 650–653, Apr. 2014.

[44] S. Yang, J. Zhang, and J. Zhang, "Impact of foliage on urban mmWave wireless propagation channel: A ray-tracing based analysis," in *Proc. ISAP*, Xi'an, China, 2019, pp. 1–3.

[45] Y. Yuan, C. Wang, X. Cheng *et al.*, "Novel 3D geometry-based stochastic models for non-isotropic MIMO vehicle-to-vehicle channels," *IEEE Trans. Wireless Commun.*, vol. 13, no. 1, pp. 298–309, Jan. 2014.

[46] P. Almers, E. Bonek, A. Burr *et al.*, "Survey of channel and radio propagation models for wireless MIMO systems," *J Wireless Com Network*, vol. 1, pp. 1–19, Feb. 2007.

[47] K. J. Q. Zhu, Y. Wang *et al.*, "3D non-stationary geometry-based multi-input multi-output channel model for UAV-ground communication systems," *IET Microw. Antennas Propag.*, vol. 13, no. 8, pp. 1104–1112, Jun. 2019.

[48] A. Abdi and M. Kaveh, "A space-time correlation model for multielement antenna systems in mobile fading channels," *IEEE J. Sel. Areas Commun.*, vol. 20, no. 3, pp. 550–560, Apr. 2002.

[49] X. Yin and X.Cheng, *Geometry-based Stochastic Channel Modeling*. Chichester: John Wiley, 2016, ch. 4, pp. 77–105.

[50] H. Chang, J. Bian, C. Wang *et al.*, "A 3D non-stationary wideband GBSM for low-altitude UAV-to-ground V2V MIMO channels," *IEEE Access*, vol. 7, pp. 70 719–70 732, 2019.

[51] J. Karedal, F. Tufvesson, N. Czink *et al.*, "A geometry-based stochastic MIMO model for vehicle-to-vehicle communications," *IEEE Trans. Wireless Commun.*, vol. 8, no. 7, pp. 3646–3657, Jul. 2009.

[52] J. Chen, B. Daneshrad, and W. Zhu, "MIMO performance evaluation for airborne wireless communication systems," in *Proc. IEEE Military Communications Conference*, Baltimore, MD, USA, 2011, pp. 1827–1832.

[53] X. Ye, X. Cai, and X. Yin, "Air-to-ground big-data-assisted channel modeling based on passive sounding in LTE networks," in *Proc. IEEE GLOBECOM Workshops*, Singapore, 2017, pp. 1–6.

[54] R. M. Gutierrez, H. Yu, Y. Rong *et al.*, "Time and frequency dispersion characteristics of the UAS wireless channel in residential and mountainous desert terrains," in *Proc. 14th IEEE CCNC*, Las Vegas, NV, USA, 2017, pp. 516–521.

[55] D. Hague, H. T. Kung, and B. Suter, "Field experimentation of cots-based uav networking," in *Proc. IEEE Military Communications Conference*, Washington, DC, USA, 2006, pp. 1–7.

[56] R. Amorim, H. Nguyen, P. Mogensen *et al.*, "Radio channel modeling for UAV communication over cellular networks," *IEEE Wireless Commu. Lett.*, vol. 6, no. 4, pp. 514–517, Aug. 2017.

[57] A. Al-Hourani and K. Gomez, "Modeling cellular-to-UAV path-loss for suburban environments," *IEEE Wireless Commu. Lett.*, vol. 7, no. 1, pp. 82–85, Feb. 2018.

[58] T. J. Willink, C. C. Squires, G. W. K. Colman *et al.*, "Measurement and characterization of low-altitude air-to-ground MIMO channels," *IEEE Trans. Veh. Technol.*, vol. 65, no. 4, pp. 2637–2648, Apr. 2016.

[59] M. Taniguchi, E. Sasaki, M. Ueba *et al.*, "Radio environment measurement over the urban area for UAV communications," in *Proc. ISAP*, Osaka, Japan, 2021, pp. 69–70.

[60] C. Calvo-Ramírez, Z. Cui, C. Briso *et al.*, "UAV air-ground channel ray tracing simulation validation," in *Proc. IEEE/CIC ICCC Workshops*, Beijing, China, 2018, pp. 122–125.

[61] E. Greenberg and P. Levy, "Channel characteristics of UAV to ground links over multipath urban environments," in *Proc. IEEE COMCAS*, Tel-Aviv, Israel, 2017, pp. 1–4.

[62] Z. Cui, K. Guan, D. He *et al.*, "Propagation modeling for UAV air-to-ground channel over the simple mountain terrain," in *Proc. IEEE ICC Workshops*, Shanghai, China, 2019, pp. 1–6.

[63] M. J. Arpaio, E. M. Vitucci, and M. Barbiroli, "Ray-launching narrowband analysis of uav-to-ground propagation in urban environment," in *Proc. ISAP*, Xi'an, China, 2019, pp. 1–3.

[64] H. Hou and L. Wang, "Analysis on time-variant air-to-ground radio communication channel for rotary-wing UAVs," in *Proc. IEEE 89th VTC-Spring*, Kuala Lumpur, Malaysia, 2019, pp. 1–6.

[65] X. Cheng and Y. Li, "3D geometry-based stochastic model for UAV-MIMO wideband non-stationary channels," *IEEE Internet Things J.*, vol. 6, no. 2, pp. 1654–1662, Apr. 2019.

[66] H. Jiang, Z. Zhang, L. Wu *et al.*, "Three-dimensional geometry-based UAV-MIMO channel modeling for A2G communication environments," *IEEE Commun. Lett.*, vol. 22, no. 7, pp. 1438–1441, Jul. 2018.

[67] H. Jia, H. Chen, S. Wang *et al.*, "3D non-stationary unmanned aerial vehicles' MIMO channel model," *IET Commun.*, vol. 13, no. 18, pp. 2941–2945, Nov. 2019.

[68] H. Jiang, Z. Zhang, and G. Gui, "Three-dimensional non-stationary wideband geometry-based UAV channel model for A2G communication environments," *IEEE Access*, vol. 7, pp. 26 116–26 122, 2019.

[69] X. Zhang and X. Cheng, "Three-dimensional non-stationary geometry-based stochastic model for UAV-MIMO Ricean fading channels," *IET Commun.*, vol. 13, no. 16, pp. 2617–2627, Oct. 2019.

[70] M. T. Dabiri, H. Safi, S. Parsaeefard *et al.*, "Analytical channel models for millimeter wave UAV networks under hovering fluctuations," *IEEE Trans. Wireless Commun.*, vol. 19, no. 4, pp. 2868–2883, Apr. 2020.

[71] E. T. Michailidis, N. Nomikos, P. Trakadas *et al.*, "Three-dimensional modeling of mmWave doubly massive MIMO aerial fading channels," *IEEE Trans. Veh. Technol.*, vol. 69, no. 2, pp. 1190–1202, Feb. 2020.

[72] W. Khawaja, O. Ozdemir, and I. Guvenc, "UAV air-to-ground channel characterization for mmWave systems," in *Proc. IEEE 86th VTC-Fall*, Toronto, Canada, 2017, pp. 1–5.

[73] ——, "Temporal and spatial characteristics of mmWave propagation channels for UAVs," in *Proc. 11th GSMM*, Boulder, USA, 2018, pp. 1–6.

[74] Y. Li, N. Li, and C. Han, "Ray-tracing simulation and hybrid channel modeling for low-Terahertz UAV communications," in *Proc. IEEE ICC*, Montreal, QC, Canada, 2021, pp. 1–6.

[75] L. Cheng, Q. Zhu, C. Wang *et al.*, "Modeling and simulation for UAV air-to-ground mmwave channels," in *Proc.14th EuCAP*, Copenhagen, Denmark, 2020, pp. 1–5.

[76] Z. Ma, B. Ai, R. He *et al.*, "A non-stationary geometry-based MIMO channel model for millimeter-wave UAV networks," *IEEE J. Sel. Areas Commun.*, vol. 39, no. 10, pp. 2960–2974, Oct. 2021.

[77] ITU, " Propagation data and prediction methods required for the design of terrestrial broadband millimetric radio access systems operating in a frequency range of about 20-50 GHz ," International telecommunication union (ITU), P 1410-2, Apr. 2003.

[78] A. Al-Hourani, S. Kandeepan, and A. Jamalipour, "Modeling air-to-ground path loss for low altitude platforms in urban environments," in *Proc. IEEE GLOBECOM*, Austin, TX, USA, 2014, pp. 2898–2904.

[79] P. K. Sharma and D. I. Kim, "Random 3D mobile UAV networks: Mobility modeling and coverage probability," *IEEE Trans. Wireless Commun.*, vol. 18, no. 5, pp. 2527–2538, May 2019.

[80] S. Khan, U. Naseem, A. Sattar *et al.*, "UAV-aided 5G network in suburban, urban, dense urban, and high-rise urban environments," in *Proc. IEEE 19th International Symposium on Network Computing and Applications*, Cambridge, MA, USA, 2020, pp. 1–4.

[81] Z. Guo, Z. Wei, Z. Feng *et al.*, "Coverage probability of multiple UAVs supported ground network," *Electron. Lett.*, vol. 53, no. 13, pp. 885–887, Jun. 2017.

[82] M. M. Azaria, F. Rosas, K. Chen *et al.*, "Ultra reliable UAV communication using altitude and cooperation diversity," *IEEE Trans. Commun.*, vol. 66, no. 1, pp. 330–344, Jan. 2018.

[83] A. Al-Hourani, "On the probability of line-of-sight in urban environments," *IEEE Wireless Commu. Lett.*, vol. 9, no. 8, pp. 1178–1181, Aug. 2020.

[84] B. Wang, J. Ouyang, W. Zhu *et al.*, "Optimal altitude of UAV-BS for minimum boundary outage probability with imperfect channel state information," in *Proc. IEEE/CIC ICCC*, Changchun, China, 2019, pp. 607–611.

[85] A. AL-Hourani, S. Chandrasekharan, G. Kaandorp *et al.*, "Coverage and rate analysis of aerial base stations [letter]," *IEEE Trans. Aerosp. Electron. Syst.*, vol. 52, no. 6, pp. 3077–3081, Dec. 2016.

[86] Z. Meng, Y. Chen, M. Ding *et al.*, "A new look at UAV channel modeling: A long tail of LoS probability," in *Proc. IEEE 30th PIMRC*, Istanbul, Turkey, 2019, pp. 1–6.

[87] X. Yuan, Z. Feng, W. Xu *et al.*, "Capacity analysis of UAV communications: Cases of random trajectories," *IEEE Trans. Veh. Technol.*, vol. 67, no. 8, pp. 7564–7576, Aug. 2018.

[88] M. Shabanighazikelayeh and E. Koyuncu, "Optimal UAV deployment for rate maximization in IoT networks," in *Proc. IEEE 31st PIMRC*, London, UK, 2020, pp. 1–6.

[89] S. Zhang, H. Zhang, B. Di *et al.*, "Cellular UAV-to-X communications: Design and optimization for multi-UAV networks," *IEEE Trans. Wireless Commun.*, vol. 18, no. 2, pp. 1346–1359, Feb. 2019.

[90] L. Xie, J. Xu, and R. Zhang, "Throughput maximization for UAV-enabled wireless powered communication networks," *IEEE Internet Things J.*, vol. 6, no. 2, pp. 1690–1703, Apr. 2019.

[91] Y. Zeng and R. Zhang, "Energy-efficient UAV communication with trajectory optimization," *IEEE Trans. Wireless Commun.*, vol. 16, no. 6, pp. 3747–3760, Oct. 2017.

[92] C. Zhan and H. Lai, "Energy minimization in internet-of-things system based on rotary-wing UAV," *IEEE Wireless Commu. Lett.*, vol. 8, no. 5, pp. 1341–1344, Oct. 2019.

[93] S. T. Muntaha, S. A. Hassan, and H. Jung, "Energy efficiency and hover time optimization in UAV-based hetnets," *IEEE Trans. Intell. Transp. Syst.*, vol. 22, no. 8, pp. 5103–5111, Aug. 2021.

[94] Y. Huang, W. Mei, J. Xu *et al.*, "Cognitive UAV communication via joint maneuver and power control," *IEEE Trans. Commun.*, vol. 67, no. 11, pp. 7872–7888, Nov. 2019.

[95] G. Plasencia, M. Rodríguez, S. Rivera *et al.*, "Modeling and analysis of vibrations in a UAV helicopter with a vision system," *IJARS*, vol. 9, no. 5, pp. 220–228, Aug. 2012.

[96] D. Li, S. Feng, and W. Ye, "Pilot-assisted channel estimation method for OFDMA systems over time-varying channels," *IEEE Commun. Lett.*, vol. 13, no. 11, pp. 826–828, Nov. 2009.

[97] R. He, C. Schneider, B. Ai *et al.*, "Propagation channels of 5G millimeter-wave vehicle-to-vehicle communications: Recent advances and future challenges," *IEEE Veh. Technol. Mag.*, vol. 15, no. 1, pp. 16–26, Mar. 2020.

[98] L. Zhang, H. Zhao, S. Hou *et al.*, "A survey on 5G millimeter wave communications for UAV-assisted wireless networks," *IEEE Access*, vol. 7, pp. 117 460–117 504, 2019.

[99] L. Zhu, J. Zhang, Z. Xiao *et al.*, "3-D beamforming for flexible coverage in millimeter-wave UAV communications," *IEEE Commun. Lett.*, vol. 8, no. 3, pp. 837–840, Jun. 2019.

[100] J. Xu, Z. Huang, Z. Wang *et al.*, "Radial velocity retrieval for multichannel SAR moving targets with time–space Doppler ambiguity," *IEEE Trans. Geosci. Remote Sens.*, vol. 56, no. 1, pp. 35–48, Jan. 2018.

[101] G. D. Durgin, *Space-time wireless channels*. Upper Saddle River, N.J.: Prentice Hall PTR, 2003.

[102] J. Zhang, "Spatial correlation coefficient estimator for frequency selective MIMO channels," *Electron. Lett.*, vol. 55, no. 5, pp. 2290–292, Mar. 2019.

[103] J. Ponce, T. Choi, N. Abbasi *et al.*, "Air-to-ground directional channel sounder with 64-antenna dual-polarized cylindrical array," in *Proc. IEEE ICC Workshops*, Montreal, Canada, 2021, pp. 1–6.

[104] Z. Ma, B. Ai, R. He *et al.*, "Impact of UAV rotation on MIMO channel characterization for air-to-ground communication systems," *IEEE Trans. Veh. Technol.*, vol. 69, no. 11, pp. 12 418–12 431, Oct. 2020.

[105] Phantom 4 Pro V2.0 - Specifications - DJI. DJI Official. 2022. [Online]. Available: https://www.dji.com/uk/phantom-4-pro-v2/specs

[106] H. A. Cirpan and M. K. Tsatsanis, "Maximum likelihood blind channel estimation in the presence of Doppler shifts," *IEEE Trans. Signal Process.*, vol. 47, no. 6, pp. 1559–1569, Jun. 1999.

[107] L. Yang, G. Ren, and Z. Qiu, "A novel Doppler frequency offset estimation method for DVB-T system in HST environment," *IEEE Trans. Broadcast.*, vol. 58, no. 1, pp. 139–143, Mar. 2012.

[108] A. Svensson, "An introduction to adaptive QAM modulation schemes for known and predicted channels," *Proc. IEEE*, vol. 95, no. 12, pp. 2322–2336, Dec. 2007.

[109] X. Yu, S. Leung, W. H. Mow *et al.*, "Performance of variable-power adaptive modulation with space–time coding and imperfect CSI in MIMO systems," *IEEE Trans. Veh. Technol.*, vol. 58, no. 4, pp. 2115–2120, May 2009.

[110] X. Liu, Y. Liu, and F. Liu, "Adaptive threshold estimation for variable rate MQAM in full-duplex systems with imperfect CSI," *IEEE Commun. Lett.*, vol. 20, no. 3, pp. 506–509, Mar. 2016.

[111] S. Akin and M. C. Gursoy, "Performance analysis of cognitive radio systems with imperfect channel sensing and estimation," *IEEE Trans. Commun.*, vol. 63, no. 5, pp. 1554–1566, Mar. 2015.

[112] S. Yang, Z. Zhang, J. Zhang *et al.*, "Impact of rotary-wing UAV wobbling on millimeter-wave air-to-ground wireless channeld," *IEEE Trans. Veh. Technol.*

[113] Y. Fu, C. Wang, Y. Yuan *et al.*, "BER performance of spatial modulation systems under 3-D V2V MIMO channel models," *IEEE Trans. Veh. Technol.*, vol. 65, no. 7, pp. 5725–5730, Jul. 2016.

[114] W. L. Huang and K. B. Letaief, "Cross-layer scheduling and power control combined with adaptive modulation for wireless ad hoc networks," *IEEE Trans. Commun.*, vol. 55, no. 4, pp. 728–739, Apr. 2007.

[115] M. Agiwal, A. Roy, and N. Saxena, "Next generation 5G wireless networks: A comprehensive survey," *IEEE Commun. Surv. Tut.*, vol. 18, no. 3, pp. 1617–1655, Thirdquarter 2016.

[116] J. Zhang, K. J. Kim, A. A. Glazunov *et al.*, "Generalized polarization-space modulation," *IEEE Trans. Commun.*, vol. 68, no. 1, pp. 258–273, Jan. 2020.

[117] J. Zhang, Y. Wang, J. Zhang *et al.*, "Polarization shift keying (PolarSK): System scheme and performance analysis," *IEEE Trans. Veh. Technol.*, vol. 66, no. 11, pp. 10 139–10 155, Nov. 2017.

[118] Z. Xiao, L. Zhu, and X. Xia, "UAV communications with millimeter-wave beamforming: Potentials, scenarios, and challenges," *China Commun.*, vol. 17, no. 9, pp. 147–166, Sept. 2020.

[119] J. S. Blogh and L. Hanzo, *Third-Generation systems and intelligent wireless networking: Smart antennas and adaptive modulation*. Chichester: John Wiley, 2002.

[120] C. C. Zarakovitis, Q. Ni, and J. Spiliotis, "Energy-efficient green wireless communication systems with imperfect CSI and data outage," *IEEE J. Sel. Areas Commun.*, vol. 34, no. 12, pp. 3108–3126, Dec. 2016.

[121] X. Xiao, X. Tao, and J. Lu, "QoS-aware energy-efficient radio resource scheduling in multi-user OFDMA systems," *IEEE Commun. Lett.*, vol. 17, no. 1, pp. 75–78, Nov. 2013.

[122] H. Yang, Y. Ye, X. Chu *et al.*, "Energy efficiency maximization for UAV-enabled hybrid backscatter-harvest-then-transmit communications," *IEEE Trans. Wireless Commun.*, vol. 21, no. 5, pp. 2876–2891, May 2022.

[123] J. Lu, K. Letaief, J. Chuang *et al.*, "M-PSK and M-QAM BER computation using signal-space concepts," *IEEE Trans. Commun.*, vol. 47, no. 2, pp. 181–184, Feb. 1999.

[124] F. B. Hildebrand, *Introduction to numerical analysis*, 2nd ed. New York ; London: McGraw-Hill, 1973.

[125] C. Wang, J. J. Huang, H. Wang *et al.*, "6G wireless channel measurements and models: Trends and challenges," *IEEE Veh. Technol. Mag.*, vol. 15, no. 4, pp. 22–32, Dec. 2020.

[126] C. Yan, L. Fu, J. Zhang *et al.*, "A comprehensive survey on UAV communication channel modeling," *IEEE Access*, vol. 7, pp. 107 769–107 792, 2019.

[127] X. Liu, Y. Liu, and Y. Chen, "Machine learning empowered trajectory and passive beamforming design in UAV-RIS wireless networks," *IEEE J. Sel. Areas Commun.*, vol. 39, no. 7, pp. 2042–2055, Jul. 2021.

[128] A. Ranjha and G. Kaddoum, "URLLC facilitated by mobile UAV relay and RIS: A joint design of passive beamforming, blocklength, and UAV positioning," *IEEE Internet Things J.*, vol. 8, no. 6, pp. 4618–4627, Mar. 2021.

[129] H. Mei, K. Yang, J. Shen *et al.*, "Joint trajectory-task-cache optimization with phase-shift design of RIS-assisted UAV for MEC," *IEEE Wireless Commu. Lett.*, vol. 10, no. 7, pp. 1586–1590, Jul. 2021.

[130] G. Geraci, A. Garcia-Rodriguez, M. M. Azari *et al.*, "What will the future of UAV cellular communications be? A flight from 5G to 6G," 2021. [Online]. Available: arXiv: abs/2105.04842.

[131] L. Xu, M. Chen, M. Chen *et al.*, "Joint location, bandwidth and power optimization for THz-enabled UAV communications," *IEEE Commun. Lett.*, vol. 25, no. 6, pp. 1984–1988, Jun. 2021.

[132] X. Wang, P. Wang, M. Ding *et al.*, "Performance analysis of terahertz unmanned aerial vehicular networks," *IEEE Trans. Veh. Technol.*, vol. 69, no. 12, pp. 16 330–16 335, Dec. 2020.

[133] Y. Pan, K. Wang, C. Pan *et al.*, "UAV-assisted and intelligent reflecting surfaces-supported terahertz communications," *IEEE Wireless Commu. Lett.*, vol. 10, no. 6, pp. 1256–1260, Jun. 2021.

[134] D. W. Jordan and P. Smith, *Mathematical techniques: An introduction for the engineering, physical, and mathematical sciences*. Oxford: Oxford University Press.

[135] F. Oberhettinger, *Fourier transforms of distributions and their inverses: A collection of tables*. Academic Press, 1973.

[136] S. M. Kay, *Fundamentals of statistical signal processing. Volume 1, Estimation theory*. Upper Saddle River, N.J.: Prentice-Hall PTR, 1993.

[137] Q. Li, K. J. Kim, S. Ruan *et al.*, "Polarized spatial scattering modulation," *IEEE Commun. Lett.*, vol. 23, no. 12, pp. 2252–2256, Dec. 2019.

[138] K. Cho and D. Yoon, "On the general BER expression of one- and two-dimensional amplitude modulations," *IEEE Trans. Commun.*, vol. 50, no. 7, pp. 1074–1080, Jul. 2002.